**Edgar Manuel Cardoso Rocha Alves**

Graduate in Mechanical Engineering Science

# Numerical modelling of appliances and packaging to support the approval for safe transportation

Dissertation for the obtainment of the Master's Degree in
Mechanical Engineering

| | |
|---|---|
| Supervisor: | Professor Ph.D Marta Isabel Pimenta Verdete da Silva Carvalho, Assistant Professor, Faculty of Science and Technology of NOVA University of Lisbon |
| Co-supervisors: | David João Machado Martins, Platform Manager, Electrolux<br>Trevor Specht, Team Leader Mechanical Design, Electrolux |

Committee:

| | |
|---|---|
| President: | Professor Ph.D João Mário Burguete Botelho Cardoso |
| Members: | Professor Ph.D João Filipe de Almeida Milho<br>Professor Ph.D Marta Isabel Pimenta Verdete da Silva Carvalho |

FACULDADE DE
CIÊNCIAS E TECNOLOGIA
UNIVERSIDADE NOVA DE LISBOA

**September, 2019**

**Numerical modelling of packaging and appliances to support the approval for safe transportation**

*Dedicated to my girlfriend,*

*Ana,*

*and my family pillars,*

*Luís, Júlia e Loló.*

# Acknowledgements

To start with, I want to thank my supervisor Professor Doctor Marta Carvalho and both of my co-supervisors David Martins and Trevor Specht from Electrolux for all the help provided on the development of this extensive work, for the availability to answer all my questions, and for giving me the opportunity to study and develop my Dissertation's work, being one of the most fulfilling and self-improving activity that I ever got to experience. Another big acknowledgment goes to Master Ana Patrícia Martins, who was always available to share her experience in order to help me regarding *LS-DYNA* formulations and problems, making my learning process much faster.

I want to also thank my friends, either from inside or outside the university universe, for all the help and support provided and for always being there letting me know everything would turn out fine.

Above all I would like to thank my family, and specially my parents for all the help and support given to me during all this journey. I want to thank them for teaching me and making me work as hard as I could, whenever possible. If it wasn't for them, I would not be placed where I am today.

To finish with, I want to thank my girlfriend Ana, as she is the main reason why I got to finish this journey with such good results, and for helping me, relax me, and above all support me and believe in me during the hard times. I owe all the success to her.

# Abstract

---

The following dissertation consists in the development of a finite element model using the *LS-DYNA software* with the goal of creating a methodology for the conception of numerical models for electrical appliances in order to aid the certification in terms of safe transportation, during the design phase. The necessary tests undertaken are stated on protocols created by the production companies, and try to replicate the transportation behavior to which the appliances are subjected from the moment of packing to the final delivery. In the performance of these tests, there is a great amount of time and money associated and, therefore, the application of computational methods as a support on the certification of appliances, implies a great reduction of time and costs related to the reduction of necessary experimental tests.

As the study object, an Electrolux oven model was used, and the project was divided in the construction of the numerical model and its posterior validation. The validation is based on a comparison between the accelerations of components in both situations, experimental and numerical, and knowing the numerical model presents a good kinematic correlation with the experimental drop test performed by the company, a structural stress analysis was performed. The analysis focused on the critical components and deformations experienced by the model and the structural motion response was detailed to understand the oven's oscillations at impact.

**Keywords:** Finite Element Modelling, Drop Test, Electrical Appliances, Numerical Model, *LS-DYNA*

# Resumo

---

A dissertação que se segue consiste no desenvolvimento de um modelo de elementos finitos utilizando o software LS-DYNA com o objectivo de criar uma metodologia para a concepção de modelos numéricos para aparelhos electrodomésticos, de modo a auxiliar a certificação em termos de segurança de transporte, durante a fase de projecto. Os testes requeridos para o efeito estão descritos em protocolos criados pelas empresas produtoras e tentam replicar o comportamento de transporte ao qual os aparelhos são submetidos desde o momento da embalagem até a entrega final. Na realização destes ensaios, encontra-se associada uma grande quantidade de tempo e dinheiro e, portanto, a aplicação de métodos computacionais como suporte na certificação de aparelhos, pressupõe uma grande redução de tempo e custos relacionados com a redução da quantidade de ensaios experimentais em causa.

Como objeto de estudo, foi utilizado um modelo de forno Electrolux, e o projeto foi dividido na construção do modelo numérico e sua posterior validação. A validação baseia-se numa comparação entre as acelerações dos componentes em ambas as situações, experimental e numérica. Sabendo que o modelo numérico apresenta uma boa correlação cinemática com o ensaio experimental de queda realizado pela empresa, foi realizada uma análise estrutural de tensões com enfase nos componentes e deformações críticas sofridas pelo modelo. O movimento de resposta estrutural foi detalhado para compreender as oscilações do forno aquando do impacto.

**Palavras-chave:** Modelação de Elementos Finitos, Teste de Queda, Aparelhos Electrodomésticos, Modelo numérico, *LS-DYNA*

# Table of Contents

# List of Tables

# List of Figures

# 1

# Chapter 1 - Introduction

## 1.1. Research Background

In the retail market, the security of packaged goods during transportation is critical, as its possible failure will lead to a highly costly situation. That said, it is necessary that proactive security measures are taken in terms of materials and design used in the package's configuration so that the probability of ruin is negligible.

Several packaging tests can be undertaken to assess the package and product ability to endure severe transport and shock absorbing situations. It is verified then, that the most critical examination for ascertaining the most crucial tensile field to which products are subjected is the Drop Test. Except for military standards MIL-STD-810F (Military standard, 2000) and MIL-STD-883F (Military standard, 2004), there are no free fall or impact test standards for home appliances. This might be due to the fact that the usage and the transportation of electronic devices vary in terms of the customers/end users and carriers. In such a case, manufacturers write their standards or instructions according to their experience in design, based on how these appliances are being transported to the users.

Since it is expensive to conduct experimental testing all the time, due to the amount of money spent on experimental assemblies and the necessary amount of time spent in the preparation of various examinations, it has been conducted valuable research on the creation of numerical models that could substitute real-time inspections. Therefore, it is achieved a much simpler, convenient, and faster method of analysis. If accurately modeled and validated, the computational model is able to predict the drop impact response of the product even before a physical model is fabricated and tested.

This type of numerical simulations started with the creation of methodologies envisioning the prediction of potential damage locations on cellular phones and other small devices through numerical simulations to compare them with real statistical data in the early 2000s, in studies from Lim et al. (Lim, Teo, & Shim, 2002) and from Park and Kim (Park & Kim, 2004). With these investigations, the design of product durability on impact wasn't anymore wholly relied on the designer's intuition and experience, but on validated models that could translate impact deformations and potential damage locations, with a substantial reduction of the product creation time and associated costs.

Based on researches like the ones referred above, Hwan et al. (Hwan, Lin, Lo, & Chen, 2011) also employed finite element analysis together with the Taguchi Method to study the drop/impact response of cell phones. It was aimed to improve the anti-impact performance of cell phones.

The idea to start comparing data obtained through experimental tests and numerical simulations on this type of devices came after studies from Goyal et. al (S Goyal, Upasani, & Patel, 1998) regarding experimental tests using high speed photography on two different types of cellular phones to understand impact tolerance and further improve drop performance, inducing housing modifications. The research showed that a thin-walled clamshell case construction would not have enough rigidity to withstand impact-induced loads, even though the advantages regarding size and weight were outstanding. It was also shown in the study that the until then construction method for cellular phone battery packs could lead to a fracture of the battery housing in the drop.

To add to this, Goyal et al. had a very important incidence in the revolution of the drop test, creating new methods for realistic drop-testing (Suresh Goyal & Buratynski, 2000). This was a necessary step to take since both conventional testing methods, constrained and free, suffered from significant downsides. In the first, the object was not allowed to perform its natural dynamics and move naturally during the impact situation, and in the second, the main disadvantage was that it was tough to control the object's orientation during the fall, which would make it impossible to repeat the same test and compare impact results. The researchers proposed a new configuration for testing, with the object being tested suspended on a guided drop-table, in the desired impact orientation. Nevertheless, just before the impact of the drop-table, the entity was released from its suspension so that it maintained its required orientation at first impact and was free to move unconstrained.

It was intended that the development of a reliable methodology for drop/impact simulations would provide a powerful and efficient vehicle for the improvement of the design quality and reduction of the product development cycle. Taking this into account, the correlation between impact simulations on small devices and impact simulations on household appliances was fast.

Some work in this area was achieved to study not only the mechanical structure of home appliances (Mulkoglu, Guler, & Demirbag, 2015) in order to determine critical regions in the assembly and to provide any further improvements on the new structure, but also to optimize packaging protection and to verify the performance and suitability of the packaging and its interaction with the structure, in case of damage occurring during transportation or delivery (Blanco, Ortalda, & Clementi, 2015). This last research showed through finite element analysis that the current packaging being used was not able to manage loads generated by the impact, and it was the critical component that compromised the integrity of the appliance. Studies from Neumayer et al. also considered the prestressing of a cooker and its packaging due to thermal shrinkage of the plastic foil that compacts the ensemble when it's distributed (Neumayer, Chatiri, & Höermann, 2006).

With the purpose of understanding and predicting the behavior of drop test simulations on shipped products, a vital investigation was carried out on gathering the benefits of finite element analysis and design of experiments to describe the effect of packaging material stiffness, component stiffness and its mass distribution on the time and magnitude of the stress induced in a component, internal energy absorbed by the packaging material and combined relationships between these parameters (Jain, Oswal, & Khisty, 2018). This type of studies concluded that structural characteristics after impact like localized structural damage, plastic deformation tracking or even stress distribution during impact, were obtained with outstanding results and effortlessness compared to the physical inspection performed after the experimental route.

It should be noted that in the case of drop test with associated packaging, the material of the packaging and the way its physical characteristics are simulated to satisfy the simulation requirements, is of relative importance due to the non-linearity of the materials used and design geometries. In view of this difficulty, there are works studying the influence of the sample size on the stress-strain curve of several foam materials (D. S. Cronin & Ouellet, 2016), the comparison between finite element analysis on LS-DYNA and ABAQUS with compression results and cushioning diagrams for multiple loadings to show that these packages need improvement for the case of unloading and reloading (Ozturk & Anlas, 2011). Investigations also show the overall limitations of the foam materials in LS-DYNA and their necessary calibration to reproduce the best results (Croop & Lobo, 2009), (Mills & Masso-Moreu, 2005) and (Shah & Topa, 2014).

## 1.2. Objectives

The main objective of this work is to create a finite element numerical model of an oven's drop test in order to create a methodology to be followed for future ventures regarding the construction of numerical models of electric home appliances and its packaging during the design phase. Using the LS-DYNA software, it is intended to replicate and compare the software results with the data obtained experimentally in order to ensure a fully validated computational model. With this, the structural integrity of the oven may be evaluated, and critical parts may be found.

This dissertation comes as the first stage for the creation of methodologies for the optimization of electrical appliances and associated packaging, being crucial the attempt to reduce the simulation time, and the final step to perform the structural optimization of the oven model. This permits the avoidance of unnecessary and repetitive experimental testing during the design phase, reducing the design period and associated costs.

## 1.3. Study Object and Dissertation's Structure

This dissertation has as its study object the oven model presented in Figure 1-1, designed and produced by the R&D Food Preparation Department of the Electrolux company. The security certification for this model's safe transportation is composed by a battery of tests that try to replicate every step of the transportation, from the shipment in factories until reaching retailers. As from all the examinations undertaken, the most critical test to ensure the structural integrity of the model during transportation is the drop test, a finite element numerical model will be developed to replicate the loadings suffered by the oven when subjected to this test. The starting point to this project will be a numerical model containing the constituent oven parts already meshed in *Hypermesh* and positioned, to develop then all the necessary characteristics to perform a validated and well-functioning numerical analysis for the drop test.

**Figure 1-1. Oven model being studied.**

The development of this work appears from the need to create a strategy and methodology for the structural optimization of electrical home appliances. This dissertation focuses only the development of the first part of the methodology, which means creating the procedure to the utilization of finite element computational methods on the simulation of the dynamic tests required to certify electrical appliances in terms of safe transportation. Thus, this procedure is introduced by the assembly of the numerical parts provided by the company, including an extensive process that imply the material and sectional dimensions gathering for all the existing components, and also an overall analysis of the structural contribution that these will represent for the performance of the numerical simulations. From this analysis, it is possible to comprehend which components are negligible and will not contribute for the structural integrity and performance of the oven. Particular attention must be brought to the Foil and Cushioning material modelling, as both require special definitions and recommended modelling techniques for a well-rounded simulation, avoiding early calculation termination due to the existing difficulties regarding the definition of these material models.

After this first step, it follows the connection of components in various subassemblies and the modelling of contacts between these, to ensure a viable and realistic behavior for the model, preventing undesired inter-penetrations. In this phase, it is vital to perform several vibration modes analysis as the contacts and connections are being introduced, in order to study the possibility of existing missing and incorrect definitions, presenting rigid body movement modes. On the possibility that this happens, corrections on the contacts defined are implemented by changing the parameters that characterize them, and a new analysis is achieved to assess the new modifications success. It is of great importance that this phase is developed in a expedite and meticulous manner, in order to prevent difficult alterations in a posterior phase of the development of the numerical model.

When the assembly is completed, a first numerical simulation is performed to understand the impact of the Foil component's thermal shrinking and to extract a file containing the initial stress and strain values caused by this process on the rest of the assembly. Then, boundary conditions characterizing the specific dynamic test being evaluated (drop test) are given, and general final simulation controls are implemented to run the simulation.

Finished the construction of the numerical model, several numerical simulations are performed (for model parameters identification and correction) in order to obtain stress information and comparison data to validate the model, relating it to the physical one. Knowing also which components are damaged above the yield point, materials can be corrected to contemplate plastic strains and deformations and the model will produce reliable results and will be ready for the optimization stage, that will not be the aim of this work, but will be the next and final step to obtain a methodology for the structural optimization of electrical home appliances. The entire methodology can be conveniently visualized and understood by observing the flow of procedures presented in Figure 1-2.

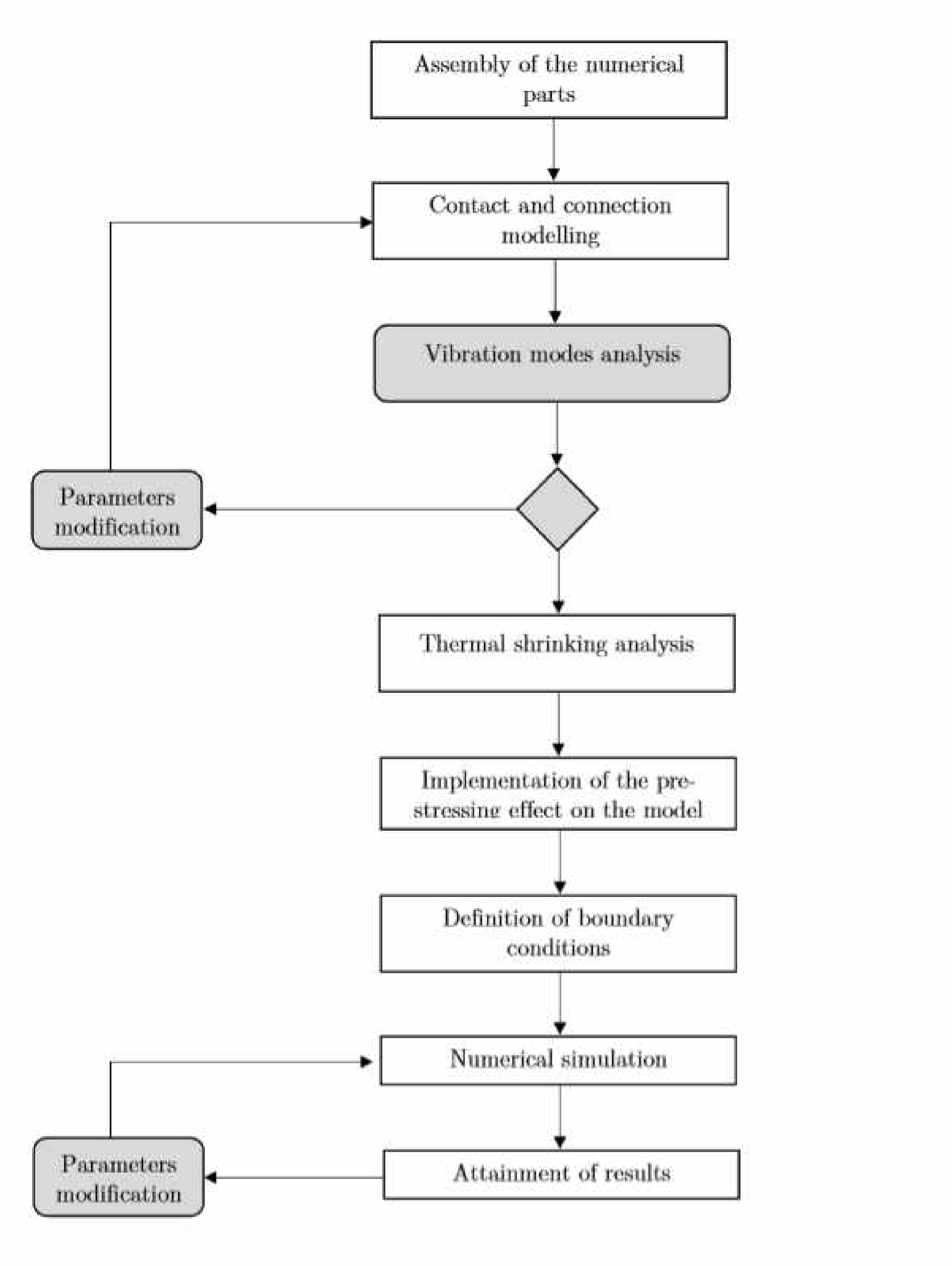

**Figure 1-2. Flow of procedures.**

# 2

# Chapter 2 - Framework

## 2.1. Evaluation Tests for Cushioning Materials

A packaging cushion is a protective system that provides an interface between a product in need of protection and a potentially damaging environment, as in distribution and transportation where high levels of shock and vibration are found. The cushioning material used will clarify the necessary design and associated performance for the protection, and relevant physical properties are usually presented by the suppliers. Although this information is typically provided, certain features must be clarified for the specific construction desired, and these can only be obtained from dynamic compression, controlled shock, and vibration type tests.

When a shock between the cushion and the drop site happens, there is a high peak short duration response that will posteriorly, directly after the impact, turn into low peak long-duration response that describes the sum of deceleration transmitted through a given thickness and drop height (Schueneman, 2017) as in the graph of Figure 2-1 a). The amount of deceleration transmitted must be below the fragility level of the product so that this one can be protected from possible damage.

In terms of vibration protection, the cushion must have the capability to be a harmonic absorber with the objective to reduce the amplitude of the product's vibration to an acceptable level. This means that the packaging will have the role to absorb the kinetic energy developed during the products excitation and work as a damper to restrain it from reaching high levels of oscillation, that is, reaching a frequency of resonance (Schueneman, 2017). It is crucial, though, that the cushion and product natural frequencies don't overlap, since this would result in the amplification of vibration of the last and would have detrimental effects on the structural composition. The transmissibility plot (which is the ratio between the response and excitation acceleration of a system) of the condition where the cushioning system provides attenuation of the product's vibration response can be seen in the graph of Figure 2-1 b), where both the cushion resonance and product response are displayed.

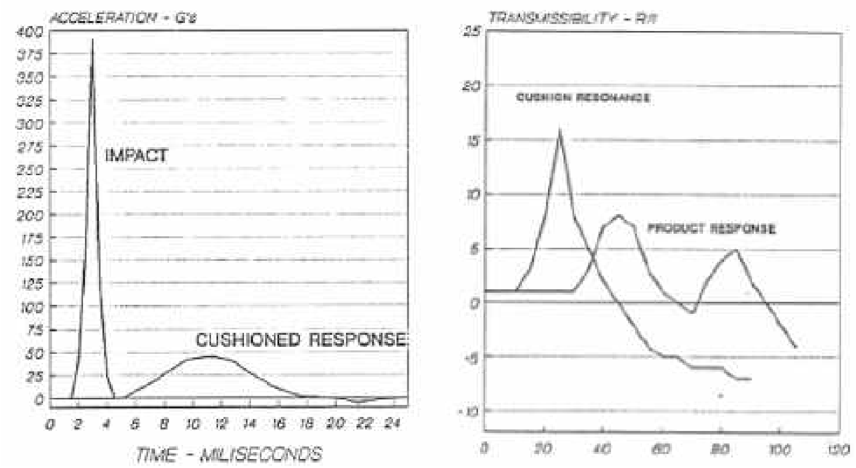

**Figure 2-1. a) Cushioned impact graph. b) Package vibration response attenuation mode graph. Source: (Schueneman, 2017).**

### 2.1.1. Basic spring dynamics

As referred before, packaging cushions can be defined as mechanical springs used to attenuate the oscillations and the amplitude of vibrations that result from collisions or impacts. This comprehends that they will turn high shock pulses into lower but longer duration ones, as it was seen before in Figure 2-1. As in a spring, the most important cushioning characteristics to be taken into account during the cushion design, are the cushion rate, the creep, and the system's natural frequency (Schueneman, 1993).

The cushion rate refers to the amount of bending in the cushion that is measured when a load is applied. There are three types of springs, all depending on what rate they are deflected, being known as linear, hardening or softening. These types of rates are described in Figure 2-2.

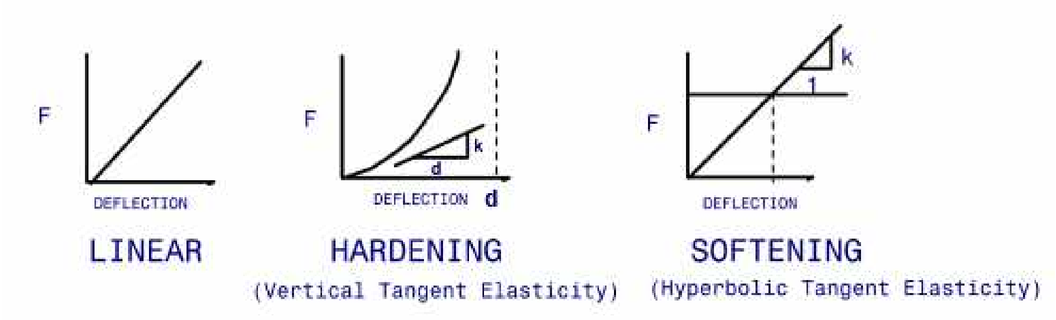

**Figure 2-2. Spring types. Source: (Schueneman, 1993)**

The compressive creep is denoted as the reduction of thickness suffered by the cushion after being statically loaded for an extended period of time. For the purpose of protecting the product, the cushion material should be designed to be near the creep limit to become as effective and efficient as possible (Schueneman, 1993).

The natural frequency present in a mass-spring system designates at what rate an object vibrates when it is not disturbed by an external body and depends on the system's mass and stiffness. There are as many natural frequencies as the degrees of freedom the system is subjected to. In Figure 2-3, it can be seen that the maximum amplitude of response is found when the input frequency on the system equals its natural frequency and the structure reaches resonance. The resonance state is undesirable, seeing that vibratory forces will amplify, and most-likely damages will occur. It is also noted that the bigger the damping coefficient, the lower the amplitude of response will convert.

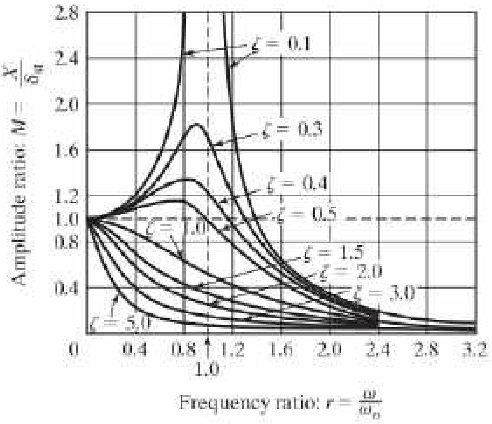

**Figure 2-3. Amplitude ratio variation with the frequency and damping ratio. Source: (Rao, 2011)**

### 2.1.2. Shock performance test

The impact resistance of a cushion material is evaluated using instrumented drops, with procedures covered by standards such as ASTM D1596-14 (ASTM International, 2014) and ASTM D4168-95 (ASTM International, 2015a). The sequence of operations stated in these standards are equivalent to a Dynamic Compression Test (Figure 2-4), which primarily concentrates in the drop of a guided platen from a pre-determined height with a pre-determined mass associated, that is intended to strike a cushion of identified thickness and area. This procedure is then executed a stated number of times, accumulating more and more weight in order to contemplate several static stress loadings. Experimental data, such as response acceleration, impact velocity, rebound velocity and strain of the test material are extracted as the platen hits the test sample (Chen, 2014) with the assistance of a velocity sensor, accelerometer and displacement sensor.

This test requires a distinct instrument called the dynamic compression tester, which is composed of a dropping platen, an impact table, the necessary sensors to find the desired characteristics of the cushion and a console to manage and analyze results.

**Figure 2-4. Dynamic compression tester. Source: Shinyei Testing Machinery CO., LTD.**

With shock performance tests such as dynamic compression tests, it is possible to identify one very important cushion characteristic, called cushion curve.

The cushion curve describes the material dynamic behavior of a cushion material with a specific thickness when exposed to diverse impact conditions, and results in a curve with peak acceleration on the vertical axis, in G, and static stress levels on the horizontal axis, in $\mathsf{g/cm^2}$ (depicted in Figure 2-5).

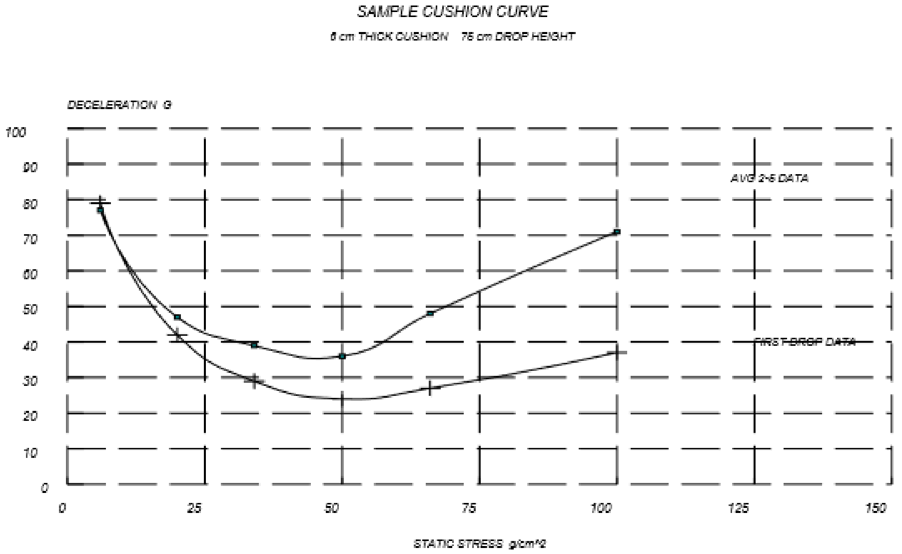

**Figure 2-5. Sample cushion curve. Source: (Schueneman, 1993)**

It is important to note that the information attained from cushion curves obtained from standards such as ASTM D1596-14 (ASTM International, 2014) are not necessarily intended to be used in a packaging design situation, but to provide comparable data between different cushion materials acquired in a controlled environment. It is also known that the variability of the cushion shape will have significant influence in the shock absorbing abilities of the material, which is not accounted in the test sample used in this standardized test (Schueneman, 2017).

Although the information from the ASTM D1596-14 standard can't give enough detail to aid packaging design, a study from Gary Burgess (Burgess, 1990) developed a method able to deduce the dynamic stress-strain curve of the cushion's material from only one cushion curve with an arbitrary drop height and cushion thickness. This method is also used to produce all other cushion curves, regardless of drop height, cushion thickness, and static loading.

There are many advantages offered by this procedure, such as the compactness of the information, the fact that the results may be used to find cushion curves for any drop heights and cushion thickness and provide information on the maximum strain occurred at the time of impact, the simplification and support of cushion design, and finally, the number of drop tests performed on a new material to evaluate its dynamic performance is drastically decreased just as the material costs associated.

Another study from Schueneman (Schueneman, 1986), also concluded that the data obtained through the ASTM D4168-95 (2015) standard presented the best results in terms of performance data when compared to the cushion curve in the final package design. The test given in this standard is called Enclosed Test Block Method and envisages the drop test of a test block surrounded by cushion material, and the entire assembly positioned in a corrugated container. Some important characteristics that make this procedure a more realistic approach are that the test block is in contact with the foam material prior to impact, like a product would be in touch with its cushion during transportation and delivery, and that the friction of the corrugated container is also taken into account (Schueneman, 1993).

### 2.1.3. Vibration response test

It is known that if frequencies from steady-state vibration inputs reach a natural frequency from the component being transported or even the product-cushioning system, resonant conditions will amplify its acceleration and displacements to damaging levels. The cumbersome regarding packaging isolation vibration problems is that the most common cushion materials used for packaging systems display non-linear load-displacement characteristics, which complicates the usage of practical analytical solving methods.

In order to determine the vibration performance of cushioning materials, a cushion sample must be subjected to a vibration input that covers the frequency range present in the distribution environment. The procedure necessary to investigate the referred properties of the material, is explained in documents such as the Military Handbook for Package Cushioning Design (Department of Defense,

1997) and discusses the monitoring of a test block which presents itself surrounded by cushion samples and placed in a corrugated container, secured to the table of the vibration test machine (see Figure 2-6). Mass is continually added to the test block, and the test is repeated to consider every static stress loading desired.

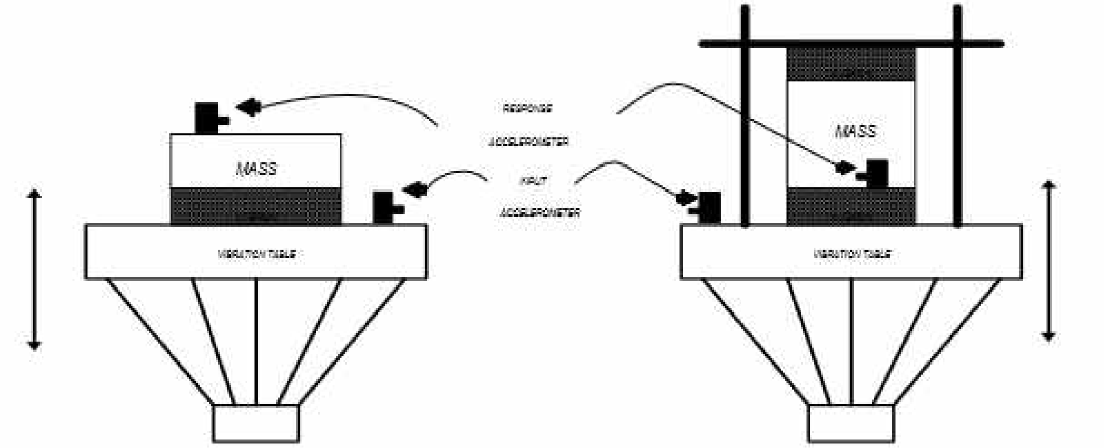

**Figure 2-6. Cushion vibration test setups. Source: (Schueneman, 1993)**

There are two possible ways to run this method of testing, as it can be seen in Figure 2-6, being the first one with a cushion sample placed below and adhered to the test block, so that the foam is able to work in both tension and compression; and the second one with a cushion sample placed above and one set below the test mass, that work only in compression due to the fixture device that only allows the whole system to move in planar section.

When the resonance search test is completed, the information obtained from the cushion and table accelerometer is used to generate the transmissibility plot of the cushion response. It is recommended that at least five vibration tests (attending five different static loading points) are implemented to find the amplification/attenuation curve (see Figure 2-7).

The amplification/attenuation curve displays the combination of frequencies and static stress loadings that amplify the vibration input. Above this zone of amplification of the response, there is a zone of attenuation where higher frequencies and loading combinations tend to attenuate the vibration input. There is, although, a zone below the amplification zone where the cushion material neither attenuates nor amplifies the vibration response. One amplification/attenuation curve is generated for each material type and material thickness combination (Department of Defense, 1997).

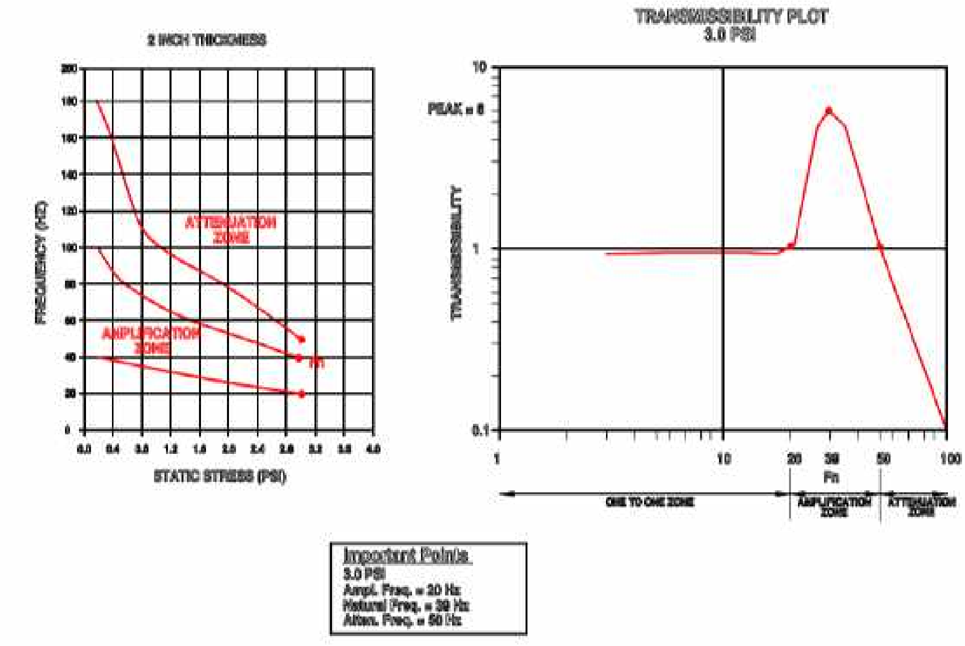

**Figure 2-7. Sample amplification/attenuation curve. Source: (Department of Defense, 1997)**

## 2.2. Packaging Design Testing

Considering all the information extracted from cushioning materials testing, a package prototype may be designed taking into consideration the optimum thickness needed for estimated drop height, rib configurations and static stress loading considering shock and vibration performance requirements.

Cushion loading is not always proven to give both shock and vibration protection so, occasionally, negotiations are necessary between the performance attributes for shock and vibration of a cushioning system. Typically, if this situation arises, it is best to ensure vibration protection rather than shock protection since a shipped product will always encounter vibration frequencies in transportation vehicles and a drop event isn't still guaranteed.

The use of ribs, which are basically created through places in the cushion where material is removed with such depth and geometry so that the vibration requirements become satisfied without significantly change the cushion shock response, usually solve problems of this kind (Schueneman, 2017).

When the rib configuration is appropriately designed, it has the ability to successfully decrease higher frequency vibrations since the reduction in material usage will be quantified in a more top loading on the material remaining, which will result in a lower natural frequency for the whole packaging system. This is somehow of great importance because the vibration response of the system can be easily altered and totally determined by the rib's geometric characteristics (Schueneman, 2017).

Apart from this, there are several other constraints when a cushion is being designed, for example, the end-user requirements, that may need unique project characteristics for the design to securely house a product in need of absorbing protection. The final package prototype will require then specific testing to estimate and evaluate its performance and integrity when exposed to conditions to which it was designed to withstand.

### 2.2.1. Shock performance and integrity test

Similarly to the shock performance test performed for the evaluation of cushion material, as in the ASTM D4168-95 (2015) standard, prototype testing also requires flat impact testing to understand how deceleration is transmitted through the cushion with the support of accelerometers coupled to the carried product. Known standard ASTM D5276-98 (ASTM International, 2017b) covers the necessary procedure for the evaluation of a container and its inner packaging to protect the desired product from sudden shock present in the moment of free fall Impact and to compare it with other packaging proposals.

One thing that is important to keep in mind when performing this test is that it is intended to find the package input deceleration, and for this matter, it is necessary to ensure that product being carried is as rigid and geometrically uniform as possible. In this way, it will be determined the packaging input deceleration and not the product response to impact, which would happen in the case where a product presents suspended components with different mass values that would excite the product's response (Schueneman, 1993).

Unlike performance testing, which refers to the study of cushioning's capability to absorb impact and vibration frequencies dangerous to the product assembly, the integrity of a packaging design refers to the ability of the protective unit to withstand the forces present in the distribution cycle without contracting too many structural damages. The ASTM D4169-16 standard (ASTM International, 2016) reviews test plans consisting in a sequence of integrity test procedures that correspond to threatening conditions that the packaging may come across depending on its distribution environment. The ASTM D4169-16 standard specifies that the whole practice must consist in defining the shipping unit; establishing an intensity level for testing; determining acceptance criteria; selecting a distribution cycle that most carefully associates with the product delivery, from those referred and planned in the standard; checking the detailed test sequence to which the product will be subjected to, depending on the distribution cycle chosen before; selecting test samples; conditioning samples in terms of temperature and humidity; performing the tests; evaluating results; documenting test results; and, finally, monitoring shipments to verify if the damage observed in the laboratory tests corresponds to that occurred in the distribution cycle. The tests utilized in this standard for correlation with hazard situations are those shown in Figure 2-8.

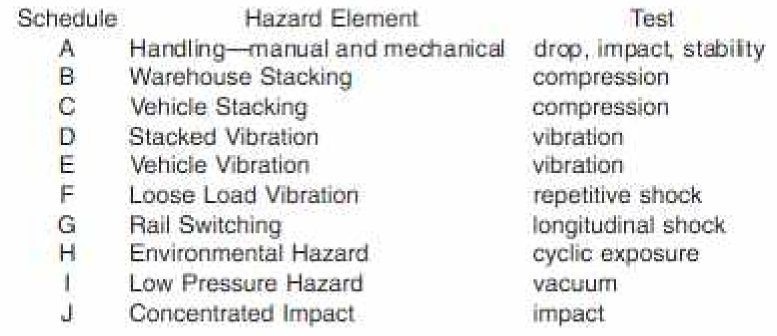

| Schedule | Hazard Element | Test |
|---|---|---|
| A | Handling—manual and mechanical | drop, impact, stability |
| B | Warehouse Stacking | compression |
| C | Vehicle Stacking | compression |
| D | Stacked Vibration | vibration |
| E | Vehicle Vibration | vibration |
| F | Loose Load Vibration | repetitive shock |
| G | Rail Switching | longitudinal shock |
| H | Environmental Hazard | cyclic exposure |
| I | Low Pressure Hazard | vacuum |
| J | Concentrated Impact | impact |

**Figure 2-8. Test sequence for integrity performance test. Source: (ASTM International, 2016)**

### 2.2.2. Vibration performance and integrity test

Once again, just as the vibration response test performed for the evaluation of a cushioning material, when a package system is designed there should be a vibratory evaluation test of its performance by subjecting it to a vibrational sinusoidal or random input which translates the frequency range experienced during transportation. With a product fixed to the cushioning and the assistance of an accelerometer, it is possible to assess if the design is such that attenuates the vibration frequencies near the product's natural frequencies.

In terms of vibration integrity, the cushioning must be tested to determine the robustness of the design and to assess if it will remain intact when presented to diverse vibrational frequencies, in a sinusoidal or random input. A possible standard that provides valuable information on a cushioning vibrational performance and integrity would be the ASTM D999-08 standard (ASTM International, 2015c). It states that the methods present in the document are able to measure the performance of the packaging in terms of its strength, and the safety it offers to its contents while being subjected to detrimental vibrations.

There are three different methods for vibrational testing contained in the standard referred before, and those are the Repetitive Shock Test, Single Container Resonance Test, and Vertical Stack Resonance Test. From this three, the one that is most suitable for testing the packaging strength and integrity is unquestionably the Single Container Resonance Test, that takes a test specimen resonance frequency search using either a sine sweep or a random vibration input, attaching accelerometers to the test sample to monitor maximum response frequencies. It is also advisable to insert an accelerometer on the vibrating platform to verify that the platform movement conforms to the desired input spectrum, and set up a transducer in a way that makes it possible to capture the package's natural frequencies in the direction of the table movement. After completing this process, the product remains in the vibration table for a specified length of time at each natural frequency revealed before.

If the designed system meets all shock and vibration requirements defined by the end-users, then the package is able to accomplish its desired job goal.

## 2.3. Evaluation Tests for Packaged Products

Packaged products will face different obstacles that may be detrimental to their integrity during transportation or loading and unloading processes. There should be taken, therefore, protective measures not only to ensure the viability of the interactions between the cushioning design and the packaged contents, but also to save time and money by testing a new model before starting full-scale mass productions. For this intent, evaluation tests on packaged products are performed by subjecting package-product units to stresses found in distribution in order to determine if requirements regarding deformations and stresses are met; to understand if a product design is being successfully developed; to help to solve problems and identify potential cost savings in current package cushioning design; and, finally, to assess the resistance of packages and products in controlled laboratory shock and vibration.

This section introduces free fall, inclined plane, and vibrations tests that make up the most critical tests and should serve as a basis for ascertaining the most crucial tensile field to which a product is subjected.

### 2.3.1. Freefall test

The drop test is one of the most frequently adopted criteria used to classify the package resistance to drop stresses and concentrated forces caused during handling, loading, and unloading of packages or even resulting from bad stacking in warehouses. As operators typically do not take the necessary security measures when handling shipped products, it is required to guarantee a sufficiently robust package to avoid any unwanted damages. Through a series of drops of a specified unit, it is possible to simulate a real transport environment to which the package will be exposed to and to predict any potential damage that might occur due to sudden shock stimuli.

The procedure performed to investigate the package-product response to the application of a series of drops can be observed and analyzed on standards such as ISO 2248:1985 (International Organization for Standardization, 1985), that aims to investigate the effects of a vertical impact as a single examination or part of a test sequence that intends to represent a continuous hazard state during a specific distribution system. The method of execution stated in the standard consists in raising a whirling arm, with the sample resting on its surface, to a pre-determined drop height, and then retreating the arm so that the package falls in the position on which it was resting.

Considering the movement executed by the arm and that the package drops in free fall, it is very likely that the product doesn't remain completely parallel to the ground during its descent. Having this in mind and knowing that accurate information won't be extracted if drop isn't performed well, the ISO regulation referred before also offers data on the angle tolerances that are accepted between the face, edge or vertex of impact with floor planar section, to confirm the test's quality.

The equipment and schematic set up used to conduct the examination are shown in Figure 2-9, where a mechanical drop test device is introduced. The different components of the device are the whirling arm used to hold the package, an accelerometer mounted on the unit to gather product's deformations (connected directly to a proper reading device), and a console to control the movement of the mechanical arm (Chen, 2014).

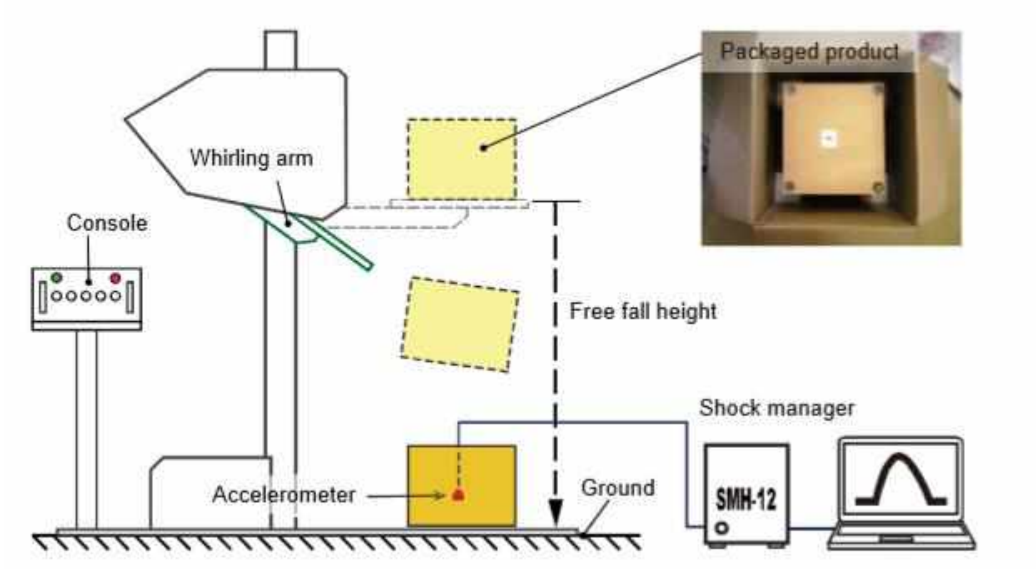

**Figure 2-9. Freefall test setup and equipment. Source: (Chen, 2014)**

### 2.3.2. Inclined plane test

Inclined plane testing is an impact testing strand used to determine the ability of a package to withstand the acceleration and compression stresses which may arise in connection with points of railcars and road transport hazards. This methodology has been found valuable in laboratory simulation of impacts that could occur in the handling of packages and may also permit observation of progressive failure of the unit and damages encountered on contents.

There are a series of standards on which the inclined plane test is reviewed, such as the ISO 2244:2000 (International Organization for Standardization, 2000a) and ASTM D880-92 (ASTM International, 2015b) standards. Using a guided test carriage, a flat test specimen mounting surface and an impact surface, the shock resistance of a product or its packaging can be determined (see Figure 2-10). Some important characteristics of the test machine, are that the guided test carriage is resting on an inclined plane with 10° of inclination with the horizontal where it will slide by the action of gravity before hitting the impact surface; the friction between the mounting surface and test sample should be enough to prevent it from moving during the whole sliding process, but such to let it move freely upon impact; and that the impact surface is desired to have its face perpendicular to the direction of movement of the test carriage. There should also be available proper instrumentation to measure the product velocity at impact.

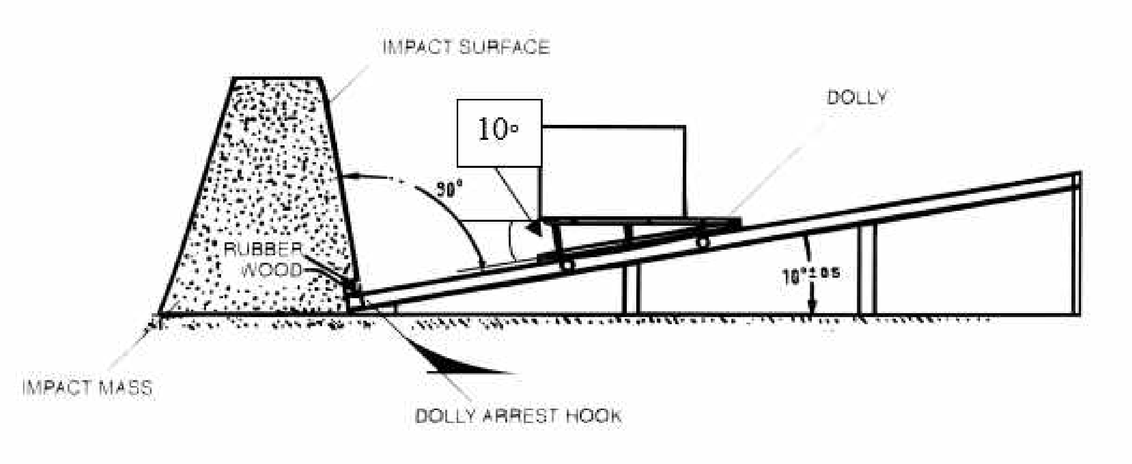

**Figure 2-10. Inclined plane test setup. Source: Electrolux**

The procedure starts by placing the testing unit on the flat platform with the edge that is planned to receive impact positioned slightly outside of the impact end of the carriage. The height from which the carriage should be released is the one that will translate the desired impact velocity previously decided for the test specimen. The test is then repeated the number of times needed for the failure of the shipping unit to occur, either at same impact velocity or by increasing the impact velocity at each cycle. It is important to highlight that the failure criteria are decided by the manufacturer, just as the sequence in which the edges are tested (ASTM International, 2015b).

### 2.3.3. Vibration test

As mentioned before, in vibration response testing for cushioning materials or for cushioning prototype testing, vibrations may occur in all forms of transportation and all levels of intensity, causing dynamic deflections that lead to product's malfunctioning. Since shipping units are subjected to intricate dynamic stresses when facing random vibrations, these tests are profoundly informative on the good correlation between the product and its packaging, or in other words, if the packaging is dampening its contents higher frequencies of vibration. When assessing a product's sensitivity to vibration, valuable information is also taken for packaging design suitable functioning abilities.

This test may be performed with either random or sinusoidal imposed vibration inputs, where each of the ways presents advantages over the other. Two of the standards that cover one of these types of vibration tests are the ISO 2247:2000 (International Organization for Standardization, 2000b) and ASTM D4728-17 standards (ASTM International, 2017a).

When performing the random vibration test, described in the ASTM D4728-17 standard, a vibration test system capable of applying essentially uniform vibrations when hosting a test specimen on the vibration table, is required. The vibration table should also be capable of producing controlled levels of continuously variable vibration amplitude over the predetermined frequency range for testing. There should be available electronic controls that have the aptitude to generate vibration system drive inputs to produce the desired power spectral density at the vibration table and to measure and control those levels at the table surface. The instrumentation used to aid the achievement of results in terms of the test specimen response are accelerometers, signal analyzers, conditioners and data display and storage devices.

The testing method for random vibration analysis consists initially on placing the test sample on the vibration table, making sure it can vibrate freely around the table surface, but attaching restraining devices to prevent excessive rocking of the product. Before the vibration test is conducted, it is necessary to ensure that the vibration levels do not overlap the one desired for the power spectral density, since very large and low-frequency displacements are going to be reached in an unpredictable way. Then, the test may be directed for the time needed to induce some type of damage on the unit being tested, or for a pre-determined length of time specified by testing or project engineers. If needed, the testing time or test level intensity may be adjusted to produce realistic testing parametrization (ASTM International, 2017a).

The random vibration test method produces some advantages when compared to a sinusoidal vibration sweep test, such as the fact that resonance buildups are less powerful than the ones happening during sinusoidal resonance dwell, which means that unrealistic damage due to resonance troubled build-up will be opposed. Confidence levels may be significantly enhanced if test results are compared with actual real field data representative of distribution cycle effects. Finally, random vibration may also be performed in any axis or in any package orientation.

On the other hand, in sinusoidal sweep tests, the vibration's intensity can become much higher than its correspondent prospects in the real world, which will help to guarantee a good design and validation margin. For the execution of the vibration test using a sinusoidal excitation pulse, the preparation and procedure of the ISO 2247:2000 standard (International Organization for Standardization, 2000b) is followed. The necessary equipment for the implementation of this test is practically the same as the one used for the performance of the test stated in the ASTM D4728-17 standard, with the difference in the vibration testing device, that should be capable of operating at a fixed peak-peak vertical component displacement and with the operational frequency range determined by the standard. The vibration table must also have a lower resonant frequency higher than the highest working test frequency performed in working stages.

To run the test, it must be verified that it is carried out in a similar environment to that experienced during the conditioning of the test specimen. The following steps are then identical to those verified in the random vibration test, starting prior to testing to lodge the product on the vibration table, and then subjecting it to the sinusoidal pulse. The specimen must be exposed to vibration in one of the two methods explicit in the standard. The first one demands that the test is operated at peak-peak displacement and at a fixed frequency within the range specified, to produce an acceleration of 0.5-1 G ensuring that the product doesn't separate from the table. Acceleration is normally measured in its peak sinusoidal value and is most commonly expressed in the dimensionless units of G's peak. Since acceleration, velocity and displacement are all frequency dependent, for a given frequency of operation held constant, the variation of one of these parameters will result in a proportional variation of the remaining and the other two outputs may be predicted. The second method implies that such acceleration must be used to make the product separate from the table, slowly increasing the frequency until repeated shocks are visualized. Finally, superimposed examinations may be performed to simulate the situation in which the packaging is transported in the low-end of a stack.

## 2.4. Relevant Standards

The procedures for each kind of package testing are normalized and established by several standard's organizations, such as ASTM International, Comité Européen de Normalisation (CEN), International Organization for Standardization (ISO), Technical Association of the Pulp and Paper Industry (TAPPI), International Safe Transit Association (ISTA) and even the Military. Many corporations and independent researchers resort to the modification of the existing procedures covered in the several standards to assess their particular requirements, either for specific product validation within a production company or an investigation requiring deviations from current methods.

For the evaluation tests of cushioning materials, standards specified in the earlier sections are summarized in Table 2-1.

The ASTM D1596-14 standard obtains specific dynamic cushioning test data from the cushioning material tested, such as the material cushion curve, to acquire comparable data for material's performance.

The ASTM D4168-95 standard not only evaluates the transmitted shock cushioning characteristics of foam-in-place materials but also evaluates it in the way they are supposed to be used, giving immediate conclusions about the efficiency of the foam for its product protection objective.

The MIL-HDBK-304C handbook, although it is not a standard, provides a very good insight on precise and organized procedures that have in mind effective cushioning design for a wide variety of applications. Scientific and practical Interactions are revised to formulate methods that take into account experimental data and valuable theoretical principles, converging the best possible practice. For the evaluation of cushioning materials particular purpose, Information on the vibration response of cushion samples to sinusoidal inputs is revised, so it can be obtained an amplification/attenuation curve for a certain combination of material type and thickness.

**Table 2-1. Standards for evaluation tests of cushioning materials.**

| Standard Code | Standard Name |
|---|---|
| **ASTM D1596-14** | Standard Test Method for Dynamic Shock Cushioning Characteristics of Packaging Material |
| **ASTM D4168-95** | Standard Test Methods for Transmitted Shock Characteristics of Foam-in-Place Cushioning Materials |
| **MIL-HDBK-304C** | Package Cushioning Design |

For the evaluation tests of packaging design prototypes, standards cited earlier are summarized in Table 2-2.

The ASTM D5276-98 standard specifies package design performance tests for the comparison of different designs, which use free fall methods to evaluate the capability of the cushioning to absorb sudden shock stresses.

The ASTM D4169-16 standard provides test methods which are representative of actual problems occurring in distribution, to estimate cushioning final design integrity qualities and structural stability.

The ASTM D999-08 standard offers procedures that replicate distribution frequency ranges, to comprehend if the packaging design is such that attenuates the product's hazardous frequencies. Other methods stated in the standard are also capable of testing the mechanical intactness of the package after being subjected to diverse types and intensities of vibrations.

**Table 2-2. Standards for packaging design testing.**

| Standard Code | Standard Name |
|---|---|
| **ASTM D5276-98** | Standard Test Method for Drop Test of Loaded Containers by Free Fall |
| **ASTM D4169-16** | Standard Practice for Performance Testing of Shipping Containers and System |
| **ASTM D999-08** | Standard Test Methods for Vibration Testing of Shipping Containers |

For the evaluation tests of packaged products, standards mentioned in previous segments are summarized in Table 2-3.

The ISO 2248:1985 standard specifies drop test methods for the investigation of the packaged product's response to vertical impacts.

The ISO 2244:2000 and ASTM D880-92 standards specify horizontal impact test methods, specifically inclined plane testing, for packaged products that encounter horizontal impact hazards during the distribution cycle.

The ISO 2247:2000 and ASTM D4728-17 standards stipulate vibration testing methods for packaged products using fixed frequency sinusoidal excitation, to judge the package strength and protection offered when low-frequency vibration is experienced.

**Table 2-3. Standards for evaluation tests on packaged products.**

| Standard Code | Standard Name |
|---|---|
| **ISO 2248:1985** | Packaging -- Complete, filled transport packages -- Vertical impact test by dropping |
| **ISO 2244:2000** | Packaging -- Complete, filled transport packages and unit loads -- Horizontal impact tests |
| **ASTM D880-92** | Standard Test Method for Impact Testing for Shipping Containers and Systems |
| **ISO 2247:2000** | Packaging -- Complete, filled transport packages and unit loads -- Vibration tests at fixed low frequency |
| **ASTM D4728-17** | Standard Test Method for Random Vibration Testing of Shipping Containers |

3

# Chapter 3 - Construction of the Numerical Model

This chapter discusses the methodologies and procedures used to construct the numerical model of the oven that will be treated and simulated in this work. To build this model, an initial evaluation was completed to comprehend what parts of the supplied model could be removed from the final numerical simulation since there was a great geometric complexity, as well as a vast set of constituent components, that would generate unbearable simulation time. These simplifications were performed with the concern of not compromising the finite element simulation, preventing out of line and non-compliant stress and strain results.

In this phase, the materials of each component were defined, as well as the properties of their sections and the connection and establishment of contacts between the various components in subassemblies in an effort to maintain their correct positioning and linking mechanisms, in order to constitute the final numerical model of the oven. It is of particular relevance to note that certain components were not intentionally geometrically modeled, and were added as mass elements to also permit a minimum simulation time. To make sure everything is properly connected and that the contacts are successfully modelled throughout the numerical model, several vibration modes tests were conducted as the assembly was being completed.

Completed the first iteration of the construction of the model, a first set of drop simulations were implemented to find any defects in the connection between elements, or even the lack of them. These simulations were performed only on the oven without its cushioning, to address faster relevant issues on the contacts and links between parts, to make sure the oven model was all set up and well-functioning when the simulation was carried with all the constituent components.

Once this iterative process was concluded, the beginning of the final simulations took place with every part, in order to discover the final assembly issues.

To conclude the development of the numerical model, many time consuming tasks were performed to produce the desired output, and different controls were used to produce output results with a good correlation to the experimental testing.

## 3.1. Geometric Model

Both a geometric and a physical model were supplied by Electrolux, found in Figure 3-1, which have proven to be very useful in the comprehension and analysis of the real structure of the oven, such as its embodiment and overall assembly. This initial work was crucial to understand the sub-assembly organization of the model's components, to further recreate the finite element model from scratch, taking into account the assembly of each set and the existing connections needed to be made.

The physical model depicted in Figure 3-1 b) was totally deconstructed and a deeper study was successfully achieved for both connections and materials of each component since the oven is composed of a great number of parts that are coupled to several different ones. There are, although, several screw holes in both CAD and physical model that were not being used, since this was an updated model with a few features changes when compared to the previous one, and there is always an attempt by the manufacturer to reduce the unnecessary material used which will lead to a reduction in the production cost of the new model. For this purpose, some screws were intentionally removed as they were not producing any major effect on the bonding of components and, thus, a lot of material is saved in each oven produced. It is important to point out, though, that the pallet found in the physical model of Figure 3-1 b) is not present in the geometric and numerical model, nor in the drop test simulations.

**Figure 3-1. a) Geometric model of the oven with packaging. b) Physical model of the oven with packaging.**

The specific location of components and their purpose for the overall operation of the oven were also considered. To conclude, some non-structural components were omitted from the mesh as they did not bring any benefit to the finite element model simulation.

## 3.2. General Aspects of the Numerical Model

### 3.2.1. Overall Definitions

A finite element model was first provided by Electrolux in an *LS-PrePost software* (Livermore Software Technology Corporation (LSTC), 2019b) readable file. The model consisted in the packaging module, composed by the bottom, left and right cushion, the top cardboard packaging, and the foil used to compress the assembly elements; and the mechanical structure of the oven, composed by its structural elements and accessories, which together fill in the full functionalities of the model. All the parts were geometrically modeled and the finite element mesh was generated by the finite element software *Hypermesh* (Altair Engineering, 2018). The overall finite element model provided, presented a number of 187570 shell elements, 324407 solid elements, 1637 beam elements and 9 mass elements to constitute a total number of 513623 elements.

Although the model provided was fully modeled in geometrical and meshing terms, it presented numerous errors and the lack of several controls needed to promote the simulation of the model. These controls, which will be described in detail during this chapter as the model is being shaped, include the necessary contacts between the various components, the presentation of boundary conditions, and the final simulation controls that deliver the various outputs of the simulation. Since the process of construction of the numerical model was unknown, it was of great difficulty to correct all the present errors given there was no previous information about the steps followed to obtain the final model received. Having this in mind, it was decided to recreate the numerical model from scratch, by simply leveraging mesh files and organizing them into multiple subassemblies to make them as easily accessible and organized as possible, in order to reduce the likelihood of errors and failures due to the lack of necessary controls.

The creation of the *LS-PrePost* file does not allow the declaration of units for each quantity entered to characterize the built numerical model, therefore it is the user's responsibility to introduce a coherent system of units. The recommended unit systems are shown in Table 3-1 (Livermore Software Technology Corporation (LSTC), 2018b), having been chosen the system C, since not only is the unit system usually used in this software but also does not conflict with the units of the numerical model of the oven.

**Table 3-1. Recommended unit systems.**

| | **A** | **B** | **C** |
|---|---|---|---|
| **Length unit** | meter | millimeter | **millimeter** |
| **Time unit** | second | second | **millisecond** |
| **Mass unit** | kilogram | ton | **kilogram** |
| **Force unit** | Newton | Newton | **kiloNewton** |

This means that the oven was modeled in millimeters and it also happens to be much easier to use the units of GPa, kN, and ms for, for example, detailing the Elasticity Modulus (E) for the materials used, applied loads and total simulation times, which will have to be greatly reduced due to the complexity of the model. Another reason is that the key moment to analyze is the short time interval when the oven hits the ground, and the large deformations that occur consequently and during this moment of impact.

Several *LS-PrePost* keyword cards were used during the development of the numerical model, being these the ones shown in Table 3-2. Summarizing the meaning of these keywords, having the mesh files imported to a new file, it starts by defining the material and section properties/element formulations of each part (that can be accessed in the keyword *PART) using the keywords *MAT and *SECTION. The information regarding the nodes and elements exchanged are all contained in the *NODE and *ELEMENT keywords, that present each node coordinates and which nodes were used to compose a particular element.

**Table 3-2. Keyword cards used in the numerical model.**

| **Keyword Card** |
|---|
| *Constrained |
| *Contact |
| *Control |
| *Database |
| *Define |
| *Element |
| *Hourglass |
| *Initial |
| *Load |
| *Mat |
| *Node |
| *Part |
| *Section |
| *Set |

The *CONTACT keyword card is posteriorly used to define interactions between components, such as parts in contact with other parts, and nodes from certain parts that need to be "glued" to other sections as they share some kind of attachment. It happens that sometimes more than one component is attached to a specific part, and when this happens, it is quite common to use the *SET keyword card to configure a set of parts or nodes to be implemented in the *CONTACT keyword.

Going back to the mass elements that were configured to substitute some of the parts that weren't intentionally modeled, these are elements composed by only one node needing to be connected to the rest of the structure. This is where the *CONSTRAINED card comes into play, creating from the mass element a nodal rigid body connected to other deformable bodies, and sharing nodes with these ones where the rigid body would settle if it was actually modeled.

The gravity condition is created with the aid of *LOAD keyword card and the *DEFINE keyword card where it is possible to define the acceleration of gravity (g) during the simulation time. To once again reduce unnecessary simulation time, the model has been placed closer to the ground section, and the *INITIAL keyword was used to impose an initial velocity value for the oven at the location where it was stationed. The rest of the keyword cards used in *CONTROL and *DATABASE were necessary to specify termination times, time-step scale factors, other controls to stabilize the simulation, and the desired outputs to be printed and subsequently investigated. All of these definitions will be thoroughly discussed at a later stage of this chapter.

### 3.2.2. Assembly of the Numerical Model

To facilitate the construction of the numerical model, this one was distributed in numerous subassemblies for a methodical assembly process to be created. In this way, the location and connections of each component are easily noticeable and installation faults are greatly reduced.

To start with, the numerical model was divided into four different subassemblies, being these the Cavity Assemble, the Housing Assemble, the Door Assemble, and the Cushioning Assemble. The first one is composed of the Cavity and all the accessories and other major components that are directly connected or linked to the Cavity structure. The Housing Assemble consists of the housing panels which serve as protection and to cover interior components, such as the ones belonging to the Cavity Assemble. The Door Assembly is pretty straight forward, and consists of the parts constituting the oven door, such as the heat retaining glasses and the handle to open the door, and including the hinges that connect to the Cavity Assemble and allow the angular opening of the door. Finally, the Cushioning Assemble is composed of the bottom and lateral cushioning, the top cardboard protection and the foil that is used to compact and compress the cushioning into the oven, to certify that the deformations of the appliance are somewhat limited. With no further ado, the numerical representation of each of the subassemblies will be presented to provide a better understanding of what parts are included in each group.

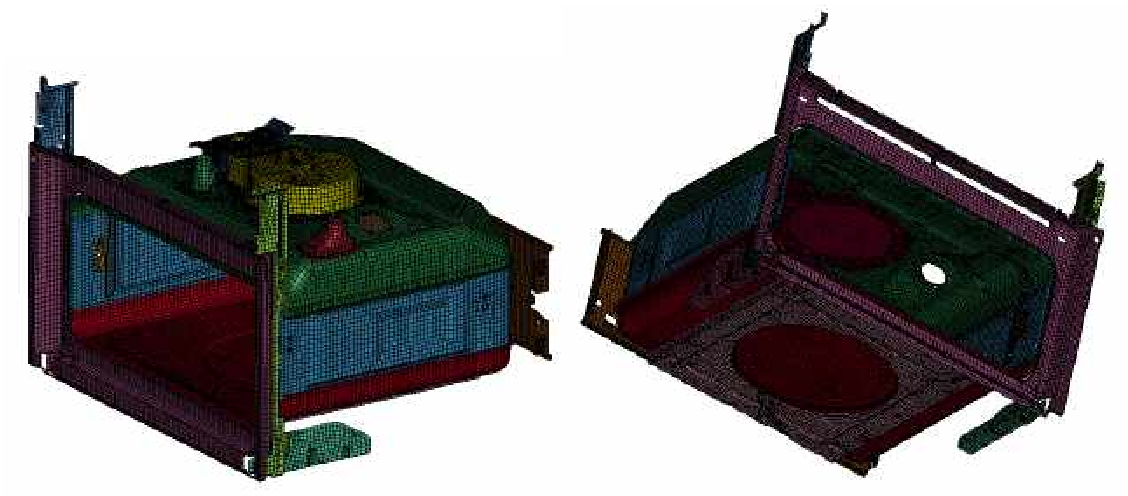

**Figure 3-2. Numerical representations of the Cavity Assemble.**

As seen in Figure 3-2, the Cavity Assemble is composed of a total of 27 different numerical parts. The assembly process starts in the cavity itself and moves to the first set of added components, where are found the waveguide, the “plate, component microwave”, the mica sheet, the magnetron, the pipes, the fan protection, the frame front, and the plate partition. After this first set, there is a second one composed of components which are not directly connected to the cavity, but to other important parts that are included in the first group. These are the bottom element protection (connected to the “plate, component microwave” and to the frame front), the brackets (connected to the frame front) and both supports which are in turn attached to these referred brackets. It is important to mention that not all of these connections are of the same kind. Some are screwed connections, others are welded (tied) connections, and there are even contact connections by means of restriction through contact between components.

In Figure 3-3 it is possible to observe the Housing Assemble. This assembly is composed by 36 different numerical parts, and its mounting process starts by connecting all four exterior housing parts, that are the housing bottom, the side panels, the housing back panel, and the top panel. There are only screw connections between the mentioned components. The next step is to join the carrier, which is a component that rests on the side panels and, as the name says, carries a variety of accessories and electronic components that are responsible for the operation of the oven. These accessories are the housing and cover fan condensation, the cooling channel and the transformer. To facilitate the building process, both the front metal panel and the glass panel were also added to this assembly group, with these components bolted to the top panel.

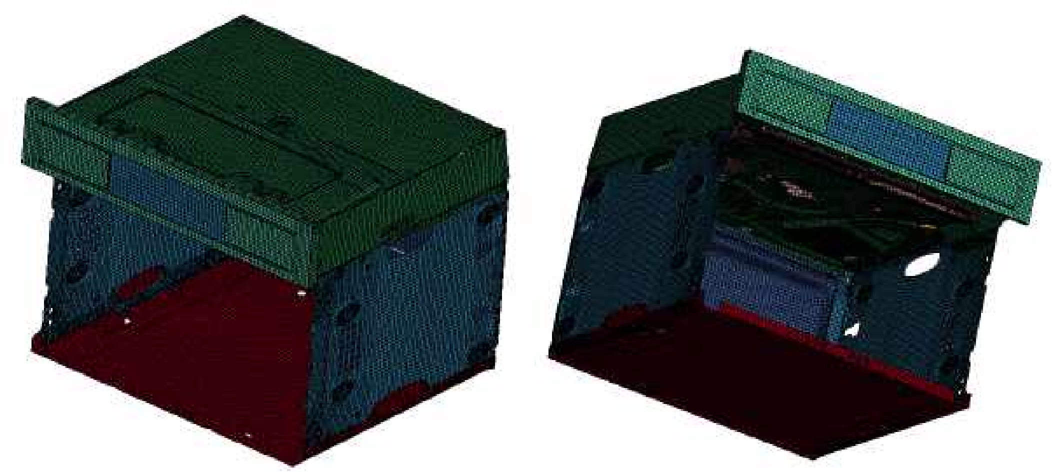

**Figure 3-3. Numerical representations of the Housing Assemble.**

With both the Cavity and Housing Assemble completed, it is required to determine which elements of each assembly allow the interconnection of both groups. With the aid of the geometric model (represented in the last section), screwed connections are found between the side panels (Housing) and the brackets and supports (Cavity), between the housing bottom (Housing) and the brackets

(Cavity), and also between the side panels (Housing) and the "plate, component microwave" (Cavity). Simple contact connections may be also found, as the top panel (Housing) is resting on both brackets (Cavity), and the frame front (Cavity) is resting on the carrier (Housing), each providing simple support to the components lodged on its surface. The union of both clusters is represented in Figure 3-4.

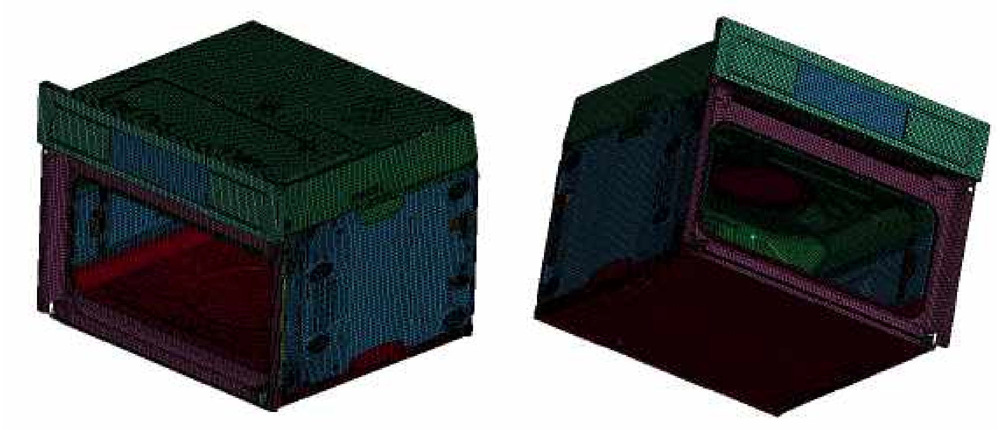

**Figure 3-4. Union of the Cavity and Housing Assembles.**

The Door Assemble, presented in Figure 3-5, is rather the most complex assembly process of the four since it exhibits the largest number of parts and varied interfaces between each constituent component involved. It is composed of 94 diverse numerical parts, but where 70 of these belong to the same component. The idea behind the montage of this assemble, is to start from the outside in. This means that the first two connected components are the front inox door and front glass, and the rest of the components will be constantly added from these.

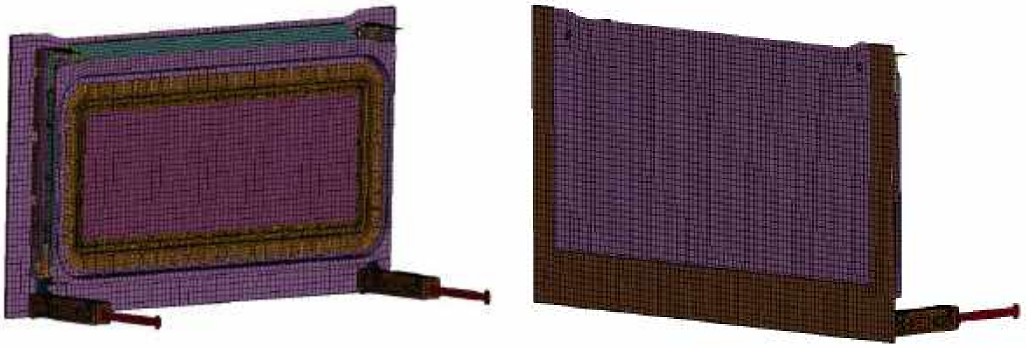

**Figure 3-5. Numerical representations of the Door Assemble.**

The sequence of operations starts by tying the column mw and the spacer to the front glass, moving then to the contact lockout of the hinges and the glass center on the column mw, and finally adding all of the choke fragments to the assemble. The choke is directly linked to the column mw through bolt connections. The interconnection of this assemble to the previous ones is described in Figure 3-6, where it is seen that the system is easily restricted from separating itself from the rest of the model by a simple contact constraint between the column mw (Door) and the frame front (Cavity). The hinge is also resting on the support parts owned by the Cavity Assemble.

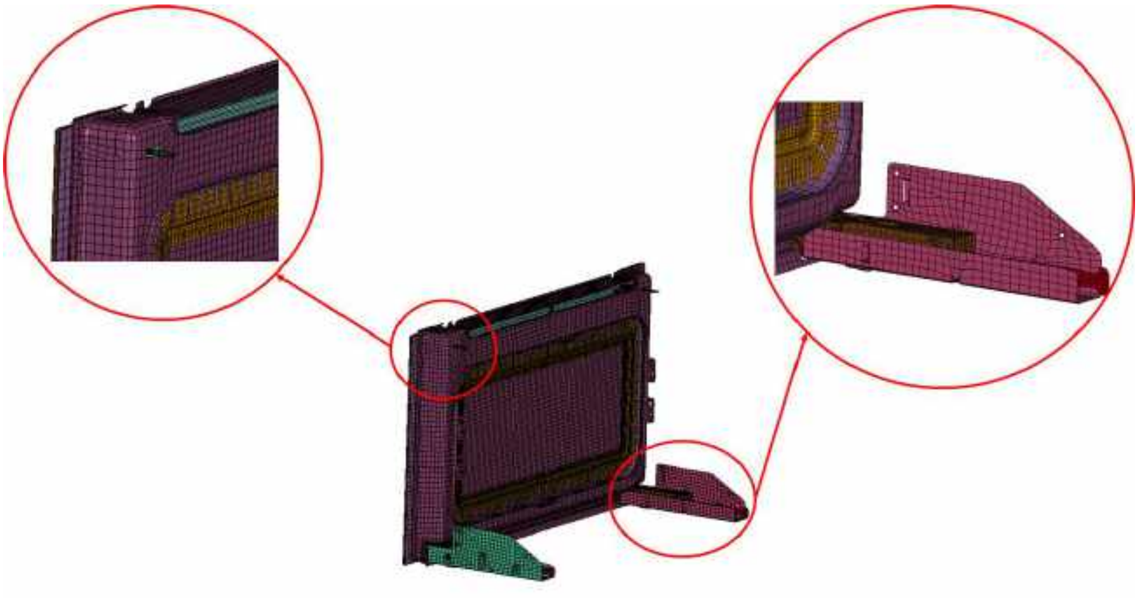

**Figure 3-6. Connections between the Door and remaining assembles.**

With the acquisition of all these three assembles, we have at our disposal the numerical model of the complete oven structure. The last set of components, designated as the Cushioning Assembly, is not directly integrated into the furnace structure and was conceived, as already mentioned in the previous chapter, to protect the furnace during transport. The design of each piece of protection has been carefully crafted to provide the best possible shock protection. There are five different components belonging to this assembly, which are the bottom cushioning, the two lateral cushioning, the top cardboard protection, and the foil enclosure that is wound around the packaging to tighten the entire assembly. It is important to underline the fact that the bottom packaging's base where the oven foundation rests, is meticulously designed so that the base of the oven sits perfectly on it and to make sure bouncing is circumvented. All of these defined components are elucidated in Figure 3-7.

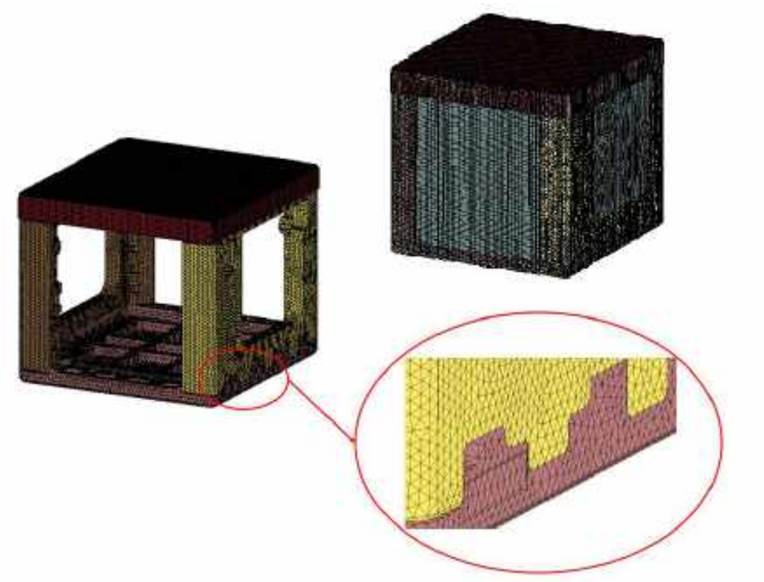

**Figure 3-7. Numerical representations of the Cushioning Assemble.**

The interior design of each packaging module can be assessed in Figure 3-8, where the crucial shape selected absorbs most of the impact energy when the oven impacts the rigid ground. It is needless to say that the bottom cushioning is the vital component protecting the oven structure on the rear surface and edge drop simulation.

**Figure 3-8. Foam packaging module design.**

### 3.2.3. Numerical Simplifications

Through a careful analysis of the various components of the geometric model, it was possible to understand which simplifications could be performed and which of these could be neglected, while not influencing the results of the numerical simulations. This analysis resulted in the removal of some components that were neither structural nor relevant to the structural behavior of the numerical model, allowing a reduction in computational costs:

- The support of the trays (side grid microwave) (see Figure 3-9), situated inside the cavity, was not contained in the numerical model, since they are not structural in nature and therefore will not resist any detrimental forces suffered by the oven at the moment of impact.

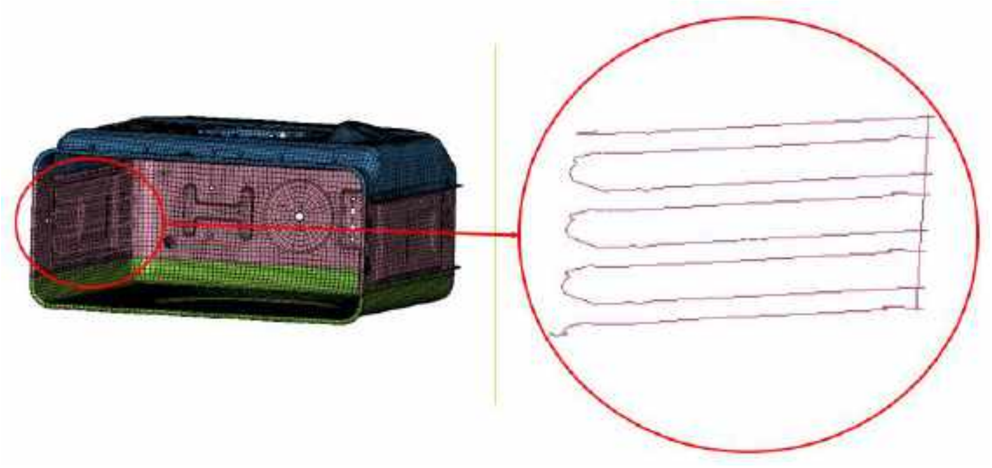

**Figure 3-9. Support of the trays' location.**

- The bottom heating grate (tubular heating element standard bottom) and its support (see Figure 3-10), which is connected to the bottom element protection, are located directly below the cavity, with the role of being a heating element that provides heat to the interior of the cavity. These are, therefore, not necessary to integrate the numerical model as they are not structural parts that will withstand stresses suffered by the oven, and since its weight is minimal when compared to the total mass of the oven.

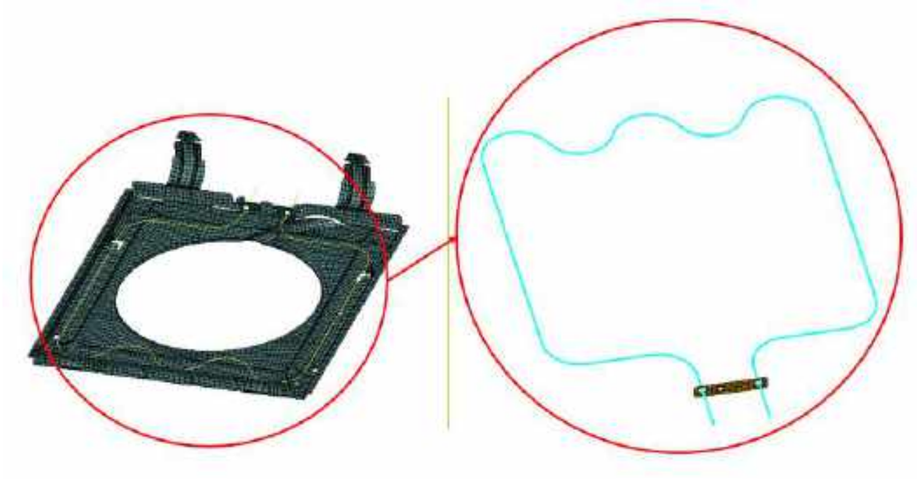

**Figure 3-10. Bottom heating grate location.**

- The lateral heating grate (heating element ring microwave) and its horizontal support (see Figure 3-11), connected to the cavity middle and located behind the fan protection, have the selfsame function and are extracted for the very same reason as the lower grate.

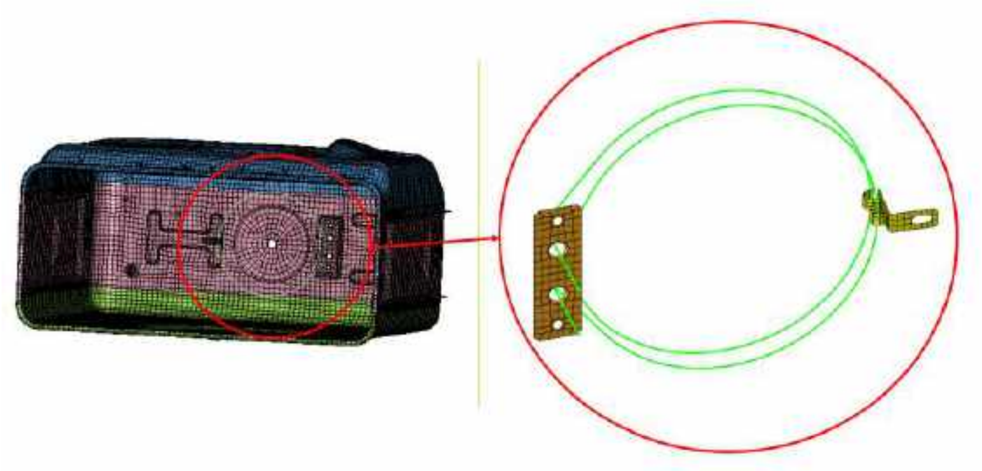

**Figure 3-11. Lateral heating grate location.**

- The upper heating grate (heating element top) and its supports (see Figure 3-12), connected to the top cavity, are once again removed for the same reason as the side and bottom grate and have precisely the same functional characteristics as those mentioned.

Figure 3-12. Upper heating grate location.

- The connecting elements between the handle and the oven door (adapter short) (see Figure 3-13), are also negligible non-structural parts which do not cause substantial forces or moments in the parts to which they are attached, or even in the remainder of the structure.

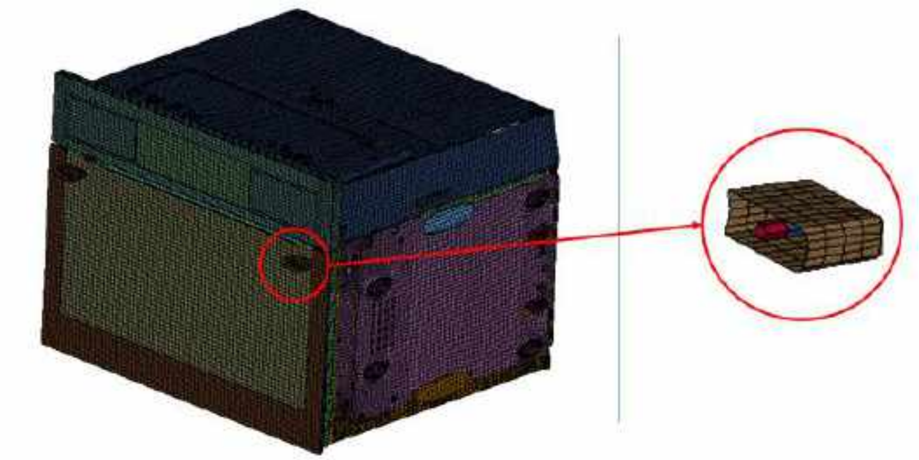

Figure 3-13. Handle accessories location.

- The small rubbers located on each hinge (silicon seal door cover) are parts with negligible weight and were only introduced into the model to compensate for thermodynamic effects that arose during the operation of the oven (see Figure 3-14). The only functionality of these rubbers is to prevent the passage of humidity into the door.

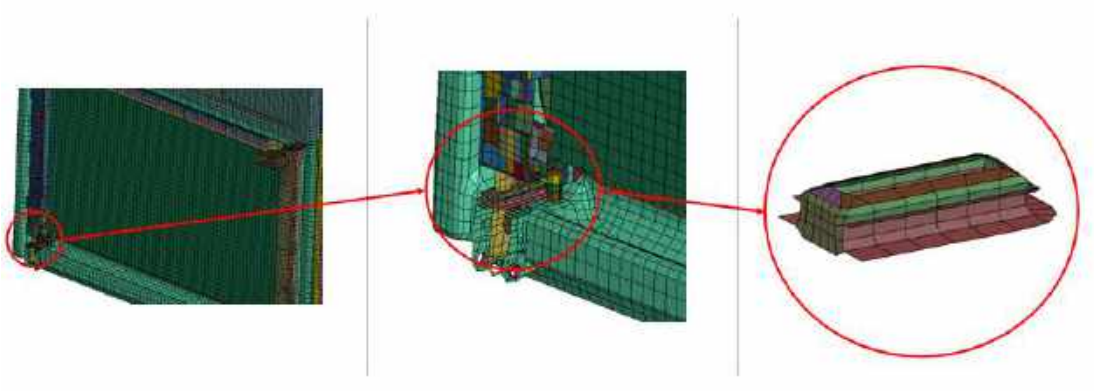

**Figure 3-14. Small rubbers location.**

- The component named "plate partition" is located below the cooling channel and resting on the carrier with the purpose of facilitating the heat distribution and airflow from the small fan to which it is connected (see Figure 3-15). It was later modified and discontinued in the current model of the oven that is the target of this analysis. For this reason, it was also subtracted from the numerical model to be simulated.

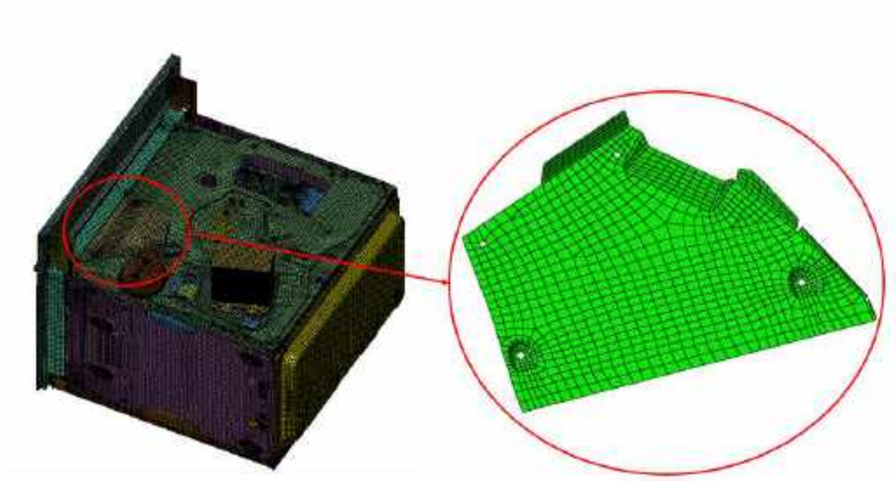

**Figure 3-15. Plate partition location.**

- Another simplification performed was the modeling of the screws using techniques consisting of the use of Beam-type elements. This technique will be comprehensively explained in later sections.

Although the weight of each removed component alone is comprehensively small when compared to the total mass of the oven, the sum of all masses can exhibit a substantial extent that should not be discarded from the simulation. With this in mind, in the following section, a detailed review of the total mass of the oven and of the numerical model is held so that the values of both are similar and realistic results are gathered for the various outputs of the simulation.

It is important to note that, as already mentioned, this approach is an iterative process and some of these components have been removed from the finite element model after ascertaining their behavior or influence during the simulation process.

### 3.2.4. Total Mass of the Model

For the results observed after the simulation of a drop test to be realistic in respect to structural stresses and displacements, it is mandatory that the total mass of the numerical model is in conformity with the total mass of the oven model that is being analyzed. To assist this comparative analysis, Electrolux provided a spreadsheet with the list of components and various relevant properties about them, such as material type, volume, density, and mass of each part.

Since some parts were removed from the numerical model, the sum of the mass of the remaining components (not considering the mass elements posteriorly added) had a value of 32.948 kg. Through the performance of a vibration (or eigenvalue) analysis of the model on the *LS-DYNA software*, the mass of the numerical model can also be extracted and displayed a value of 32.815 kg for the sum of all nodal masses (as seen in Figure 3-16). Once again, this mass concerns only the modelled parts and not the additional mass elements.

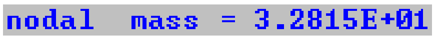

```
nodal  mass = 3.2815E+01
```

**Figure 3-16. Nodal mass sum.**

To determine the precision of the numerical mass when compared to the theoretical real oven mass, the percent error was calculated with Equation 3.1.

$$\%_{error} = \frac{|mass_{numerical} - mass_{theoretical}|}{mass_{theoretical}} * 100 \tag{3.1}$$

The value of the relative percent error of 0.374 % is quite small and the difference in mass can be considered to be practically negligible. It is important, though, to understand where this difference is coming from. The reason for this difference then comes from the fact that there are small differences between some of the density values established in the spreadsheet and the finite element model provided. Since the model provided contains the most recent model characteristics, the mass found in the finite element model is considered to be correct, even while observing that the error between the theoretical and numerical values is insignificant. It is also worth mentioning that the density for each component deviates slightly from the actual value of each material used so that the final weight of each numerical component is sufficiently close to the actual mass recorded.

As there are a vast number of screwed connections that consist of utilizing rigid beams, the total mass for these rigid elements was assessed using "Measure" inside the *LS-PrePost software's* "Element Tool" set of controls. All rigid connections were compiled as one part, this being the part number 21, since the material properties would be the same for all bolted connections. Observing the plot of the value of the part's mass over a certain simulation time (see Figure 3-17), it is possible to conclude that the total screw mass is given by the value of 0.2508 kg.

If this mass is added to the nodal mass of all modelled parts observed before ($m_{numerical} = 32.815$ kg), the new total mass will be of 33.0658 kg. This mass was not compared to the one observed in the spreadsheet since that mass sum does not count with the mass of the bolted joints, and as mentioned above, only considers the modelled parts.

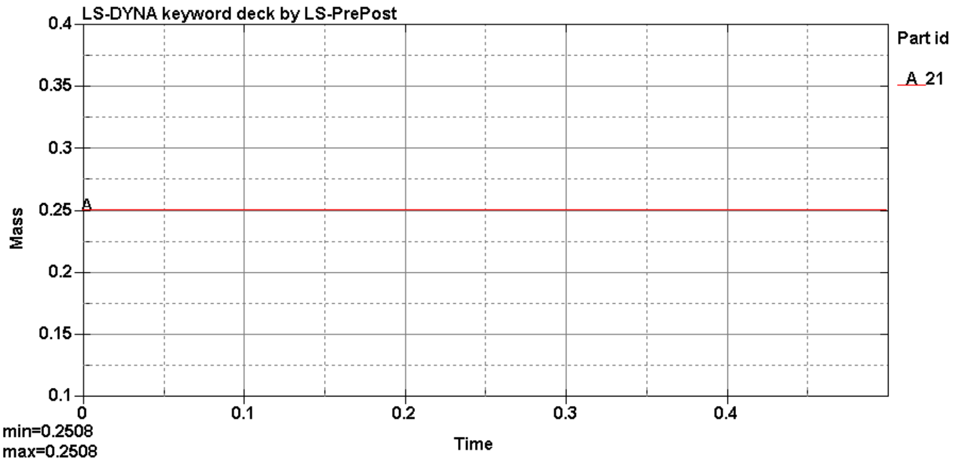

**Figure 3-17. Total screw mass over the simulation time.**

What also contributes to the total mass of the oven are the mass elements incorporated into the assembly to supersede the modelling of some components. Although a detailed view of this subject is later exposed in future sections, it is necessary to review the total mass value of these elements to account for and find the total weight of the oven. There are a total of eight different mass elements, and their mass and corresponding component can be assessed over Table 3-3.

**Table 3-3. Mass elements present in the numerical model.**

| Component | Mass, kg |
|---|---|
| **Electronics, OVC3000** | 0.1536 |
| **Magnetron, Opole** | 0.8566 |
| **Capacitor** | 0.1808 |
| **Circuit board vision** | 0.0546 |
| **Cooling fan** | 0.8628 |
| **Interlock LH** | 0.0356 |
| **Interlock RH** | 0.0356 |
| **Motor, hot air** | 0.5064 |

The sum of all these masses gives a total value of 2.686 kg, coming only from mass elements. Adding this mass to the previously seen total mass (already accounting for the screws) of 33.0658 kg, the final total mass for the numerical model will be of 35.7518 kg. It is clarified in the spreadsheet, though, that the estimated mass of the physical oven model has a value of 42.96 kg. Given this mass difference of 7.2082 kg, the numerical simulation could not provide realistic results of the oven stresses and deformations since the analysis was not being conducted with any safety coefficient, quite the contrary. For this particular reason, a ninth mass element was added to the numerical simulation, and positioned on the center of gravity of the oven model so that the missing mass would be accounted for as well.

It is important to point out that if the model contained the removed components, the total mass would be slightly increased, considering that the mass sum of these removed parts is of 1.9883 kg (taken out from the bill of material properties present in the spreadsheet). This mass sum is, therefore, implicitly included in the mass difference assigned to the oven assembly's center of gravity location ($\Delta m = 7.2082$ kg), and this is considered a reasonable simplification seeing that the removed parts are well distributed around the oven's center of gravity, instead of being concentrated on a narrow location.

With these modifications achieved, the new final model has a number of 176578 shell elements, 324407 solid elements, 832 beam elements and 9 mass elements to constitute a final number of 501826 total elements.

## 3.3. Characteristics of the Employed Materials

Through the content contained in the spreadsheet referred to in the previous section, it was possible to distinguish the various constituent materials of the diverse components operating in the oven. Table 3-4 shows the materials that constitute the physical model of the furnace to be studied, which will be used to define the materials of the components considered in the numerical model. The various characteristics presented are the modulus of elasticity (E), yield stress ($\sigma_y$), tensile strength ($\sigma_t$), Poisson coefficient ($\nu$) and density ($\rho$).

It is possible to observe several types of material that fall into the various existing classes of materials, these being metals, polymers, ceramics and composites. Within the category of metallic materials, can be found enameling steel

(ASTM A424 Type II), galvanized steel (Commercial steel (CS Type B) and S250 GD + Z140), cold rolled carbon steel (Structural Steel Grade 25), aluminium alloy (AlSi10Mg), stainless steel (Type 430), and structural steel (CK45). The EPS foams and the soda lime float glasses fall under the polymeric material and ceramic material category, respectively. There is also a wide variety of composite materials, such as the Grodnamid polymer composite, the mica filled Teflon (PTFE) and the corrugated fiberboard.

**Table 3-4. Materials present in the numerical model.**

| Material | E (GPa) | $\sigma_y$ (MPa) | $\sigma_t$ (MPa) | $\nu$ | $\rho$ (kg /mm$^3$) |
|---|---|---|---|---|---|
| **DIN 55471 EPS foam 27.5** | 0.002908 | | | 0 | 3e-8 |
| **DIN 55471 EPS foam 20** | 0.00689 | | | 0 | 2e-8 |
| **Corrugated Fiberboard** | 0.5 | | | 0.3 | 9.5e-8 |
| **ASTM A424 Type II** | 200 | 180 | 300 | 0.29 | 7.87e-6 |
| **ASTM A653M - 18 Commercial steel (CS Type B)** | 200 | 283 | 365 | 0.29 | 7.87e-6 |
| **ASTM A1008M – 18 Structural Steel Grade 25** | 200 | 170 | 290 | 0.29 | 7.87e-6 |
| **DIN EN 1706:2010 AlSi10Mg** | 65 | 200 | 335 | 0.33 | 2.67e-6 |
| **Grodnamid PA6-GF30-1 PA66** | 8 | 144 | 145 | 0.35 | 1.35e-6 |
| **ASTM A240M – 18 Stainless Steel Type 430** | 200 | 310 | 483 | 0.3 | 7.7e-6 |
| **Glass – Soda Lime Float Clear Tempered and Toughned** | 72 | | | 0.23 | 2.5e-6 |
| **DIN CK45 steel** | 200 | 450 | 585 | 0.29 | 7.85e-6 |
| **DIN EN 10346:2015 S250 GD + Z140** | 200 | 250 | 330 | 0.29 | 8e-6 |
| **PTFE, Mica Filled** | 1.45 | | | 0.35 | 2.3e-6 |
| **Glimmer (Stone) “MICA”** | 2.07 | | | 0.35 | 2.9e-6 |

Foam properties will be explained in detail in the “Cushioning Material Modeling” sub-section, in order to justify the totality of the values found in Table 3-4. The shrink foil material is a thermal shrinking low-density polyethylene (LDPE) with its material attributes supplied by the Electrolux material database, since it exhibits a variation of its mechanical properties as a function of temperature, as displayed individually in Annex 1.

### 3.3.1. Elastic Material Modelling

Reinforcing the idea that the construction of the numerical model is an iterative process that has the possibility to undergo changes according to the treatment of results obtained after each iteration in the creation of a realistic simulation, it is necessary to start this dynamic procedure in a simplistic way and subsequently make changes that are necessary to obtain viable results.

To initially characterize the behavior of each material used, except for the cushioning foam and foil material, the hypoelastic isotropic material model was used. To correctly represent the chosen model the material card *MAT_ELASTIC is used. To define this keyword card, it is only necessary to provide the modulus of elasticity, Poisson’s coefficient and density of the representative material.

This first approximation is fairly practical, considering to begin with that all the oven components remain in the elastic regimen during the entire impact and simulation time. If by chance this assumption is not correct, that is, if some of the components exceed the value of the yield stress after the impact with the ground, the elastic material model may not be sufficient to correctly characterize the existing plastic deformation and consequently, the actual deformations that occur. It is remarked also that the hypoelastic material model may not be stable for large elastic strains, so if this would occur, a hyperelastic material model (*MAT_002) would provide a more accurate approach (Livermore Software Technology Corporation (LSTC), 2018c).

For metalic material components, if the plastic regime is reached, the option that best characterizes the behavior of the material in these conditions is the model of elasto-plastic material with linear hardening, represented in Figure 3-18.

To represent this material model in the *LS-PrePost software*, the utilized material card would be the *MAT_PIECEWISE_LINEAR_PLASTICITY. To define this card, additionally to those necessary for the definition of the *MAT_ELASTIC card, it is also required to provide the material's yield stress value (that if necessary, can be found in Table 3-4) and a tangent modulus to describe the plastic strain experienced as a function of the stresses that befall on each component. Once again, if large elastic strains are experienced before yielding, a hyperelastic formulation can also be used instead with the keyword card *MAT_FINITE_ELASTIC_STRAIN_PLASTICITY, but only for solid elements. The only concern when using these material types compared to the use of the elastic material models, is that the computational cost could be moderately increased. In these types of simulations containing a large number of elements and vast geometrical complexity, it is desired the decrease of computational effort at the utmost extent.

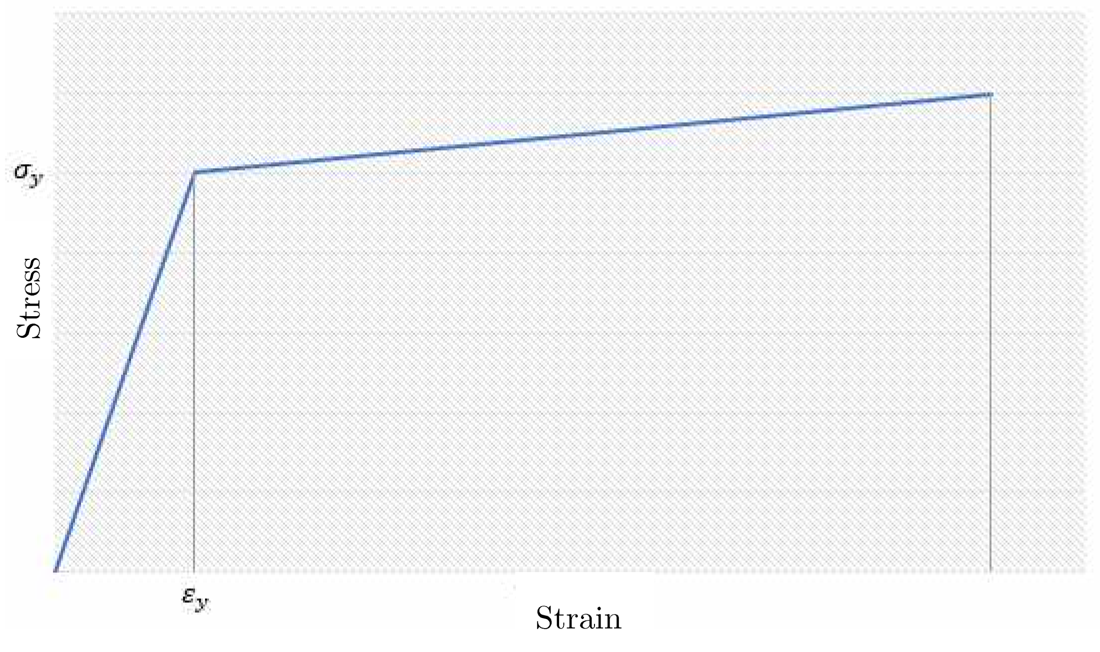

**Figure 3-18. Elasto-plastic with linear hardening material model.**

For the polymeric composites, the same principles and material models can be used when plastic strain is experienced, but there are also a few other very good representative material cards for plastics and thermoplastics. Examples of these are the *MAT_PLASTICITY_COMPRESSION_TENSION and the

*MAT_SAMP-1 which can better describe the complex material behavior of plastics. A recent study was carried by P. Reithofer and colleagues (Reithofer, Fertschej, Hirschmann, Jilka, & Rollant, 2018) to give a good comparison between these widely used material models for plastics, and to provide an overview on each card's advantages and disadvantages when representing the behavior of polymers in different types of loading situations. The particular issue with using far more complex material models, is the difficulty of defining all the parameters required for the correspondence with the material model in question.

To define ceramic materials, particularly glass, apart from what was referred for metallic materials, there are also diverse viable materials cards available. The most widely used material model in *LS-DYNA* for this purpose, is by far the *MAT_JOHNSON_HOLMQUIST_CERAMICS, which is based on the Johnson-Holmquist 2 (JH-2) material model, developed to facilitate the modelling of brittle materials subjected to large loading conditions (Johnson & Holmquist, 1994). The implementation and validation of this material model into *LS-DYNA* was also performed by Cronin and colleagues (Duane S Cronin et al., 2003), to show that it precisely replicated the published data for simple single element validation cases.

### 3.3.2. Foil Material Modelling

During the packaging process of the final assembly, after securing the oven frame within the cushioning assembly, the entire set is wrapped with a plastic foil produced in LDPE so that it remains compact and the vibrations are reduced to a minimum. The main feature of this foil is the fact that it shrinks due to thermal heating. This feature allows an increased compression of the assembly and greater protection of the goods being transported. In order to portray the behavior of this material considering its thermal shrinkage, the material card *MAT_ELASTIC_PLASTIC_THERMAL was used, as proved to provide a good representation of thermal shrinking in a work by Neumayer et al. (Neumayer et al., 2006). It should be noted that for the performance of the thermal shrinking simulation, a separate analysis from the drop test is performed to provide the values of compressive stress caused by the plastic foil in the cushioning assembly, which will in turn be retrieved and included in the simulation of the drop test.

To define this material model, one must provide the LDPE mass density, and at least two Young's Modulus, Poisson's ratio and coefficients of thermal expansion at two different temperatures. In order to define all of these parameters, some assumptions were made, since some of these values couldn't be obtained from the provided data (Electrolux's spreadsheet and Annex 1) and needed to be sourced from the foil's supplier.

The two different temperatures considered were 25°C and 150°C, since the plastic foil's mechanical properties for ambient temperature were already provided through the spreadsheet, and the information stated in Annex 1 was obtained for a heating process up to 150°C. Since the only relevant information in Annex 1 was tensile strength and breaking elongation, the material's behavior was assumed to be purely elastic, and fracturing when it reaches the maximum tensile strength value and respective elongation. As the modulus of elasticity is the slope of the elastic regimen of the material, from the Hooke's Law (Equation 3.2) it is possible to know the value of this one.

$$\sigma = E.\varepsilon \Leftrightarrow E = \frac{\sigma}{\varepsilon} \tag{3.2}$$

Where $\sigma$ represents the ultimate tensile strength of 28 MPa, and $\varepsilon$ represents the breaking elongation corresponding to this tensile strength which is taken to be 500%.

The variation of the Poisson's ratio with temperature is not stated in Annex 1, but a study from Nitta and Yamana on Poisson's ratio and mechanical nonlinearity under tensile deformation in crystalline polymers shows that for LDPE, Poisson's ratio appear to be insensitive to temperature fluctuations (Nitta & Yamana, 2012). Thus, the value of the Poisson's ratio remained the same for both temperatures considered.

The thermal expansion coefficient ($\propto$) can be identified in different sources and presents of minimum value of $10 * 10^{-5}/°\mathrm{C}$. The minimum value was employed as it presents the most disadvantaged situation, since the compression will be the minimum corresponding to this type of material, and therefore will allow the achievement of results with structural safety. The value was also taken to be negative to ensure the shrinking of the plastic foil onto the oven assembly when thermal loading is applied. In Table 3-5, the various parameters needed to define the material model of the foil material are shown.

**Table 3-5. LDPE mechanical properties at two different temperatures.**

| Temperature (°C) | E (GPa) | ν | ∝ (x$10^{-5}$) | $\rho$ (kg/mm$^3$) |
|---|---|---|---|---|
| **25** | 1.1 | 0.38 | 250 | 9.24e-7 |
| **150** | 0.0056 | 0.38 | 1500 | 9.24e-7 |

To code how the temperature variation happens over time, the card *LOAD_THERMAL_LOAD_CURVE must be used in combination with this material card to display the heating process of the foil. As mentioned, the temperature will vary between 25°C and 150°C, in this case during 40 ms, following the procedure held in the study by Neumayer et al.. The thermal load applied through time is described in Figure 3-19.

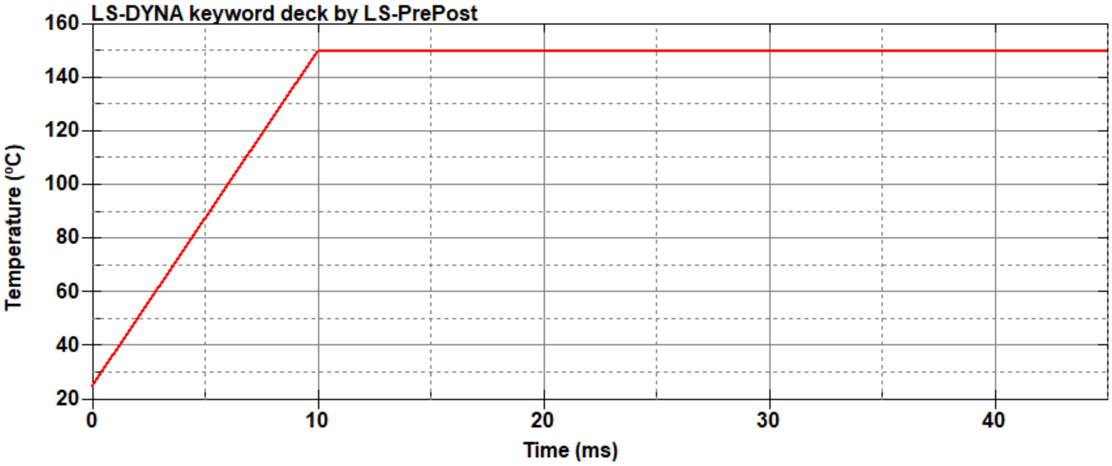

**Figure 3-19. Thermal load curve.**

As this is a coupled structural thermal analysis, there is a need to define a thermal material model, represented in this case by the card *MAT_THERMAL_ISOTROPIC. Since heat transfer is not one of the concerns in this analysis, to define this material card only the structural density of the foil was included.

To specify that this will be a coupled structural thermal analysis, *CONTROL_SOLUTION must also be activated with the SOLN parameter set to 2. Lastly, the controls *CONTROL_THERMAL_SOLVER and *CONTROL_THERMAL_TIMESTEP are utilized to stipulate that this will be a transient analysis with the symmetric direct solver, and to specify that it will be fully implicit. Other controls were used, as for example *CONTROL_TERMINATION to indicate the termination time (40 ms), to ensure a stable simulation. These will all be explained in detail in the "General Final Simulations Results" section, as it is more pertinent its description later on.

As a last and vital observation, a control called *INTERFACE_SPRINGBACK_LSDYNA was also assigned. This command allows the generation of a *dynain*-type file at the end of the thermal pre-stressing simulation, where the stresses and strains in each part are included. The *dynain* file contains information about the updated nodal coordinates, the pre-stressing and initial strains of the cushioning components (as these are the parts which are in contact with the plastic foil) expressed in terms of the *INITIAL_STRESS_SOLID and the *INITIAL_STRAIN_SOLID cards. Then, after the simulation is finished, this file is withdrawn and included in the drop test simulation, by modifying the keyword (*.k*) file and applying the *INCLUDE card.

### 3.3.3. Cushioning Material Modelling

To define the cushioning performance, which is a crucial element in the protection of the oven at impact, the material card *MAT_CRUSHABLE_FOAM was required. To replicate the foam behavior, *MAT_ELASTIC could not be used (as the simplification made for the other components), since the cushioning directly affect how to oven will deform, depending on the damping offered by the packaging material characteristics. The packaging module is made out of Expanded Polystyrene Foam (EPS), and since foams present a highly complex and varied behavior, a large number of material models are accessible in the LS-DYNA library to define lots of its different types. Based on works from Shah and Topa (Shah & Topa, 2014) and Bielenberg and Reid (Bielenberg & Reid, 2004), the best candidate and one of the easiest to use to characterize the EPS foams, is the referred *MAT_CRUSHABLE_FOAM. To define this material model, it is necessary to provide the mass density, the modulus of elasticity, the Poisson coefficient, a stress-strain curve, the tensile stress cutoff, and the damping coefficient.

The stress-strain curve required, is more specifically a stress versus volumetric strain curve, and can be obtained from a compressive stress versus deformation percentage curve provided in the spreadsheet supplied by Electrolux. The reason why these curves are somehow equivalent is that the volumetric strain is simplified to be equal do the compressive strain detected in the foam.

The volumetric strain, which is given by the ratio between the change in volume of a deformable body and its original volume, may be clarified by:

$$\frac{\Delta V}{V} = \frac{(\sigma_1 + \sigma_2 + \sigma_3)(1 - 2\nu)}{E} \tag{3.3}$$

Where $\sigma_1$, $\sigma_2$ and $\sigma_3$ are the principal stresses, $\nu$ is the Poisson's coefficient, and E the modulus of elasticity. Since the curve available provides the compressive stress, it is known that there is only an applied force in one direction and, therefore, a stress component in that specific direction. Assuming that the direction of compression is the same as the first principal direction, then $\sigma_2$ and $\sigma_3$ are known to be zero. Also, based on the work of Shah and Topa (Shah & Topa, 2014) about modeling large deformation and failure of EPS crushable foam using *LS-DYNA*, Poisson's coefficient is taken to be zero. This was proved by the experimental tests conducted in this study, where no lateral elongation was observed during the compression of the test specimen. It was found out that there was no volume conservation throughout the compression test, and instead the density would increase over the course of the test. The analysis previously carried on the work by Bielenberg and Reid (Bielenberg & Reid, 2004) on modeling crushable foam for the safer racetrack barrier, also underpinned this validation.

These considerations allow for the streamline of the volumetric strain formula:

$$\frac{\Delta V}{V} = \frac{\sigma_1}{E} \tag{3.4}$$

What makes the volumetric strain equal to the compressive strain, as discussed in the first place. Therefore, the only noticeable change in the EPS' volume is the change in the compressive depth.

Having this information, the foam stress-strain curves provided by Electrolux, are detailed in Figure 3-20. Both curves are necessary since the lateral and bottom cushioning present different mass densities and the compressive strength increases with the increase of the latter.

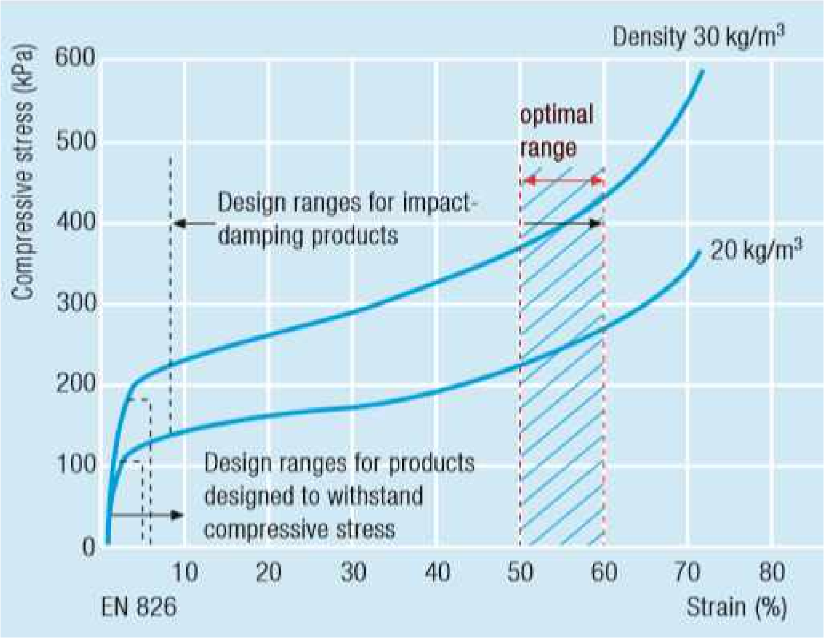

**Figure 3-20. EPS Foam stress-strain curves. Source: Electrolux**

To import these curves' information to *LS-PrePost*, they need to be discretized at several points and inserted into the software. As all the available data is the image showed in Figure 3-20, a *Matlab* code created by Ana Patrícia Martins was implemented to read the image and return the coordinates of selected curve points. For this to happen, one must alter the image in an editing program, placing some pixels of the curve in a different color from the rest of the colors featured in the image. The limits of each axis must also be clarified so that the program can relate the points of space where the pixels are located to its position on each axis. Discretizing each curve (for 20 and 30 $\mathrm{kg/m^3}$) into 31 different points, the coordinates were introduced in the numerical model to represent the cushioning performance. From these curves, it is also possible to extract the value of the modulus of elasticity (E) by analyzing the slope of the initial part of the curve. If the point located at the end of this line segment is known, and recognizing that the curve starts at the graph's origin, the slope value is trivially determined.

The remaining unknown parameters, the tensile stress cutoff, and the viscous damping coefficient, were obtained from the work developed by Ozturk and Anlas (Ozturk & Anlas, 2011) where they studied in detail the finite element analysis of EPS foam used in packaging under multiple compressive loading and unloading. All of the parameters needed to define the cushioning material model in *LS-PrePost* are summarized in Table 3-6.

**Table 3-6. Cushioning material model properties for both foam densities.**

| Parameter | Description | Value for EPS20 | Value for EPS30 | Units |
|---|---|---|---|---|
| **RO** | Density | 2.04192e-8 | 3.1993e-8 | kg/mm$^3$ |
| **E** | Modulus of Elasticity | 0.002908 | 0.00689 | GPa |
| **PR** | Poisson's Coefficient | 0 | 0 | |
| **TSC** | Tensile Stress Cut-off | 0.0001 | 0.0001 | GPa |
| **DAMP** | Viscous Damping Coefficient | 0.5 | 0.5 | |

### 3.3.4. Negative Volume in Soft Materials

Foams are highly soft materials that undergo deeply large deformations. In Finite Element Analysis, when deformable bodies are modelled with this type of material model, its elements may be deformed in such a way that the volume of the element is calculated as negative, causing the simulation to stop due to negative volume error, without the material reaching a failure criterion. There are, although, plenty of possible controls to avoid the termination of the calculation (JPD, 2003).

The first consideration was to set the erosion flag for solids to 1, to invoke the erosion of any solid elements whose volume becomes negative. Even with this control set as described, a negative volume may cause a simulation error. Being the reconstruction of the mesh at specific locations to accommodate particular deformation fields the last option, other remarks were also considered, as avoiding fully-integrated solid element formulations, increasing the viscous damping parameter of the foam model to maximum recommended value of 0.5 (which was performed and may be checked in the material properties of Table 3-6), and adding the optional contact card *CONTACT_INTERIOR to the cushioning part (JPD, 2003).

The reason behind avoiding fully-integrated solid element formulations is that the fully-integrated elements tend to have a less robust approach when dealing with large deformations. A calculation using these formulations will terminate much sooner with a negative jacobian, than that using 1-point element formulations, since a negative jacobian can occur at one of the element's integration points while the element as whole remains with positive volume. As the 1-point element formulations present only one integration point, the probability of this error to happen is somewhat reduced as compared to the previous formulation.

The optional contact card *CONTACT_INTERIOR must be used on soft materials that work under high-pressure compression since the negative volume error occurs due to the solid element's inversion, which will induce penetration into the underneath layer of elements. When this contact card is invoked, these interpenetrations between layer surfaces of solid elements' faces are prevented and, therefore, the negative volume of these elements is anticipated. To complete the definition of this card, the selected inner contact formulation (Attribute 4) is the Type 1, as it is recommended to handle uniform compression (Livermore Software Technology Corporation (LSTC), 2018b).

Allowing the erosion of solid foam elements, enables the simulation to continue even after the detection of elements with a negative volume, but may raise a problem if the elements on the upper surface of the foam erode and the constituent parts of the oven come into contact with the interior elements of the foam. (Shah & Topa, 2014). To prevent this occurrence, the contact type *AUTOMATIC_NODES_TO_SURFACE was used considering a set of nodes belonging to the cushioning foam to be in contact with the surface of the oven. This contact option is not only recommended for this particular case in comparison with the "surface to surface" contact type, but also presents a much lower computational cost in terms of speed and memory, which will be explained in detail in the "Definition of Contacts" section.

As a rule, *LS-DYNA* removes the mass of the elements that were eroded from the simulation to maintain the stability of the simulation. Although this is not a problem when the eroded elements are small in size, when manifested in large numbers the mass reduction can become excessive and lead to inaccurate simulation results. To ensure that this mass is computed, the ENMASS parameter in the *CONTROL_CONTACT card should be adjusted to a value of 1, thereby causing the mass of eroded nodes belonging to solid elements to be considered in the calculation and these nodes to remain active in the contact algorithm (Shah & Abid, 2012).

The last observation to be addressed is the fact that the stress-strain curve used to define the performance of the foam material model was obtained from a compression test whose maximum allowable strain value would be about 70-80% of the maximum possible value. The problem that this poses in the simulation has to do with the fact that in a drop test, due to the high kinetic energy achieved by the oven, the deformations of the cushioning elements may reach values above 70% of the foam length. For values above the last strain value found on the selected curve, the program extends the curve with the slope obtained from the last two recorded values, that is, the last slope of the curve. This can result in the corresponding stress value for the largest possible strain having a relatively lower value than what was anticipated in reality, and hence *LS-DYNA* will not be able to simulate the bottoming out effect that occurs at large compressive strains. To counteract this event, the curve must be manually extended exponentially to cover these large compressive strains to at least 95% (Shah & Topa, 2014). The difference between the initial and modified curve can be seen in Figures 3-21 and 3-22, respectively.

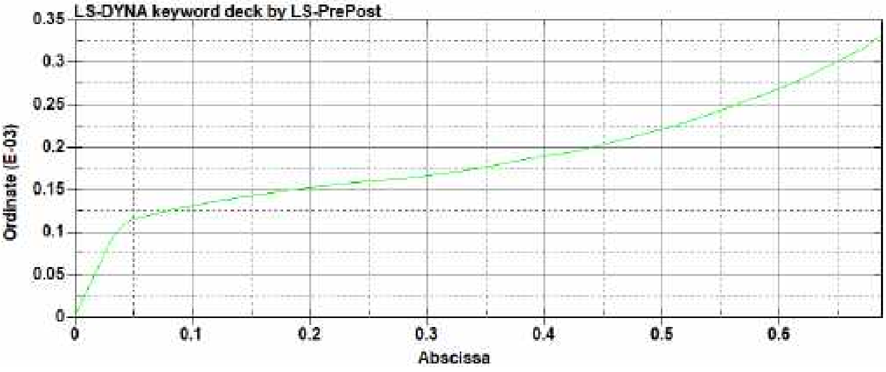

**Figure 3-21. EPS foam stress strain curve input in *LS-PrePost*.**

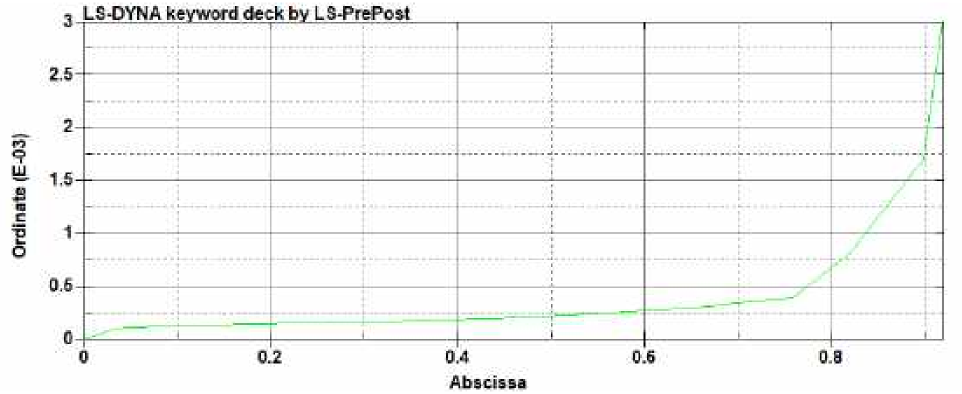

**Figure 3-22. EPS foam stress-strain curve with exponential extension.**

It is finally required that the modified curve is as smooth as possible. This process is basically based on stiffening-up the stress-strain curve of the material at large strains.

This approach is only required to be implemented on the bottom cushioning since this part is the key component sustaining the oven's loads under the impact condition. Due to the oven's weight compressing all the upper surface of this feature, considerable strains will be expected. The lateral cushioning will have a neglectable effect when the simulation is carried on the oven's surface and still have little impact on the edges' drop simulations, having much weaker deformations than those observed in the bottom foam.

### 3.3.5. Foam Material Model Validation

In order to validate the material model chosen to reproduce the foam behavior in *LS-DYNA*, a simple foam compression test was performed on three different samples retrieved from the physical cushioning sent with the physical model assembly by Electrolux. The compression test was conducted on three different test specimens with different dimensions from one another, being two of them extracted from the lateral cushion (with density equal to 27.5 $\mathsf{kg/m^3}$), and only one extracted from the bottom cushion (with density equal to 20 $\mathsf{kg/m^3}$). The reason behind this choice was the difficulty in extracting cushion samples with regular geometry and sufficient height to perform this test from the bottom cushioning, since its geometry was quite complex and with several fillets and ribs included. The specimens were also compressed until 80% of their initial length, and the compression rate was maintained constant through all three tests performed with a value of 0.5 mm/s.

The equipment used for the conduction of this test was a servo-hydraulic test machine (Figure 3-23 a)), two steel plates, the foam samples extracted from the cushioning components, an analogue module responsible for receiving the values extracted from the sensors contained in the machine and relaying them to the general processing unit (Figure 3-23 b)), and a console with the software provided by the machine manufacturer to control the parameters associated therewith.

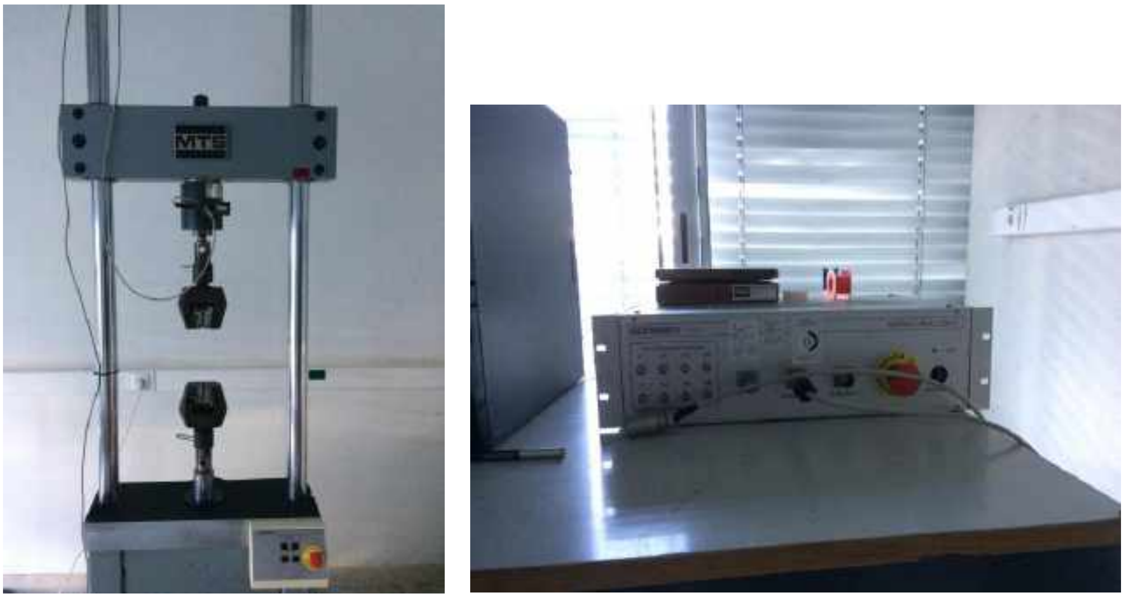

**Figure 3-23. a) Servo-hydraulic test machine; b) General processing unit.**

The procedure for this test begins by calibrating the punches at a height that takes into account the height of the foam to be tested, plus the height of the two steel plates that thus function as the base and compression plate for the test specimen. The two steel plates were required due to the tapered shape of the punches that would compress the foam sample concentrically in its core, and therefore these plates will allow constant compression throughout the specimen's entire height.

After calibration, the foam sample and the two steel plates are placed in the lower punch of the machine and through the console, the speed of the compression punch (upper punch) is imposed with a value of 0.5 mm/s. The punch movement is subsequently set corresponding to 80% of the sample height (Figure 3-24), since the curves that have been obtained from the literature are also achieved by the compression to around this range of strain values.

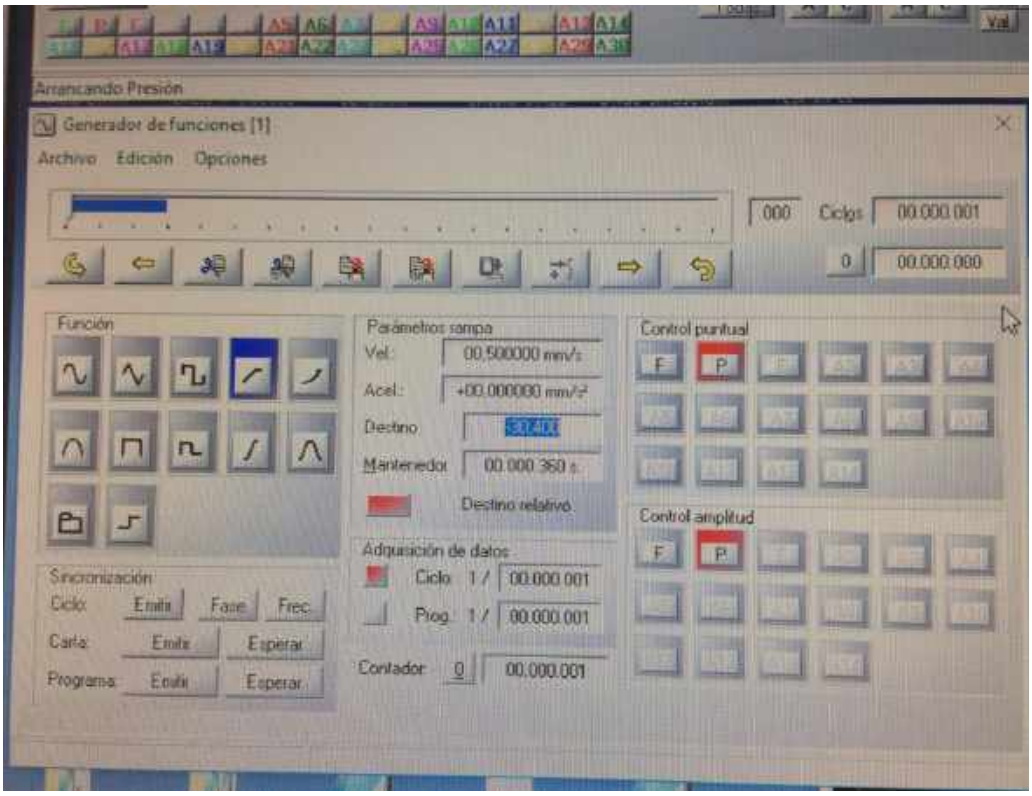

000 Ciclos 00.000.001

0 00.000.000

Vel: 00,500000 mm/s

Acel.: +00.000000 mm/s²

Destino -30.400

Mantenedor 00.000.360 s

Ciclo 1 / 00.000.001

Prog. 1 / 00.000.001

Contador 0 00.000.001

Figure 3-24. Punch movement setting.

Before the compression starts, it is still necessary to define which parameters will be described by the graph obtained from the data processing system. In this case, since the velocity is fixed constant, the desired graph will plot the force required for the movement of the punch as a function of its position at each instant. The graph being plotted while the punch is compressing the foam sample can be assessed in Figure 3-25, where it is possible to see that the plot line is growing in the negative force and position values. This happens because the upper punch is descending in height and applying a compression force on the specimen.

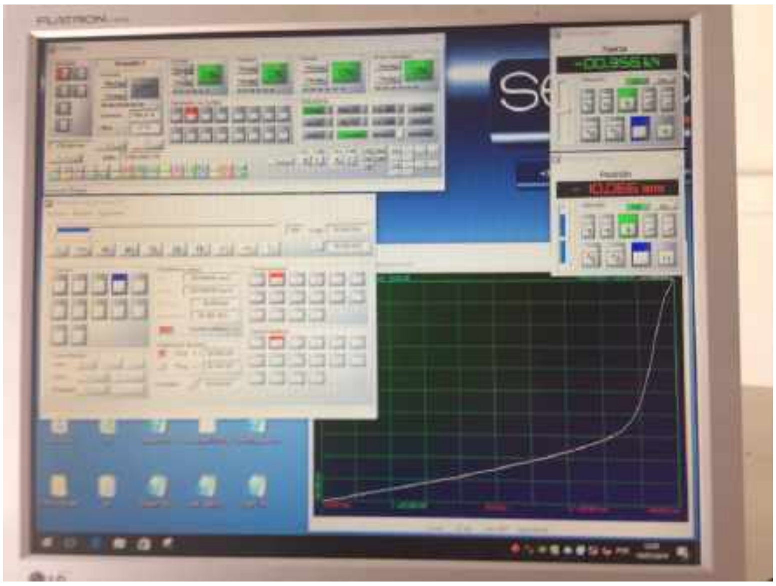

**Figure 3-25. Force-position graph plotted by the console.**

The first test specimen to be analyzed was retrieved from the lateral cushion (27.5 $\mathrm{kg/m^3}$) with the upper and lower surface dimensions of 41 by 39 mm and an associated height of 38 mm. The movement of the punch shall be of 30.4 mm, being this value 80% of the initial height of the specimen. Since the compression rate has a value of 0.5 mm/s, the strain rate was calculated as 0.01316/s. After compression (depicted in Figure 3-26), the compressed sample is measured to examine its final dimensions.

**Figure 3-26. First test specimen after compression.**

The final dimensions were measured as 41 by 39 mm for the superior and inferior cushion surfaces, and a value of 19 mm for the final height of the sample when the upper punch was reset to its original position. As there is no lateral elongation, it is proved that the EPS foam have zero Poisson's ratio and consequently, the volume is not conserved during compression. This implies that the density of the material increases while it is being compressed, as previously concluded by the study of Shah and Topa (Shah & Topa, 2014). From the final height length observed of 19 mm, it is also possible to conclude that there was an elastic recovery of around 50% of the initial length. Despite this, permanent deformation is observed due to the foam cells that collapse on the stress plateau region.

In Figure 3-27, one can observe the stress-strain curve for this given compression rate obtained from the force-position curve extracted from the console. Only the stress points up to an elongation corresponding to 70% of deformation in height were considered, since the curve of the literature with which this will be compared, was obtained for these strain values as well.

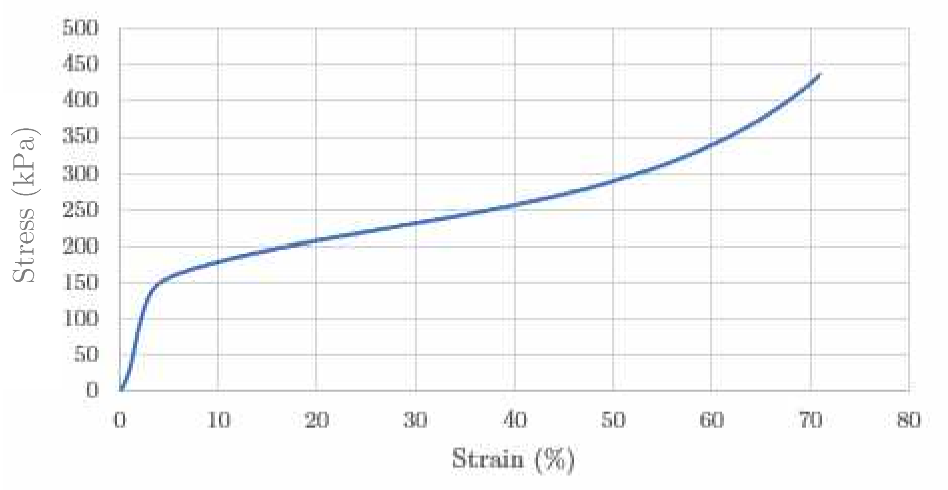

**Figure 3-27. Compression test stress-strain curve for the first test specimen.**

There are three different regions of deformation observed in this graph which are typical of EPS foams. These are: the linear elastic region (the foam behavior is almost linear elastic for small strains, being this slope the Young's Modulus for this foam material); the plateau region (where the foam cells begin to collapse due to elastic buckling, plastic yielding or brittle crushing (Belingardi, Montanini, & Avalle, 2001)) that characterizes the plastic behavior of the foam; and the densification region (where opposing cell walls meet which cause the stresses to increase sharply). Nevertheless, the transition point between the plateau and densification regions is not very clear due to the destruction of the foam cells and permanent damage (Shah & Topa, 2014).

As seen in the "Cushioning Material Modeling" section, the literature cushion stress-strain curve was obtained through the use of a program created in *Matlab* for the discretization of the curve in its various constituent coordinates. With this process, it was possible to obtain the stress-strain curve of this material for possible comparison with the curve obtained with the compression test performed on a specimen of the lateral foam. Thus, in Figure 3-28, it is observable that the progress of both curves is quite similar, although the one obtained from the literature corresponds to a density slightly higher (30 $\text{kg/m}^3$) than that observed in the lateral cushion (27.5 $\text{kg/m}^3$). Because of this density difference, both stress-strain curves could never be equal, and since it is not known any information on the strain rate at which the literature curve was obtained, this can also be a factor for the difference of stress levels obtained by each curve. It is known from experimental studies (Shah & Topa, 2014) that the highest the compression rate, the highest will be the stress needed to trigger the same strain.

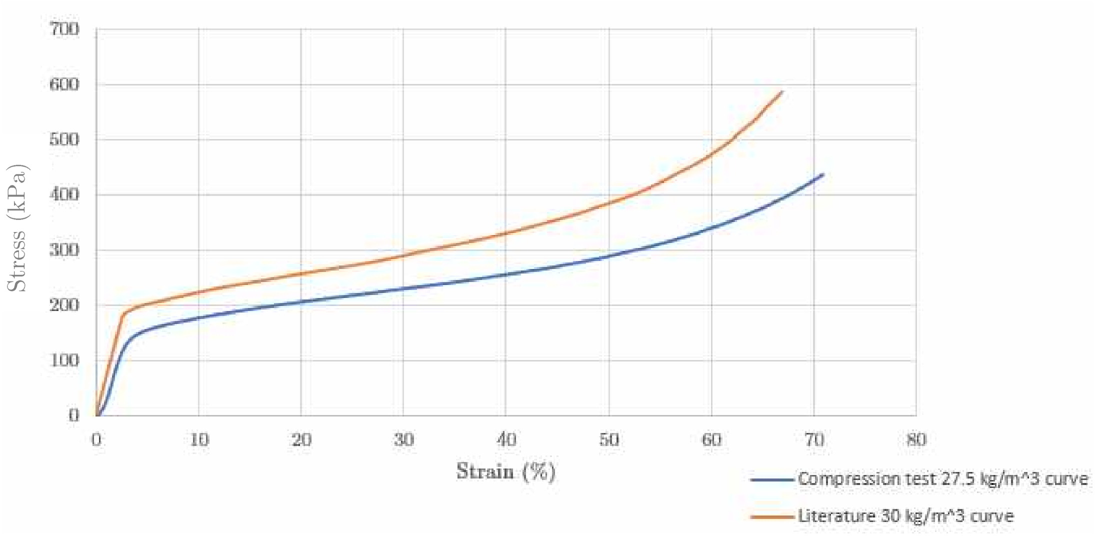

**Figure 3-28. Comparison between the Literature and Compression test curves for the first test specimen.**

The second test sample was extracted from the bottom cushioning (with density equal to 20 kg/m$^3$). The particularity with this sample is that the bottom cushion presents a highly complex geometry along its entire structure and for this reason, the only samples with uniform geometry that were possible to extract presents a fairly reduced height. In Figure 3-29, the only places in this cushion segment from which it is possible to collect samples with uniform geometry can be observed. As can also be seen, the thickness of material to be found in these regions is quite small. Due to this constraint, the sample used to perform the compression test was composed of two samples of equal geometry and positioned one above the other.

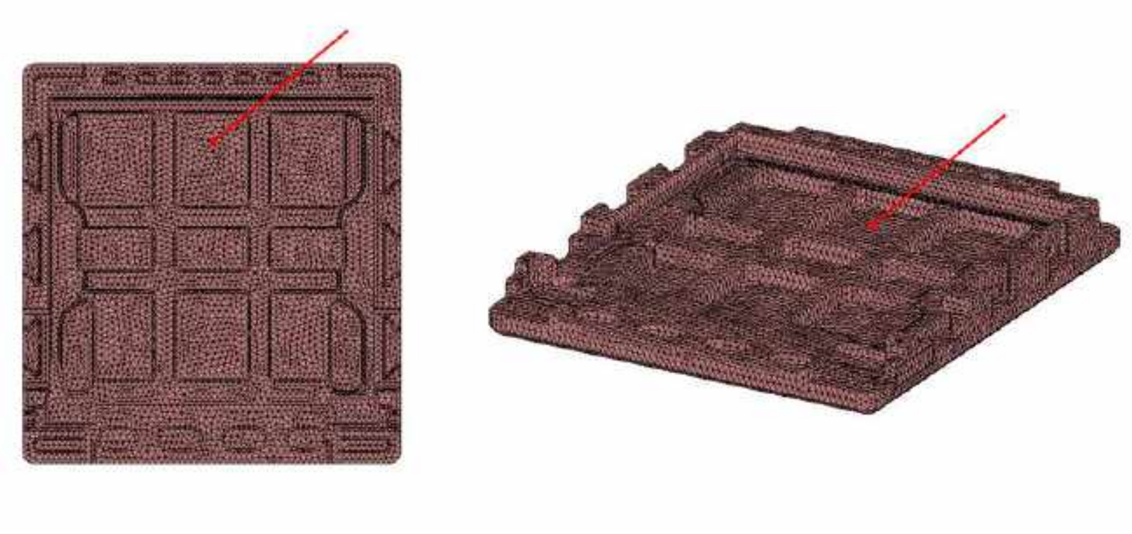

**Figure 3-29. Foam samples extraction location.**

The dimensions for each of these samples are of 88 by 103 mm for the upper and lower surfaces' sections, and a height of 15.5 mm, making a total height of 31 mm when both specimens are stacked. Whit this height, the motion of the punch must be of 24.8 mm to ensure compression of 80% in thickness. Since the compression rate has a value of 0.5 mm/s, the strain rate was calculated as 0.01612/s. After compression, the compressed sample was examined, being the final dimensions 88 by 103 mm for the superior and inferior cushion surfaces, and 19 mm for the final height of the sample when the upper punch was reset to its original position.

The same conclusions were drawn about the Poisson's ratio for this type of material, although it was not observed an elastic return up to 50% of the initial height dimension as in the first sample analyzed, but a return up to 61.3%. Although not concordant, it was expected that this would occur since the test specimen is not composed by only one sample, but two samples stacked. This leads to the absence of collapse of foam cells in the transition plane from one sample to the next and therefore the elastic return aggregated from each individual will be higher than the 50% previously observed.

In Figure 3-30, one can observe the stress-strain curve for this given compression rate obtained from the force-position curve extracted from the console. Only the stress points up to an elongation corresponding to 70% of deformation in height were considered, since the curve of the literature with which this will be compared was obtained for these strain values as well.

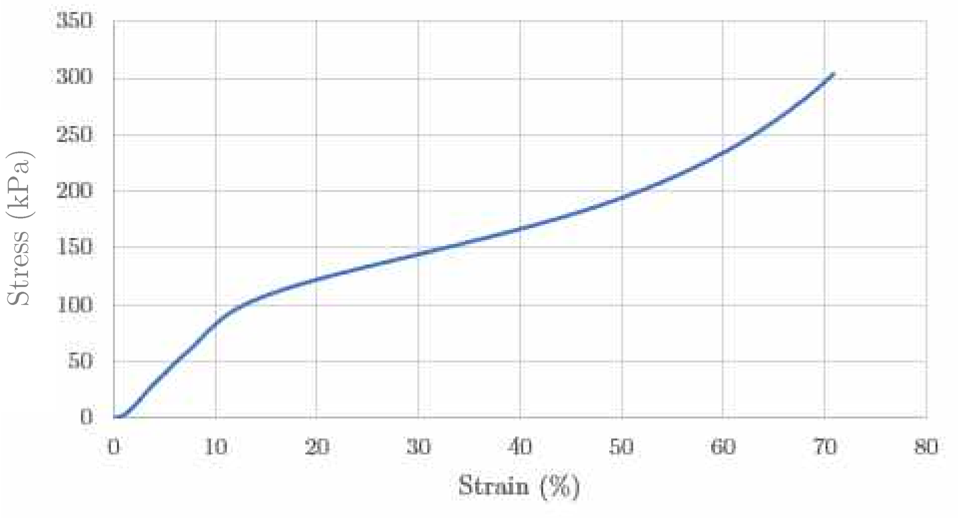

**Figure 3-30. Compression test stress-strain curve for the second test specimen.**

Using the same procedure to discretize the stress-strain curve, the literature stress-strain curve for the 20 kg/m$^3$ density was compared to the one obtained by means of the compression test, in Figure 3-31.

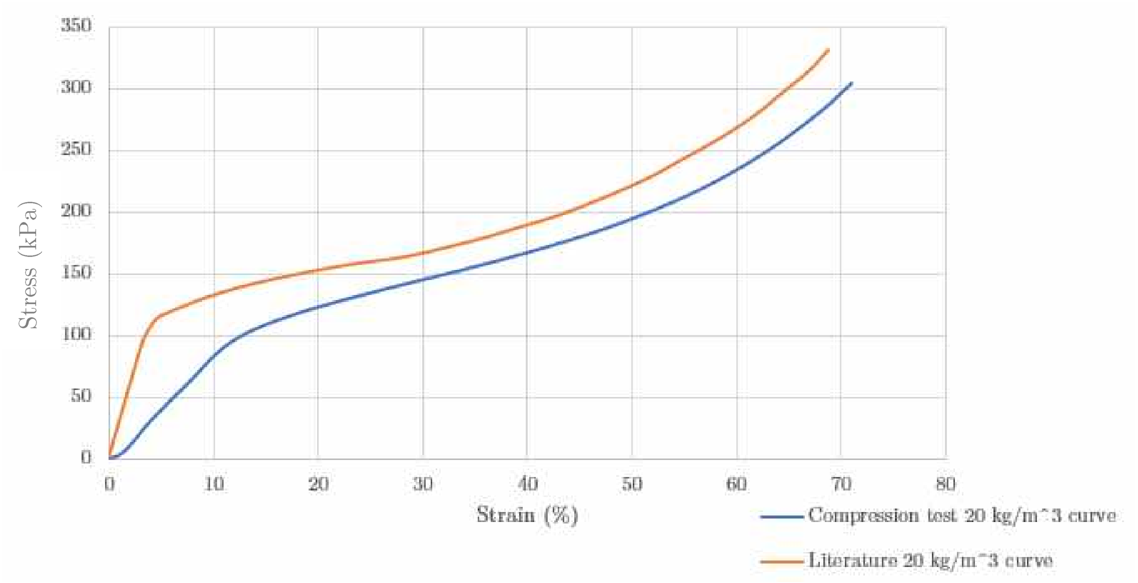

**Figure 3-31. Comparison between the Literature and Compression test curves for the second test specimen.**

It is verified that the behavior of each curve is similar, with just a difference in the stress values for each given level of strain, and in the progress of the linear elastic region mentioned before. The reason for the difference in the stress values for a given level of strain has been referred before and is due to the fact that both tests were not conducted with the same compression rate, since it is not known the compression velocity with which tests were made to obtain the first curve. The difference in the progress of the linear elastic region is due to what was explained before regarding the elastic return being larger than expected, since there is no collapse of foam cells in the transition plane between both foam samples constituting the test specimen, modifying the global elastic behavior.

The third test sample was also extracted from the lateral cushioning (with density equal to 27.5 $\mathrm{kg/m^3}$). Its dimensions were measured before the compression test as 59 by 54 mm for the upper and lower surfaces, with a height of 39.5 mm. As expressed for the first two analyzed samples, the punch movement will maintain a constant compression velocity of 0.5 mm/s, compressing 80% of the sample's thickness, which presents the value of 31.6 mm. The strain rate at which this sample was compressed was calculated as 0.01266/s. After compression, the third sample is retrieved from the servo-hydraulic machine and the final dimensions are measured (depicted in Figure 3-32).

**Figure 3-32. Third test specimen after compression.**

The final dimensions were measured as 59 by 54 mm for the superior and inferior cushion surfaces, and a value of 19.5 mm for the final height of the sample when the upper punch was reset to its original position. As also observed for the first two tests, there is no lateral elongation and, therefore, the conclusion on the Poisson's ratio being zero was once again corroborated. The elastic recovery was, as in the first examination, up to 50% of the height's initial length as it would be expected for any homogeneous sample tested.

In Figure 3-33, the stress-strain curve for this given compression rate obtained from the force-position curve extracted from the data recording equipment, is observed. Only the stress points up to an elongation corresponding to 70% of deformation in height were considered, since the curve of the literature with which this one will be compared was obtained for these strain values as well.

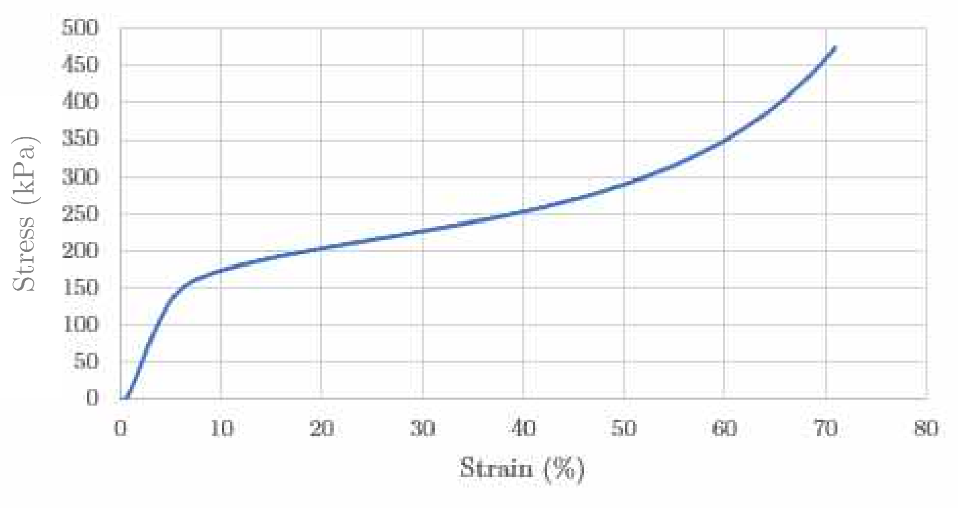

**Figure 3-33. Compression test stress-strain curve for the third test specimen.**

As the literature stress-strain curve for 30 $\text{kg/m}^3$ density value was already discretized for the previous comparison with the first sample's stress-strain curve, this was further used for possible comparison with the curve obtained in the compression test performed on this third and final sample analyzed (Figure 3-34).

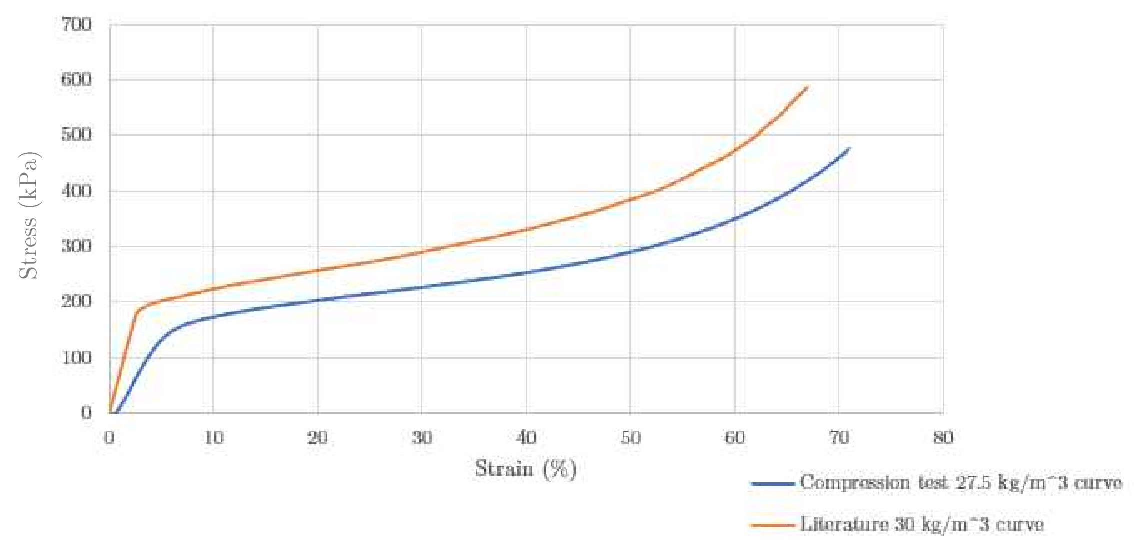

**Figure 3-34. Comparison between the Literature and Compression test curves for the third test specimen.**

Comparing both literature and compression test curves, it is noticeable that both curves' progress is, as far as possible, fairly similar. Yet again, the difference between the two motions results from the difference between the densities of the materials tested in each curve, and the possible difference in terms of the strain rate used in the conduction of each one of the analyses. It is possible to conclude with these three tests that both the 20 and 30 kg/m$^3$ curves supplied by Electrolux present themselves as excellent representations of the packaging assembly material's behavior.

### 3.3.5.1. Numerical Compression Test Simulation

In addition to these tests, a numerical compression test simulation was performed in the *LS-DYNA* software to demonstrate that the material card *MAT_CRUSHABLE_FOAM, used in the behavior modeling of the various cushioning modules, actually reproduces a similar performance to that observed in the literature curve for the foam with density of 30 kg/m$^3$, which has been proven to correctly represent the behavior of the physical foam material. To do so, a numerical construction was conducted using as reference the geometry of the third sample used in the compression tests, as seen in Figure 3-35. A *Shell*-type section was also defined, with rigid material and dimensions slightly larger than those observed on the surface of the sample to be simulated, to deliver constant compression to the upper face of the deformable body. Using the same unit system of the current model, a constant velocity of 0.5 mm/ms was imposed on the rigid section through the keyword card *BOUNDARY_PRESCRIBED_MOTION_RIGID.

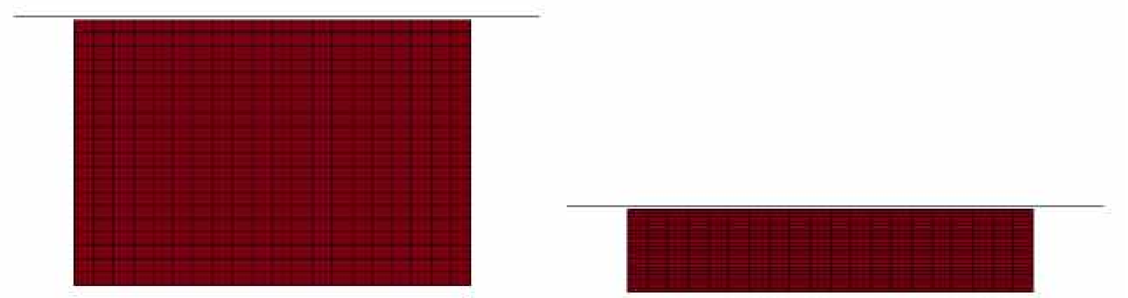

**Figure 3-35. Compression test's numerical representation.**

To define this card, it is only needed to choose the applicable degree-of-freedom for the velocity that is going to be imposed (z-translational degree-of-freedom) within the DOF parameter, and the indication that a constant speed will be applied, from the VAD parameter. Finally, a curve is defined to describe the velocity value through time, which will be represented by a horizontal line with the constant value of 0.5 mm/ms, through the amount of time needed to generate 70% of compression on the foam body. Equation 3.5 represents the time needed to achieve this volume of compression.

$$v = \frac{d}{t} \Leftrightarrow t = \frac{d}{v} \tag{3.5}$$

Where $d$ represents 70% of the third sample's height length (as its height takes a value of 39.5 mm), and $v$ the constant velocity rate.

In order to fix the sample's position during the entire simulation, the card *BOUNDARY_SPC_SET was employed, activating all translational and rotational constraints about each degree of freedom, inhibiting the movement of the nodes referring to the lower face of the object under study. Apart from this, only the contacts and the rest of the required commands for the operation of the simulation, have been defined.

The only contact card used was the *AUTOMATIC_NODES_TO_SURFACE, as it is very suitable for the situation in which the master side is a rigid body, since in this type of contacts only the slave nodes are analyzed for penetration by the master segments. In this way, it is prevented an increased simulation time regarding the verification of penetration of the slave segments in the master nodes, since the only deformable body is that which represents the foam sample. All of these definitions will be explained in full detail in the next section, regarding the "Definition of Contacts".

The last commands required for the finite element simulation process were the simulation termination control (*CONTROL_TERMINATION), the time-step control (*CONTROL_TIMESTEP), and finally those relative to which outputs will be written during the entire operation, including the time at which they will have to be written (*DATABASE_BINARY_D3PLOT and *DATABASE_ASCII_option). The crucial output to take from this simulation is the

RCFORC file, which provides the resulting forces on each contact interface present in the simulation. In this way, it is possible to know the force required by the punch, represented by the rigid *shell* section, to compress the test specimen with constant speed over the simulation time. Then again, these definitions will all be posteriorly detailed in a later section regarding the “General Final Simulation Controls”.

After the end of the simulation, the graph that represents the force at the interface between the punch and the sample over the time necessary to induce a deformation of 70% in height, is presented in Figure 3-36.

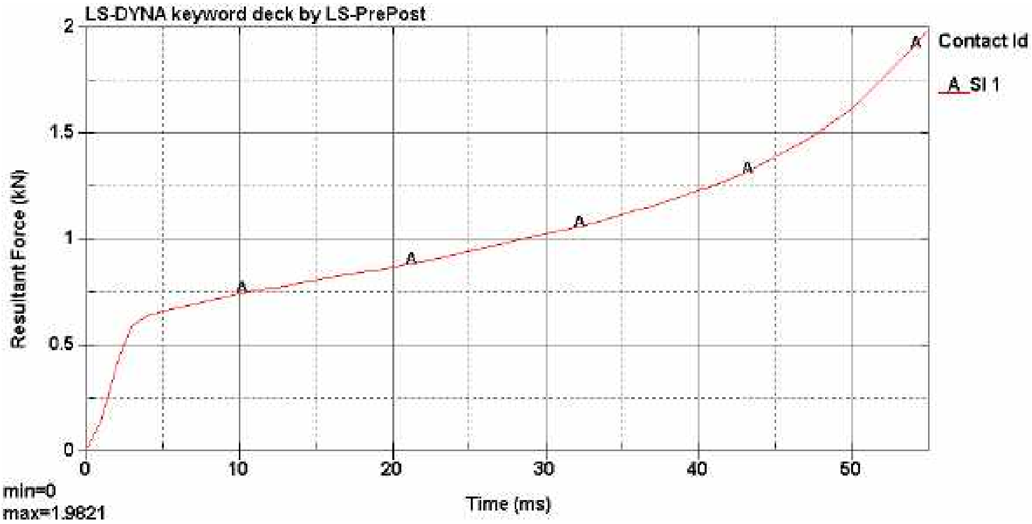

**Figure 3-36. Force-time graph plotted by *LS-DYNA*.**

Since the graph only indicates strength over time, it does not represent a good comparison point with the graph with which one wishes to compare. For this reason, the various coordinates of the graph were imported into *Excel* and the stress was obtained by dividing each force value by the resistant cross section which, as previously seen, does not change since the Poisson’s ratio remains zero. As the punching speed is constant, the deformation rate will also remain constant. Knowing this, it is possible to know the level of strain at each moment of the simulation.

Having now axes equivalence for the simulation and literature graphs, their comparison can be consulted in Figure 3-37.

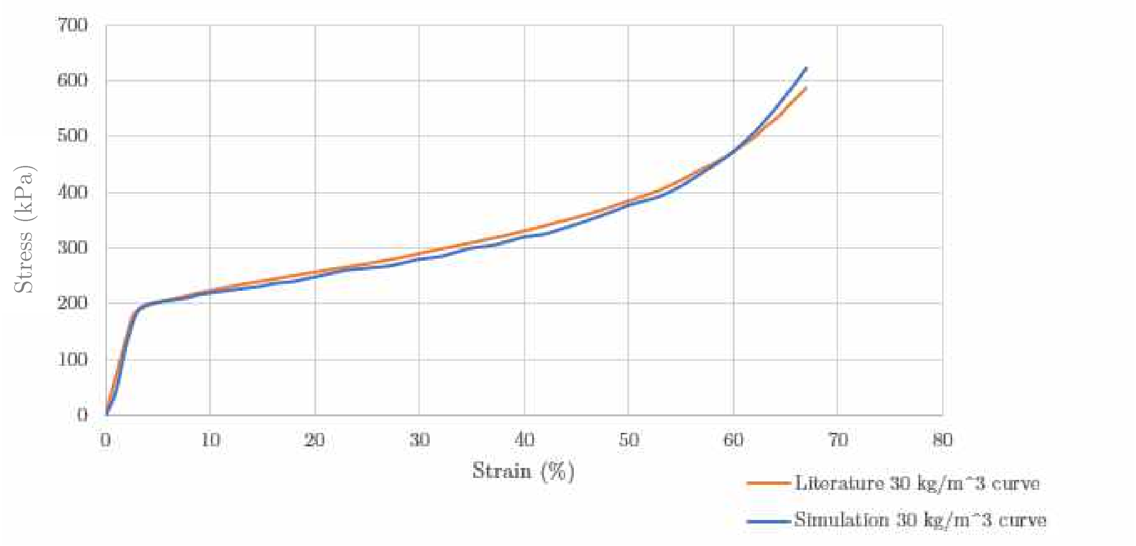

**Figure 3-37. Comparison between the Literature and Simulation test curves for the third test specimen.**

It is concluded that the material model *MAT_CRUSHABLE_FOAM, with the parameters mentioned earlier, represents in a dignified way the profile of the EPS foam given the graphics coincide to practically 100%.

## 3.4. Definition of Contacts

In a finite element software, the definition of contacts is of utmost importance to prevent interpenetration between parts, elements or nodes, which will come into contact with each other during the finite element simulation. This analysis is carried out using one of the *LS-DYNA's* own algorithms, made at each time step. These contacts are based on linear springs that can be found between the slave nodes and the nearest master segments, where the stiffness of these springs defines the applied force in the nodes of each.

The algorithms that define these contacts are divided into two different groups, *penalty-based* contacts and *constrained-based* contacts, where the former can be used in both rigid and deformable bodies while the latter will only be applicable to deformable bodies. The default method for analyzing interpenetrations is the *penalty-based* approach, which basically returns a force proportional do the depth of the potential penetration found, in order to withstand this interference, as in Equation 3.6 (LS-DYNA Support, 2001c).

$$F = l.k \tag{3.6}$$

Where $l$ is the creeping length, $k$ is spring's stiffness and $F$ the proportional force that eliminates the penetration.

### 3.4.1. Penalty-based Approach

As mentioned previously, the default computational method for the calculation of the contact spring stiffness is the *penalty-based* approach, which is described by the definition of SOFT=0 in the Optional Card A in each contact series. This concept uses the size of each contact segment and the respective material properties to determine the contact force value. These type of approach is not recommended to analyze contacts between materials exhibiting large differences in material properties, since the calculated stiffness will be the minimum displayed between that of the slave and that of the master, which may lead to values that are too small when the material stiffness parameters between contacting surfaces are not of the same order of magnitude. With this information, this type of analysis cannot be used in the definition of contact between the EPS foam and the oven structure, since the foam has a very soft material compared to the metallic materials in which the furnace is produced (LS-DYNA Support, 2001a).

For a solid element, the prescribed contact stiffness is calculated as presented in Equation 3.7, detecting the penetrations of nodes into segments and applying the appropriate force to both the penetrating node and the nodes of the segment (Livermore Software Technology Corporation (LSTC), 2018a).

$$k = \frac{\propto . K . A^2}{V} \tag{3.7}$$

Where $\propto$ represents the penalty scale factor, $K$ characterizes the material bulk modulus, A stands for the segment area, and finally, V represents the element volume.

For shell elements, Equation 3.8 is given for the stiffness calculation:

$$k = \frac{\propto . K . A}{Max\ (shell\ diagonal)} \tag{3.8}$$

In the wide variety of existing contact types utilizing the penalty-based formulation, the ones used to in the definition of contacts between the components pertaining to the oven's numerical model were the *CONTACT_AUTOMATIC_NODES_TO_SURFACE and the *CONTACT_AUTOMATIC_SURFACE_TO_SURFACE. The difference between these types of contacts is that the first one permits only one-way treatment of contacts, and the latter permits the treatment of contacts in both ways. This means that one-way contacts only check for penetration of the slave nodes specified by the software user into the surface selected master segments. Two-way contacts essentially work the same way as the correspondent one-way treatments, but also including the second application of the subroutines used to check the penetration of the slave nodes in the master segments, but this time using them to check the penetration of the master nodes in the selected slave segments (LS-DYNA Support, 2001b). The schematization presented in Figure 3-38, represents perfectly what happens in the definition of one-way contacts.

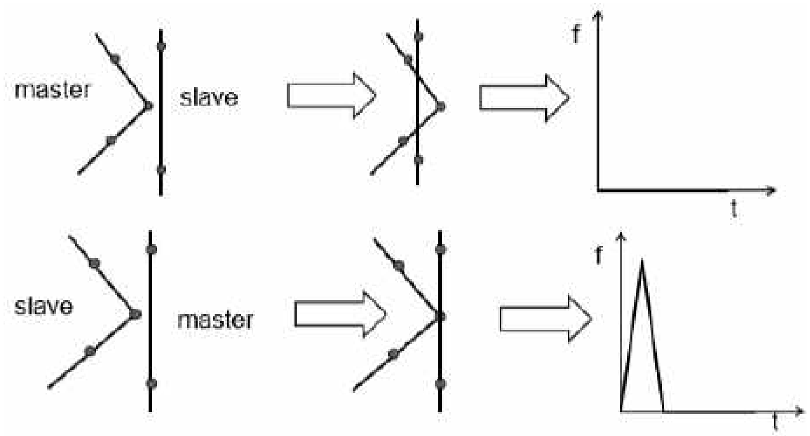

**Figure 3-38. Schematization of one-way contacts. Source: (Livermore Software Technology Corporation (LSTC), 2018a)**

For impact simulations, since the numerical model suffers great deformations due to the high kinetic energy felt at the moment of impact, it is extremely difficult to predict the orientation of components in relation to those found at its margins. Because of this, the contact type *CONTACT_AUTOMATIC_SURFACE_TO_SURFACE is recommended, since it searches for penetration on both sides of Shell type elements, projecting the contact surfaces in both directions from the normal direction of the middle plane of the element(LS-DYNA Support, 2001b).

To define this type of contact, two part ID's were chosen for contact verification, and the friction coefficients were assigned according to those that can be observed between metals, which make up the majority of the components present in the numerical model. Then, the selected values for the static and dynamic friction coefficients are taken to be 0.5 and 0.3 respectively for each contact characterization.

Although it is observed that two-way treatment contact types are more suitable for simulations containing crash analysis, these carry some disadvantages in comparison with one-way treatment contact types. In a simulation with thousands of nodes and elements present, combined with a vast number of components, the number of defined contacts also becomes considerable. As surface to surface contacts contain a more advanced algorithm, the analysis is not only more realistic but also more time consuming as the computational cost is proportionally increased in terms of simulation speed and memory utilization. This was the reason why the use of the contact type *CONTACT_AUTOMATIC_NODES_TO_SURFACE was chosen whenever its application was observed to be advantageous. There is, therefore, a decreased computational cost of approximately a factor of two due to not having to call each subroutine twice (LS-DYNA Support, 2001b).

### 3.4.2. Soft Constraint-based Approach

This contact stiffness calculation method, unlike the previous one, is independent from the component's material properties and consequently, highly appropriate for the treatment of contacts between very disparate materials. For the definition SOFT=1 in Optional Card A, the calculation is performed based on the nodal masses that come into contact and the global time-step size, creating the stability of a spring mass system, as shown in Equation 3.9.

$$k = 0.5 \cdot SOFSCL \cdot \frac{m}{\Delta t_0^2} \tag{3.9}$$

The SOFSCL parameter, only applicable for SOFT=1, is a special stiffness scale factor that may be defined in this command's card.

The use of the *Soft Constrained Penalty Formulation* (SOFT=1) is justified when the contact of dissimilar materials is desired, such as the situation present in this work in the establishment of a contact between the various EPS foams and the oven. As mentioned in the "Negative Volume in Soft Materials" section, the keyword card *CONTACT_AUTOMATIC_NODES_TO_SURFACE was recommended and used with the formulation SOFT=1, to define this contact. In these circumstances, using this soft formulation will ensure an interface contact stiffness once or twice as great as the one that would arise when using a penalty-based formulation (LS-DYNA Support, 2001a). These numerical problems are explained by the fact that the cushioning and the overall oven structure differ greatly in terms of modulus of elasticity and bulk modulus, causing unrealistic numerical results between these components. This option can also be used in situations where the degree of refinement of the meshes that are brought into contact are very dissimilar.

The *Segment-based Penalty Formulation* (SOFT=2) provides a stiffness calculation of the linear contact springs quite similar to that observed in the SOFT=1 option. This formulation invokes a segment-based contact algorithm, rather than the usual node to segment penetration checking, where penetration is found between two different segments and a penalty force is exerted on the nodes of both segments. The contact forces are consequently distributed more realistically, which makes this treatment a safeguard for situations where the first two formulations fail to function. The only inconvenience encountered is, as can be reasonably expected, the fact that it cannot be used in nodes-to-surface contact types, since not only segments are generated. The contact stiffness calculation is then given by Equation 3.10.

$$k = 0.5 \cdot SLSFAC \cdot \begin{Bmatrix} SFS \\ or \\ SFM \end{Bmatrix} \cdot \left(\frac{m_1 \cdot m_2}{m_1 + m_2}\right) \cdot \left(\frac{1}{\Delta t_0}\right)^2 \tag{3.10}$$

Where the SLSFAC, SFS, and SFM all represent different scale factors, being 0.1 the recommend value for the first parameter, and the value of 1 advisable for the latter.

This segment-based formulation proved to be very effective in the contact definition between the bottom foam and the floor and between the lateral and bottom foams as well, which were modelled using the contact card *AUTOMATIC_SURFACE_TO_SURFACE.

### 3.4.3. Connection Contacts

The *Contact* controls can also be used to connect components. With the help of this control, a number of connections have been defined in the numerical model in order to faithfully represent the structural interconnection behavior between the oven assembly components.

Since the number of components modeled with *Solid* type elements is quite limited, the link between components modeled with this type of element and components modeled with *Shell* type elements is minimal. The only components modeled with Solid elements are the packaging assembly units (bottom, side, and cardboard), one of the three glasses located in the door assembly, and lastly, the transformer. Of all these components, the only one that is directly connected to the oven structure is the transformer, while the others are only in simple contact with the structure. This observation is relevant, since the *Solid* elements (ELFORM=1) of which the transformer is composed, do not have rotational degrees of freedom, unlike the *Shell* elements that make up most of the components of the numerical model, so the connection between these different types of elements has to be carefully managed. Their connection would, therefore, require special commands to maintain the rotational continuity of degrees of freedom between the elements, but instead, the connection will be made by means of a special technique where connection contacts are not involved, which will be explained in detail in the next section.

For the connection between components modeled with *Shell* elements only, the contact commands *TIED_NODES_TO_SURFACE and *TIED_SURFACE_TO_SURFACE were employed. The application of this type of contacts is only possible if the components meshes are considered close enough to one another, based on the software's criteria. When this is verified, the slave nodes are transferred to the master surface and its isoparametric position is controlled by kinematic constraint equations.

The contact command *TIED_SURFACE_TO_SURFACE was the least used with only eight applications in the whole model. This contact card was mainly used to connect components where the entire contact surface between the two components was intended to be bonded. A good example to illustrate this point is the connection required between the three parts that constitute the cavity, as can be observed in Figure 3-39.

**Figure 3-39. Connection between the middle and the remaining Cavity parts.**

The remaining tied contact used, the *TIED_NODES_TO_SURFACE contact card, was employed in the connection of components at specific locations within their surface, in this case, where the heads of the screws used for the connection of the actual structure would be found. Even this type of contact was not widely used, with only fifteen implementations, since the distance between many of the components was not sufficiently small to meet the program's analysis criterion for tied contacts.

Most of the implementations of this contact card were within the cavity connections, as for example in the connection of the Cavity to the Fan Protection or the Mica sheet, seen in Figures 3-40 and 3-41, respectively.

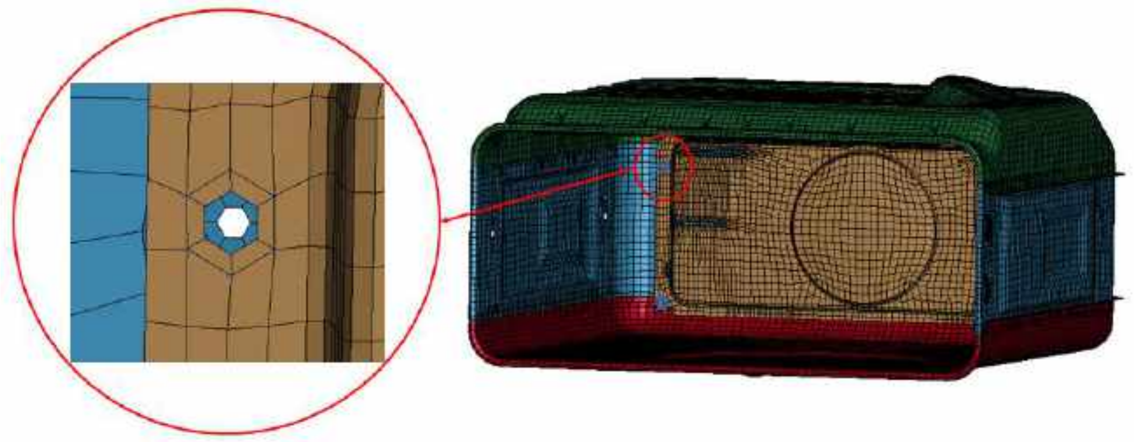

**Figure 3-40. Connection between the Cavity and the Fan Protection.**

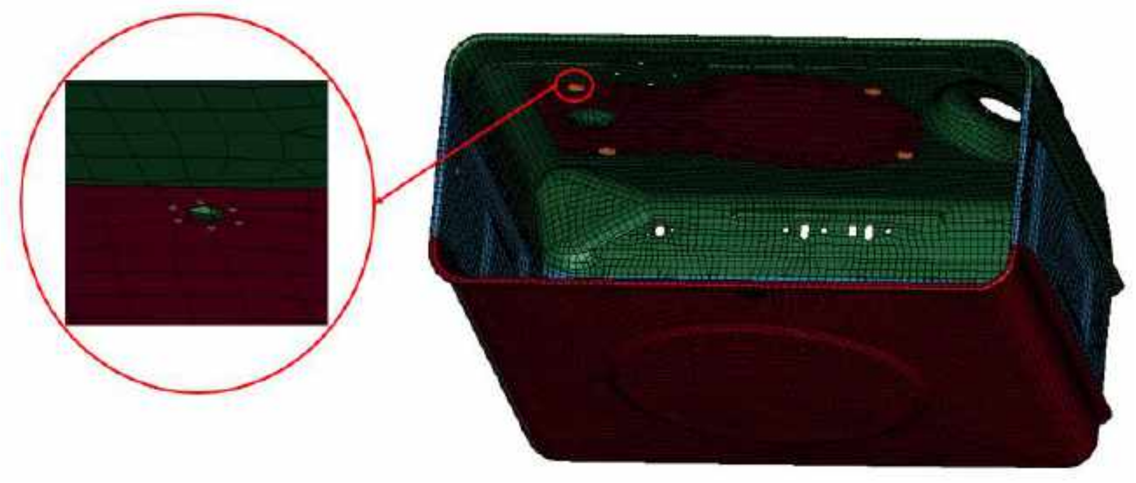

**Figure 3-41. Connection between the Cavity and the Mica sheet.**

To define this contact card, as observed in both Figure 3-40 and 3-41, the nodes from the Fan Protection and Mica sheet where the screw head would settle were chosen to be the slave nodes, and the cavity part was defined as the master surface to which the selected nodes would be held fixed to. The only noticeable difference with regard to the definition of the first tied contact card, was that in this one two part ID's were used to define the slave and master segment since it was desired to connect the entire contact surface between components.

Although all these connections worked perfectly, both these contact types should, however, be used in *Shell* type elements very carefully since the rotational degrees of freedom of the slave nodes are not constrained by these specific tied contacts. That was the reason why they were seldom used, and the rest of the screwed connections were performed using a special technique explained in detail in the following section.

## 3.5. Modelling of Rigid Connections

For the modelling of the remaining screws that were not included in the tied contacts, it was used a conventional technique where the bolt shank is represented by a rigid *Beam* element with Hughes-Liu with cross section integration formulation (ELFORM=1) and modelled with *MAT_RIGID, being the connection between this and the screw hole achieved by means of a *spider mesh* (Sonnenschein, 2008). The *spider mesh* is also made up of rigid *Beam* elements, with the exact same formulation as the element that represents the bolt shank, which have to be strong enough to provide a powerful connection and that have the aim of representing the screw head and the nut by being connected to each node of the screw hole. This technique is quite common, as it enables a considerable reduction in the computational cost associated to the modeling of the screws, since their modeling is rather trivial, and avoids the need of establishing contacts between the bolt shank and the screw hole and between the screw head and the external areas of the components that are being connected. It is important to emphasize that this is not by any means the best option to estimate and evaluate the bolt loads, but this is not the focus of the computational model analysis and with this type of modeling it is only intended to achieve a successful connection between the components involved.

This type of connection not only restricts the movement of components in all degrees of freedom to which they are subjected, but also lowers the computational time associated with the analysis of tied contacts also used initially. It thus becomes a highly recommended technique for this type of applications. The graphic representation of a *spider connection* can be visualized in Figure 3-42, and its modeling is achieved in a few steps, as it will be described below.

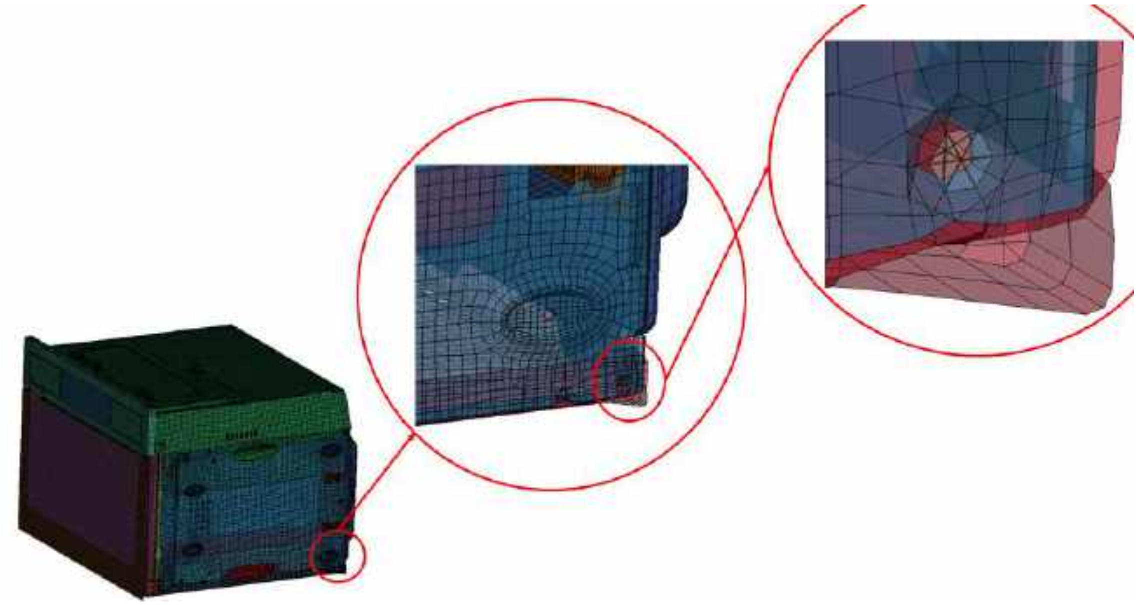

**Figure 3-42.** ***Spider connection*** **between the Side panels and the Housing Bottom.**

To model a *spider connection*, one should start by creating a center node in the middle of the screw hole of both components intended to be linked. The next step should be the linkage between each node of the screw hole to the center node recently created, by means of rigid *Beam* elements. The final step is to create the bolt shank, which means connecting the center nodes belonging to each screw hole.

## 3.6. Technique for the Replacement of Components

A major problem regarding the construction of a finite element model with an accompanying large scale of elements is the long simulation time that hinders the speed at which results are delivered and ultimately the validation of the model, necessary for its application in its designated role. Thus, if there are components whose structural composition does not require any analysis in the specific purpose of the simulation to be performed, it contributes greatly to the success of the simulation if these are removed or, if their weight has an influence on the deformations of other components, are modeled in different ways that allow a considerable reduction in the final number of elements.

One of the ways to obtain this result is by adding mass elements with the mass of the components to be replaced and by using the *CONSTRAINED_NODAL_RIGID_BODY command to connect each of them to the surface area to which they would be in contact with if they had actually been modeled. The lumped mass added by defining the mass element, is assigned to a nodal point located at the position of the center of mass of the component intended to substitute, with the value of its mass. In order to make these elements load other components congruently, their weight must be distributed in accordance with their position in the actual oven structure. This is where the command *CONSTRAINED_NODAL_RIGID_BODY comes to play, computing the inertia tensor from the nodal masses and creating a sort of rigid body with its surface area composed by the nodes of the component to which it is connected, and constituting the exact same geometry as the physical component to be relieved. With this command, the equations of rigid body dynamics allow the update of the movement of the nodes and consequently account for their rotation (Livermore Software Technology Corporation (LSTC), 2018b).

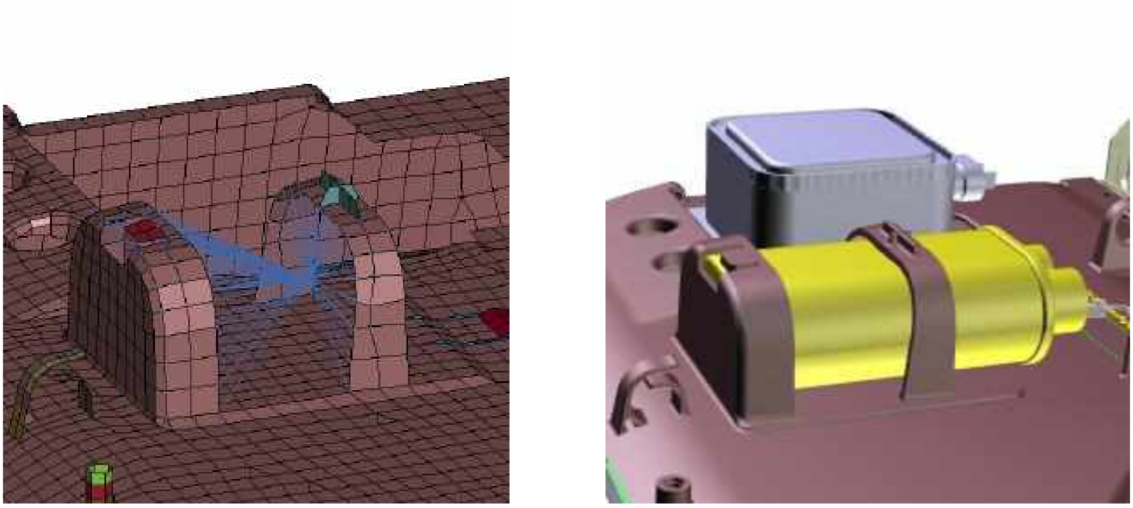

**Figure 3-43. a) Capacitor nodal rigid body representation. b) Capacitor representation In the geometric model.**

To define this command, it is only required to create a node set where the first node represents the node located in the center of mass of the rigid body to be created, and the remaining nodes represent the surface of the physical component projected on the surface of the component to which it is attached. For a better understanding of the explanation provided, the visual representation of this function applied to the construction of the capacitor rigid body can be found in Figure 3-43 a). In Figure 3-43 b), it is possible to observe the capacitor representation in the geometric model, which would be connected to the cooling channel at the entire area relating to the tabs designed to incorporate this component. It is also visible in Figure 3-43 a) that all nodes are connected to one common point, which is the mass element located at the center of mass of the capacitor.

The whole set of components that were included in the numerical model by this method, is composed of the aforementioned capacitor, the electronics board, the magnetron, the cooling fan, the interlock, the circuit board vision, the hot air motor, and the mass that was still to be provided to the model so that it would reflect the real mass of the physical model. The nodal rigid bodies can be observed in Figure 3-44 a), whereas the same components represented in the geometric model can be previewed in Figure 3-44 b).

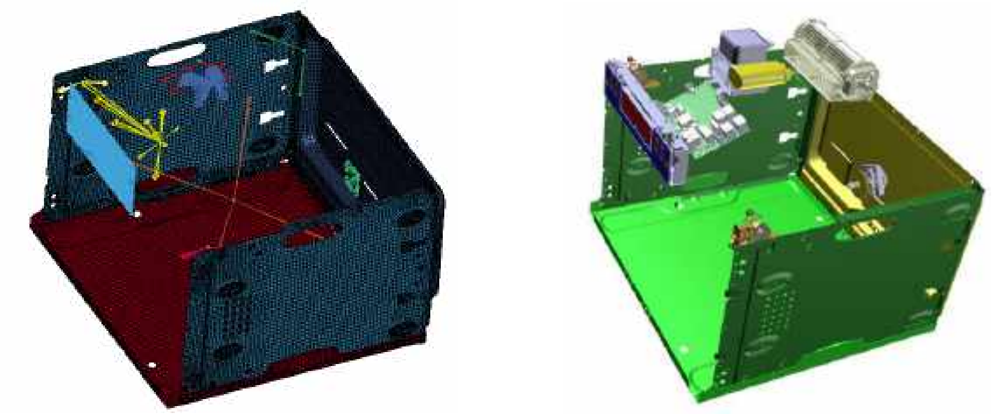

**Figure 3-44. a)Totality of nodal rigid bodies present in the numerical model. b) Components substituted by nodal rigid bodies, in the geometric model.**

## 3.7. Vibration Test for Connection Verification

In order to verify whether the connections established either with the tied contact definition or with the *spider connection* were successfully obtained, a vibration mode test was conducted during the construction of the oven assembly. In addition to the verification of the success of connections between components, this eigenvalue analysis also permits the verification of the authenticity of detected contacts and the verification of interpenetrations between components when excited in certain vibration modes.

To perform this analysis only a few controls need to be used, these being the *CONTROL_IMPLICIT_EIGENVALUE, the *CONTROL_IMPLICIT_GENERAL and the *CONTROL_TERMINATION. Through the *CONTROL_IMPLICIT_EIGENVALUE command the number of mode shapes to be analyzed can be defined. For the purpose of this simulation, 100 different vibration modes were requested in order to cover the vibration modes of various components (in addition to those belonging to the complete oven), in order to control a large amount of the defined contacts and ascertain that there would be no interpenetration in the remaining ones as well. In *CONTROL_IMPLICIT_GENERAL command, the implicit method must also be activated by setting IMFLAG=1 to perform this vibration analysis. To conclude, it is always necessary to set a termination time using the *CONTROL_TERMINATION control.

The output of the simulation is shown in Figure 3-45, and displays each mode shape of the oven and the correspondent frequency at which this mode occurs. If every component is connected correctly, then the oven will move all together in the first six modes observed in the simulation, which refer to the six degrees of freedom where the oven can translate and rotate. If the contacts are also properly established, there will be no penetration during the translation or rotation movements of the oven.

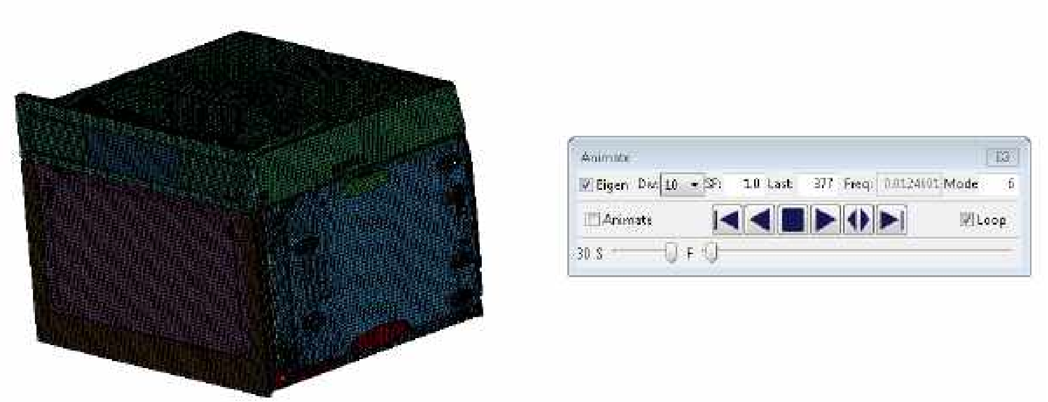

☑ Eigen Div: 10 SF: 1.0 Last 377 Freq: 0.0124101 Mode 6

☐ Animate ☑ Loop

**Figure 3-45. Vibration modes analysis output in *LS-DYNA*.**

## 3.8. Definition of Boundary Conditions

In the data sheet provided and used by Electrolux for testing and validation of finished products (EHP/EUROPE, 2004), it is required for drop examinations of appliances with more than 20 kg that the whole product-packaging assembly is released from a height of 250 mm, as shown in Table 3-7. The five drops required, are one onto the assembly's base, and another four on each of the four bottom edges where the product carries an angle of 10º between the its base and the horizontal.

**Table 3-7. Drop test release height depending on the appliance's weight.**

| Appliance's weight | Drop Height | Number of drops |
|---|---|---|
| **<10 kg** | 800 mm | 6 |
| **>10 <20 kg** | 600 mm | 6 |
| **>20 kg** | 250 mm | 5 |

To simplify the numerical simulation and once again, in order to reduce the simulation time, the simulation is set up positioning the oven at a distance of 0.1 mm from the floor. To define this peculiarity, it is necessary to define an initial velocity that would correspond to the velocity obtained by the oven when falling from the aforesaid height of 250 mm. The initial velocity may be defined by the command *INITIAL_VELOCITY and its value can be obtained from the equations of motion of a body in freefall, presented in Equations 3.11 and 3.12.

$$v_z = v_{0z} - g.t \tag{3.11}$$

$$z = z_0 + v_{0z}.t - \frac{1}{2}.g.t^2 \tag{3.12}$$

Since the oven is dropped from a pre-determined height, the correspondent initial velocity at the moment of being dropped is 0, so $v_{0y}$ is taken to be null. Knowing this, the time it takes for the assembly to fall from 250 to 0.1 mm can be extracted by using the quadratic formula in Equation 3.12. The time is thus expressed in Equation 3.13:

$$t = \frac{\pm\sqrt{2.g.(z_0 - z)}}{-g} \tag{3.13}$$

Substituting the time in the equation concerning the instantaneous velocity, it is obtained in Equation 3.14 the value referring to the velocity at 0.1 mm of elevation. The representation of this simplification is also available in Figure 3-46.

$$v_{y=0.1mm} = -\sqrt{2.g.(z_0 - z)} \tag{3.14}$$

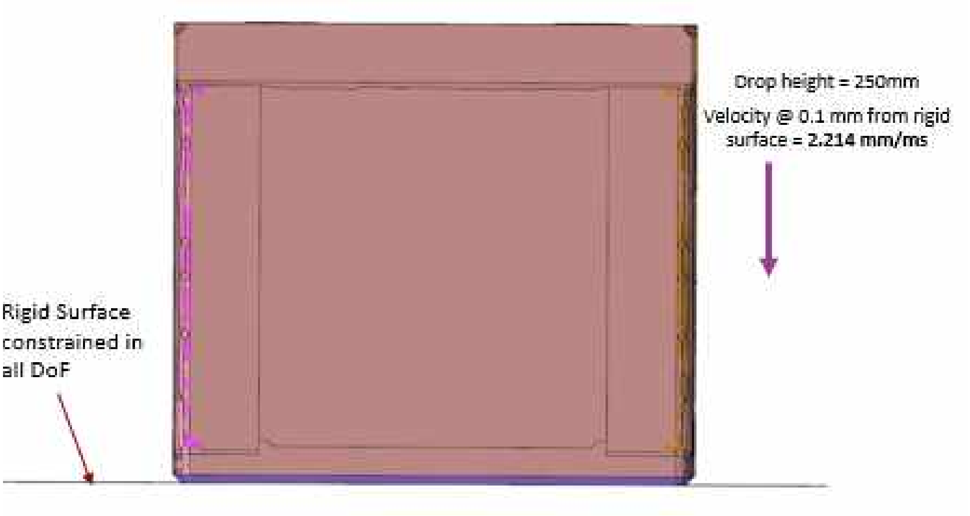

**Figure 3-46. Drop test specifications for software implementation. Source: Electrolux**

Although the initial velocity is set, there is still the acceleration of gravity applied to the oven, which can be set using the *LOAD_BODY_Z and the *LOAD_BODY_PARTS function. The first one, is used to define body force loads due to a prescribed base acceleration in the z-axis direction, which is taken to be the direction of fall. These body force loads are held constant to simulate gravitational loads defined by the command *DEFINE_CURVE, where the gravitational acceleration through time is established (Figure 3-47). The second *LOAD command is finally used to specify the part subset subjected to the acceleration specified (which will be all the assembly, except for the floor).

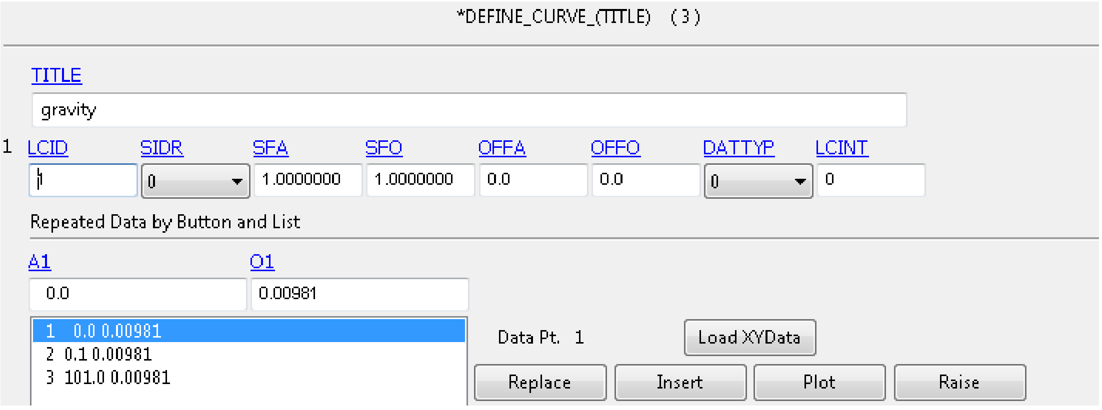
*DEFINE_CURVE_(TITLE) (3)

TITLE: gravity

| | LCID | SIDR | SFA | SFO | OFFA | OFFO | DATTYP | LCINT |
|---|---|---|---|---|---|---|---|---|
| 1 | 1 | 0 | 1.0000000 | 1.0000000 | 0.0 | 0.0 | 0 | 0 |

Repeated Data by Button and List

| A1 | O1 |
|---|---|
| 0.0 | 0.00981 |

1 0.0 0.00981
2 0.1 0.00981
3 101.0 0.00981

Data Pt. 1

**Figure 3-47. Acceleration value over the simulation time.**

In Figure 3-47 it is also possible to observe that gravity is defined in three distinct points. Being 0.00981 mm/ms^2 the value of the acceleration of gravity in the previously specified units, this one is then defined in the moment of t=0 s, which represents the moment of the beginning of the simulation. The second point of t=0.1ms only intends to facilitate the analysis and to indicate the *software* that after a short period of time, the observed acceleration remains the same. Finally, the point of t=101ms is chosen as the instant after the end of the simulation time, once again to facilitate the analysis of the acceleration in the program at the final simulation instance. As no simulation exceeded the time of t=100ms, this point was preserved for any of the simulations performed.

It is also necessary to restrict the movement of translation and rotation of the ground in all global directions. Since the floor is defined with rigid material, this type of restriction is imposed in the material definition itself by setting the CON1 and CON2 to 7.

## 3.9. General Final Simulation Controls

To make the simulation run, it is necessary to apply some final controls to establish the simulation period, the time gap between analyses performed by the software, and determine which outputs the program must record to be analyzed posteriorly in the post-processor.

The command needed to determine the amount of time to be analyzed during the simulation is called *CONTROL_TERMINATION, where it is only necessary to define the simulation termination time. In addition, it is also possible to control the end of the simulation by observing an increase in mass percentage that exceeds a threshold established in this command. Although this parameter is of great relevance, it will be explained in more detail in the following section where the phenomenon "Mass Scaling" will be described.

The time interval in which the simulation is analyzed, called time-step size, can be controlled using the *CONTROL_TIMESTEP card. Using this control, a time-step scale factor can be established, which should be less than or equal to 90% of the time-step calculated by *LS-DYNA*, in order to prevent instabilities. Of course, in order to reduce the actual simulation time to a minimum, it is necessary to choose the largest possible time-step size that will present itself under stable conditions, and for this matter the largest time-step scale factor of 0.9 was assigned to this variable. The time-step used for each iteration is given by Equation 3.15.

$$\Delta t^{n+1} = TSSFAC * \min\{\Delta t_1, \Delta t_2, \ldots, \Delta t_N\} \tag{3.15}$$

In this equation, TSSFAC represents the time-step scale factor parameter, and N is total number of elements. Thus, during the simulation the system loops through all elements and determines the new time-step size for each evaluation by finding the minimum value over all elements (Livermore Software Technology Corporation (LSTC), 2018b).

The parameter DT2MS was also used in the *CONTROL_TIMESTEP command, but once again it refers to the phenomenon of “Mass Scaling” which is more conveniently discussed in the next section.

The last mandatory cards to be defined are those that define the outputs to be written by the software that will be analyzed in the post-processor. The *DATABASE_BINARY_D3PLOT requests binary outputs of geometry history and state variables, that are used in *LS-PrePost* to animate deformed geometries and plot time histories of component stresses and nodal displacements. It is, therefore, necessary to specify in this command the time interval between the achievement of output results. The last required control, which is the *DATABASE_ASCII_option, offers the possibility of selecting which type of files the user wants to retrieve from the simulation performed, and of how long the output from the file should be collected. The files chosen to be written were the GLSTAT file, the MATSUM file, the NODOUT file, the RBDOUT file, and the SLEOUT file.

The GLSTAT file offers global statistics on a lot of comprehensive information, such as the time-step, the added mass, the different types of energy existing in the system, external work, and global velocities. This file makes it possible to evaluate the size of each component of the overall total energy of the system, in order to understand if the energy balance of the system is in conformity with the established rules presented in Equation 3.16.

$$total\ energy = initial\ total\ energy + external\ work \tag{3.16}$$

The MATSUM file provides a clearer insight on the kinetic, internal, and hourglass energy, since these can be measured for each component/part of the system, in order to be evaluated and compared the energy state in each one of them. Apart from this, other outputs as momentums, rigid body velocities, and eroded energies for each part can be recovered.

The NODOUT file is quite crucial for the validation of this numerical model as it offers vital data on each node's displacement (/rotation), velocity (/rotational velocity), and acceleration (/rotational acceleration). This way, it is possible to compare the accelerations measured by accelerometers placed in specific places of the physical model, with the calculated acceleration at the node located on that corresponding position in the numerical model.

The RBDOUT file provides details on rigid body motion at different time cycles. This is of great relevance as it gives the nodal rigid bodies' coordinates, velocities, and accelerations, at different time cycles to track the center of mass movement of components which were modelled using mass elements and the *CONSTRAINED_NODAL_RIGID_BODY function.

The final file, labelled SLEOUT, reports a more detailed information about contact energies on each defined contact, in an effort to find the location of problems related to negative contact energies (if applicable).

The last piece of information to point out is the use of the *CONTROL_ENERGY card to request the inclusion of Hourglass, Stonewall, Sliding interface, and Damping energies in the ASCII files GLSTAT, MATSUM, and SLEOUT, to aid in the evaluation of the energy balance.

## 3.10. Mass Scaling

The Mass Scaling phenomenon refers to the process of adjusting an element's explicit timestep by simply adding non-physical mass to its structure. The objective of using this technique is to obtain an increased global time-step in order to reduce the simulation time that is conditioned by the critical time-step of the system, which in turn is limited by the Courant's stability criteria (Livermore Software Technology Corporation (LSTC), 2018b). To define the type of Mass Scaling performed during the simulation, the DT2MS parameter found in *CONTROL_TIMESTEP must be defined as either a positive or negative value.

When DT2MS is set to be a positive value, mass is added to those elements whose time-step is lower than |DT2MS|, and removes mass from those whose time-step is higher than this referred value. This ensures that the overall time-step is equal for every single element present in the analysis, but there is no identifiable advantage for using the method over the negative DT2MS method since it will take out mass from elements which wouldn't need this removal (as the critical time-step of the simulation is given by the lower time-step found) and possibly provide inaccurate deformations results because of the lack of mass in those places.

Setting the minimum time-step in DT2MS as negative value, the *software* will only add mass to those elements whose time-step is below the |DT2MS| threshold. Although this is a very convenient tool and procedure to take when the minimum time-step produces unbearable simulation times, it is also needed to ensure a proper care for the simulation to make sure the added mass is not too big and produce once again adverse effects on the simulation accuracy. What happens is if the percentage of mass is relatively large compared to the total mass existing in the numerical model, the components that have undergone this modification will lead to detrimental non-physical inertia effects that may dominate the global solution. For this matter, it is good practice to limit the added mass to a certain amount using the ENDMAS parameter in *CONTROL_TERMINATION. This value was chosen to be 2% to safeguard a minimum amount of added mass in the system. When this value is reached, the numerical simulation is concluded since the amount of added mass is becoming too large, so the DT2MS value must be carefully chosen to on one hand maintain a reasonable simulation time, and on the other to make sure that the added mass does not exceed the imposed limit and lead to an early termination of the simulation.

Given that mass scaling is not an easily estimated process, several iterations and attempts were performed in regard to the choice of the minimum time-step specified in DT2MS (Bala, 2006).

4

# Chapter 4 - Simulation Results and Discussion

This chapter presents the results achieved through numerical simulations carried out on the basis of the drop test procedures followed by Electrolux. The simulation was performed in order to determine and analyze the stresses present in the various components, deformations, displacements, and also accelerations for comparison with the experimental data acquired with the aid of two 1-axis direction accelerometers. To conduct the 60 ms simulations for assessing the critical structural components, approximately 176 hours of analysis time were required, using 1 CPU 8 core i7 of 4.20 GHz.

The structure for this chapter is divided in Energy Balance analysis, where it is explained what are the different energies present in the analysis and what would be the expected values for each , in order to understand if the simulation is providing good and consistent results energy-wise. The necessary controls used to ensure that each energy value was at its projected value are also detailed and clarified. Then, the acceleration curves obtained from the simulation for three specific components are compared with the ones found via experimental testing, to assess if the oven's response is similar in both situations. The final section was created to express the results of stress analysis for several components which were found to sustain critical loads during the drop test, reaching the plastic regime.

As the construction of the numerical model is an iteration process, quite a few attempts were performed to correct the problems that would arise from each modification implemented. Due to the amount of time necessary to carry each simulation it was not possible to correct the last problems encountered, regarding some unpredicted energy values and components behavior. On the other hand, these small problems were found not to influence the results validity, as they were very discrete and localized.

## 4.1. Energy Balance

In order to obtain reliable simulation results energy-wise, the various energy components accounted for by the *software* have to respect some rules that lead to a perfect energy balance. The total energy conveyed in the GLSTAT file is the sum of the internal, kinetic, contact, hourglass, system damping, and rigidwall energy. This total energy present in the system will exhibit a perfect energy balance if the sum of each of its constituent components is equal to the sum of the total initial energy of the system and the external work. In the GLSTAT file, this verification may be assessed observing if the energy ratio, which is given by the ratio between the total and initial energy of the system, is equal do 1, or in other words, if both curves display the same progression (LS-DYNA Support, 2002c). If the total energy is greater than the total initial energy, it means that energy is being artificially introduced, for example, due to numerical instabilities or due to the detection of artificial penetrations between contact surfaces. If, on the other hand, the total initial energy is greater than the current total energy of the system, energy is being artificially absorbed due to, for instance, over-compliant contact surfaces (LS-DYNA Support, 2002a). The energies associated with deleted elements (Eroded internal energy) and deleted nodes (Eroded kinetic energy) are also included in the sum of the total energy if elements are selected to be eroded. As the ENMASS parameter has been set to 1 in the keyword *CONTROL_CONTACT, the eroded nodes of the eroded solid elements remain active in the contact algorithm, and since only solid elements are eroded due to problems related to negative volumes in the bottom cushioning as a result of the material type to which it is associated, the eroded kinetic energy will be zero for this particular situation.

One last thing to keep in mind is the appearance of negative contact energies, which are expected to be positive. Through the SLEOUT file, contact energies for each contact are reported, so the investigation on where these negative energies are located is easier to be achieved.

By analyzing through the post-processor the final results of the energy ratio (Figure 4-1), it can be seen that the energy ratio is not fully in accordance with the statement mentioned, starting at 1 but rising in the course of the simulation until it reaches the value of 1.77. The cause found for this slight increase is the fact that some of the contacts defined in some door components present some difficulties that have visibly altered the loads and accuracy of the behavior of these same components.

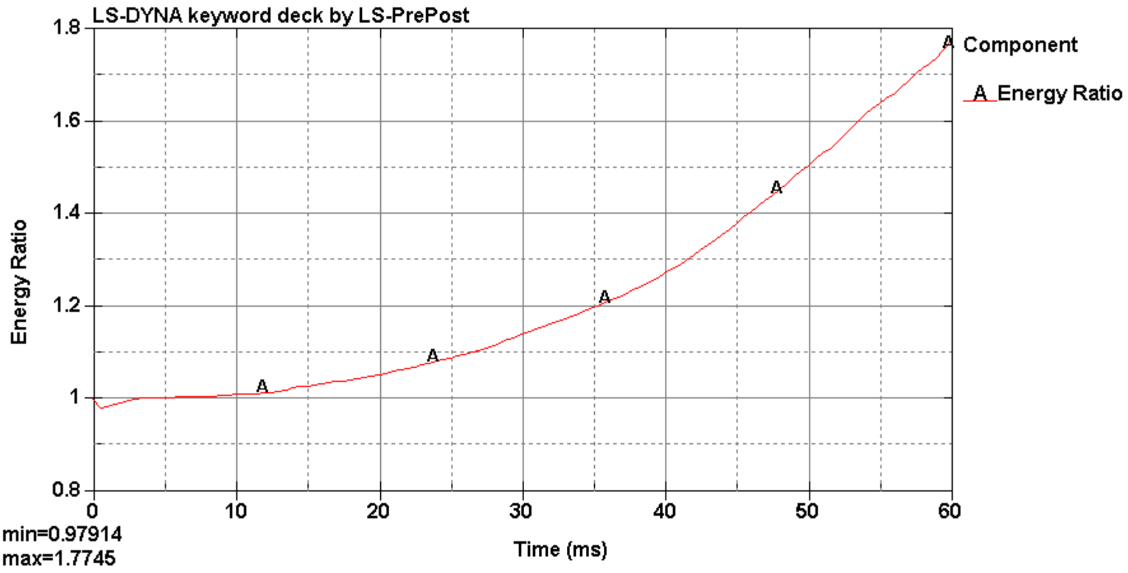

**Figure 4-1. Numerical model's Energy Ratio.**

With this in mind, it was also noted that the contact energy was not in line with the expected values and was found to be negative. It is known, though, that if the global internal energy progress is equal but opposite to the global contact energy curve found, it is likely that the problem is very localized and has relatively low impact on the overall validity of the numerical model's solution (LS-DYNA Support, 2002c). Observing Figure 4-2, one may see that the previous statement is verified and that the solution presents still great results in terms of energy balance, despite witnessing the negative contact energy which will not influence the global results.

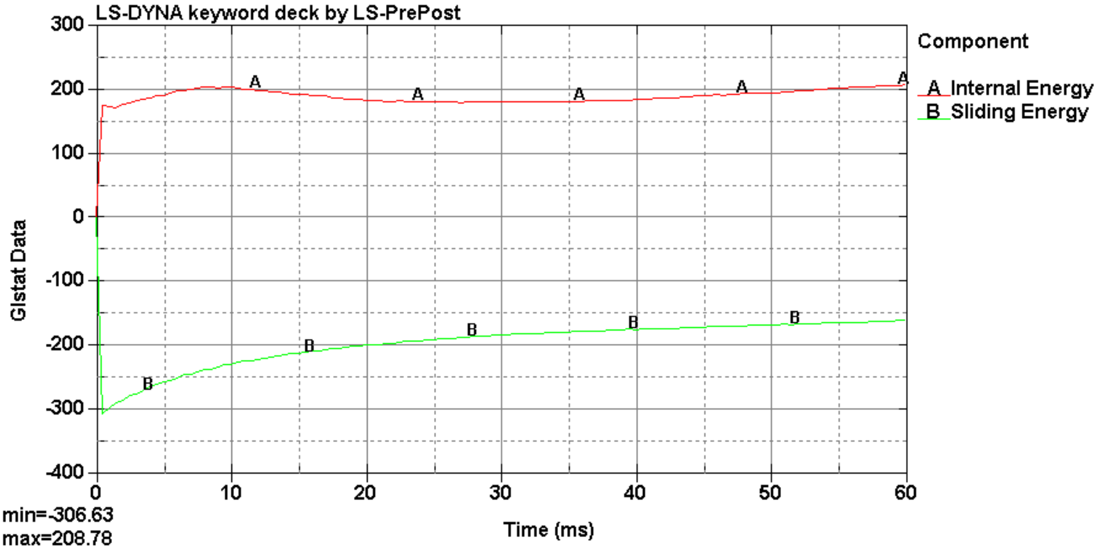

**Figure 4-2. Internal and Sliding energies' values over the simulation time.**

Searching through the SLEOUT file, the problem was found to be located on the *AUTOMATIC_NODES_TO_SURFACE contact number 174, defined between two of the Choke components. In Figure 4-3, it is possible to see the contact energy uttered by this contact, which is observed to almost match the global contact energy and leading to the conclusion that the main issue comes from the contact number 174. Both of the Choke components that are present in this contact, may be visualized in Figure 4-4.

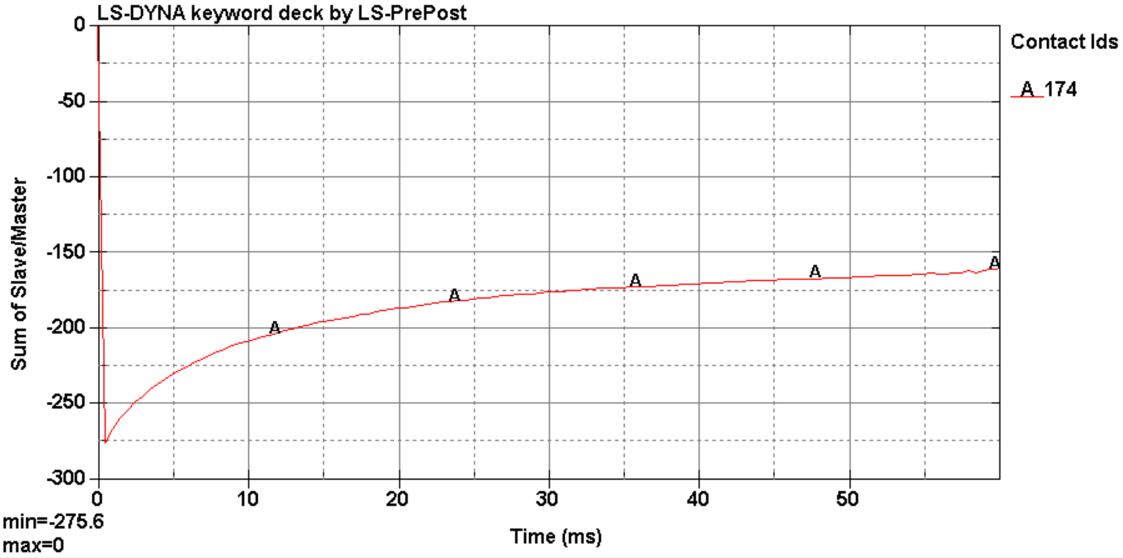

**Figure 4-3. Contact energy for the contact number 174.**

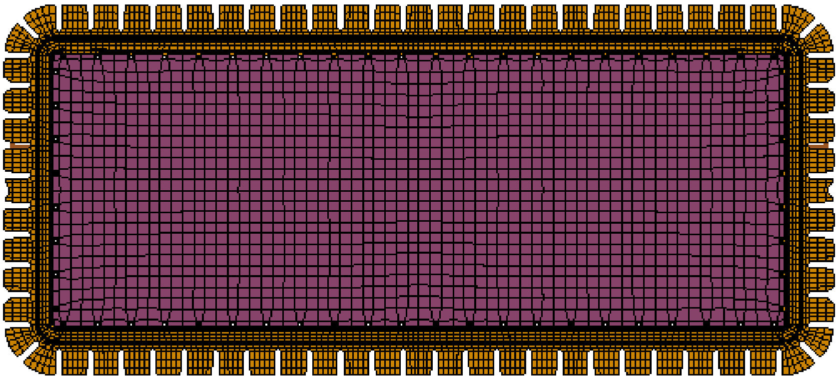

**Figure 4-4. Choke components present in contact number 174.**

At the point in time the numerical model was perfected and this last minor issue was found, although easily corrected, there was not enough time available to correct it as the simulation times would reach almost 8 days. Nevertheless, as already seen, it will not pose a major problem on the veracity of the results extracted from the simulation.

In order for the GLSTAT, MATSUM, and SLEOUT files to account for all the energies mentioned above, the keyword *CONTROL_ENERGY must have the parameters HGEN, RWEN, SLNTEN, and RYLEN set to 2. This way the Hourglass, Stonewall, Sliding interface, and Damping energies are computed and included in the energy balance, as it was already mentioned in the previous “General Final Simulation Controls” section.

### 4.1.1. Hourglass Energy

The major problem regarding the use of single-point integration elements, which are fully used in this finite element model owing to their low computational cost, is the fact that they introduce the appearance of zero-energy modes of deformation that produce both zero strain and stress, called Hourglassing modes. These modes are observed to be oscillatory and tend to have much shorter periods than those detected in the structural response, and for this motive, the outcome are mathematical states that are not physically possible (Hallquist, 2006). Although fully-integrated *Solid* and *Shell* elements don’t produce Hourglass modes, its use is not only quite more expensive (which is not desired in an explicit numerical simulation that already presents extremely high simulation time lengths) but also are less robust and relatively unstable in large deformation analyses (LS-DYNA Support, 2002b). The Hourglass energy, which is the work done by internal forces that provide resistance to Hourglassing modes, takes away physical energy from the system as Hourglass deformation modes are orthogonal to the strain calculations. However, Hourglass control is always recommended to resist these deformation modes that cause suspicious and unreliable results to the final deformations analyzed in the numerical model (Livermore Software Technology Corporation (LSTC), 2019a).

The internal forces calculated to resist Hourglass modes may be applied by choosing one of the several internal *LS-DYNA* control algorithms present in the *HOURGLASS keyword card. A general Hourglass control may also be applied in the entire model, using the *CONTROL_HOURGLASS card, which will add elastic stiffness to fight hourglass modes but not rigid body motions or linear deformation fields. This method is quite effective when Hourglassing occurs due to small displacements situations, which is achieved by increasing the QH parameter (Hourglass coefficient) carefully. If this parameter exceeds the value of 0.15, instabilities may arise due to over-stiffening the model's response in large deformation applications.

Using the aforementioned *HOURGLASS card, the model's stiffness may be locally increased in specific constituent parts. The adoption of this method allows the resistance to Hourglass deformations in areas intensively affected by these modes, without the excessive increase of the overall stiffness of the model. The control types used in this keyword can be identified as being of stiffness or viscous nature, depending on whether the Hourglass forces generated are proportional to the components of the nodal displacements contributing to the occurrence of Hourglass modes, or proportional to the components of the nodal velocities that also contribute to these modes. The stiffness control types are able to successfully reduce total accumulated Hourglassing deformations and is highly convenient for crash and impact simulations (as the aim of this numerical model). The viscous control forms, on the other hand, are more suited for high velocity and strain rate simulations (Livermore Software Technology Corporation (LSTC), 2019a). Instead of using these controls, there is always the possibility of refining localized meshes where Hourglass deformations are found (which would increase once again the simulation time), or even avoiding point and edge loads or contacts, but a wise use of the previously mentioned controls is always preferable.

The oven's numerical model presented quite some challenges regarding Hourglass problems. As a general guideline, the Hourglass energy for each numerical component should be less than 10% of the internal energy of that same component. If this is verified, the hourglass energy of the entire system will certainly also show values below 10% in comparison with the global internal energy. Almost every single component displayed problems regarding high Hourglass energy, so for this matter, three different types of Hourglass control formulations showed relatively good results when it came to reducing the adverse effects brought by these modes.

As aforementioned, stiffness control forms are desirable for crash and impact analysis and, as many authors advocate, control types 4 (*Flanagan-Belytschko stiffness form*) and 5 (*Flanagan-Belytschko stiffness form with exact volume integration for solid elements*) chosen for IHQ in *HOURGLASS card are recommended when it comes to controlling the Hourglass for metal and plastic parts in crash simulations, which comprise all the constituent components of the oven, except for the cushion assembly (Bala & Day, 2013). For foam materials, control type 6 (*Belytschko-Bindeman [1993] assumed strain corotational stiffness form for 2D and 3D solid elements only*) is recommended. However, since the cushioning components are modelled with tetrahedral elements, no problems related to hourglass will occur.

For the most part, control type 4 was used with the Hourglass coefficient set to 0.1, as it displayed formidable results for the major part of the components. Hourglass control type 5 was only used for the component "cavity middle" with the Hourglass coefficient also set to 0.1, as in more advanced iterations it has shown to respond better to this type of formulation. The only two components that have demonstrated the need for different Hourglass control to be used were the "transformer" and the "cardboard", modelled with ELFORM=1 solid elements, which showed no significant decrease in Hourglass energy when subjected to Hourglass control type 4 or 5. Therefore, the Hourglass control type 6 was employed, which invokes an assumed-strain corotational stiffness formulation for ELFORM=1 solid elements, and when used with a Hourglass coefficient set to 1, provides excellent accuracy on decreasing Hourglass energy for elastic material modelled parts (Livermore Software Technology Corporation (LSTC), 2019a)

(Livermore Software Technology Corporation (LSTC), 2018b). To finish, it was observed in advanced iterations of the simulation that the Bottom Cavity, the Bottom Element Protection, and one segment of the Spacer were displaying negative Hourglass energy values, which is certainly not desired. For this matter, the element formulation for the three (all three are modelled with *Shell* elements) was changed to ELFORM=16, which is the recommended fully integrated formulation for *Shell* element modelled numerical parts. As detailed, although fully integrated *Shell* elements are more expensive in terms of computational effort, they definitely do not Hourglass, thus the problem was resolved.

In Figure 4-5, it is possible to see that the global hourglass energy presents values way below the peak of the global internal energy of the system during the whole simulation. This was also verified for every single component in the MATSUM file, but the various graphs won't be presented as their number is quite extensive.

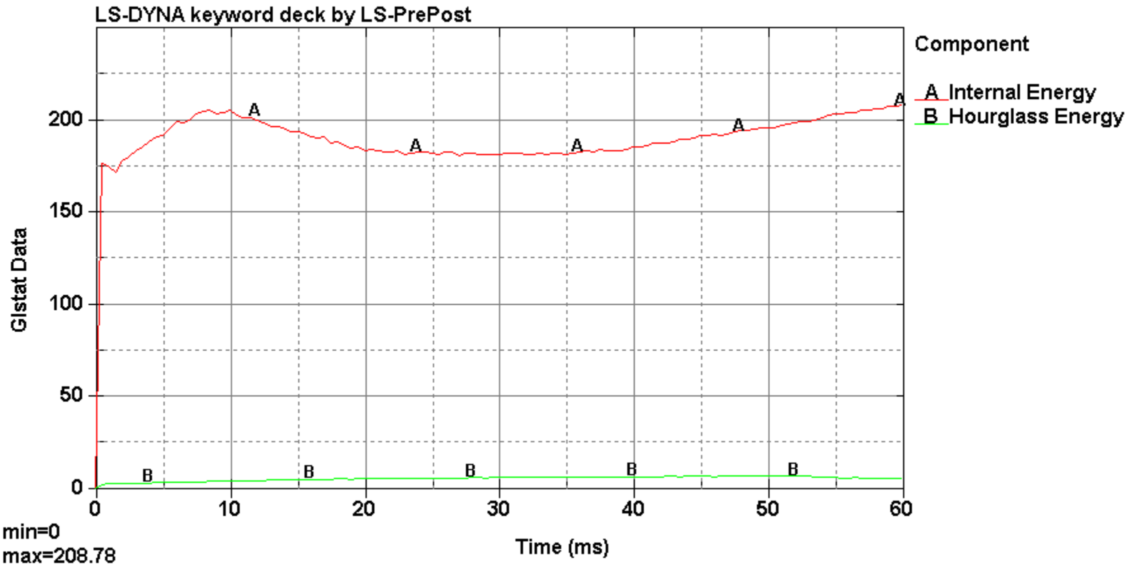

**Figure 4-5. Variation of the Internal and Hourglass energies over the simulation time.**

## 4.2. Acceleration Curve Comparison

To validate the finite element numerical model created, the method it was decided to follow was to compare the acceleration curve progress for two specific components via numerical simulation with the curves obtained by Electrolux via experimental drop testing on the oven model. The experimental testing was conducted using two different one-axis accelerometers, being one placed on the Magnetron and the other on the Hot Air Motor, respectively.

### 4.2.1. Magnetron's Acceleration Curves

The experimental setup for the Magnetron's accelerometer may be observed in Figure 4-6, where different views and the dimensions for correct positioning of the accelerometer can be visualized.

Knowing where the accelerometer was introduced, the next step would be to find the right nodal point in the numerical model on essentially the same position as the one found in Figure 4-6, to guarantee the closest curve progress when compared to the experimental one. The problem faced when selecting the mentioned nodal point, was that the Magnetron's component was not modelled but instead was replaced with a mass element at its center of mass to replicate its inertial contribution on the rest of the model. With this matter, there is no nodal point defined on the exact same position as the one where the accelerometer was placed in the physical model.

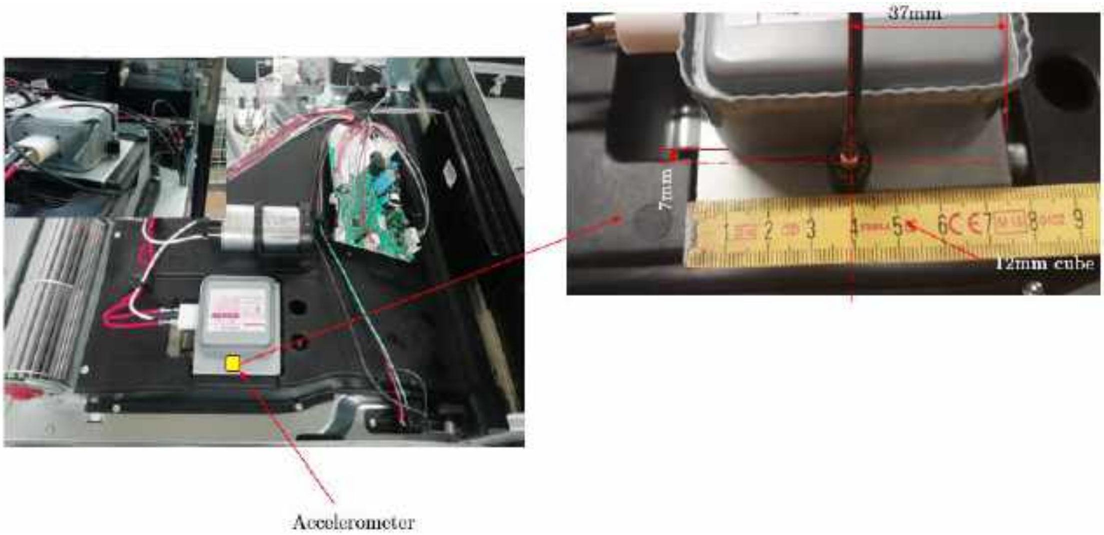

**Figure 4-6. Correct positioning of the accelerometer on the Magnetron's physical component. Source: Electrolux**

The nodal point chosen to follow the acceleration progress, found in Figure 4-7, is then the one representing the Magnetron's center of mass since this is the closest node to the right location, and presents virtually the same motion as the point where the accelerometer should be located. It is, however, possible that differences between the acceleration curves appear due to the rotation of the oven and oscillation of different components that directly affect the motion of both points (center of mass and accelerometer position) of the Magnetron.

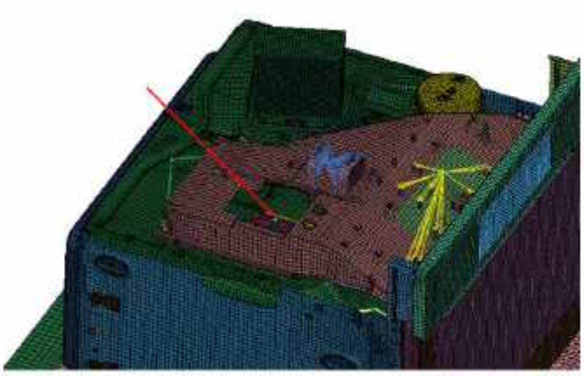

**Figure 4-7. Magnetron's mass element representation and location.**

As the experimental acceleration curve for the Magnetron is already accessible (since it was provided by Electrolux), the simulation curve is extracted from *LS-PrePost* by assessing the information on the NODOUT ASCII file. Thus, the node number 996819 (Magnetron's mass element) presents the acceleration curve on the Z-axis (height) found in Figure 4-8.

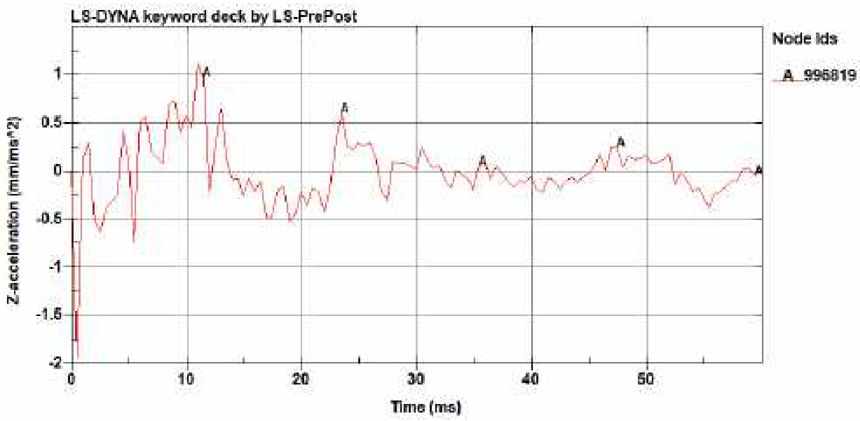

**Figure 4-8. Acceleration curve for the node number 996819.**

Using the same filter applied by Electrolux on the traces acquired (Butterworth @300Hz 4th order) and comparing both the experimental and numerical curves on the same graph, one may see in Figure 4-9 that both progressions display good correlation and are considerably identical, making the numerical Magnetron's virtual motion behavior a virtuous agreement of the measured motion.

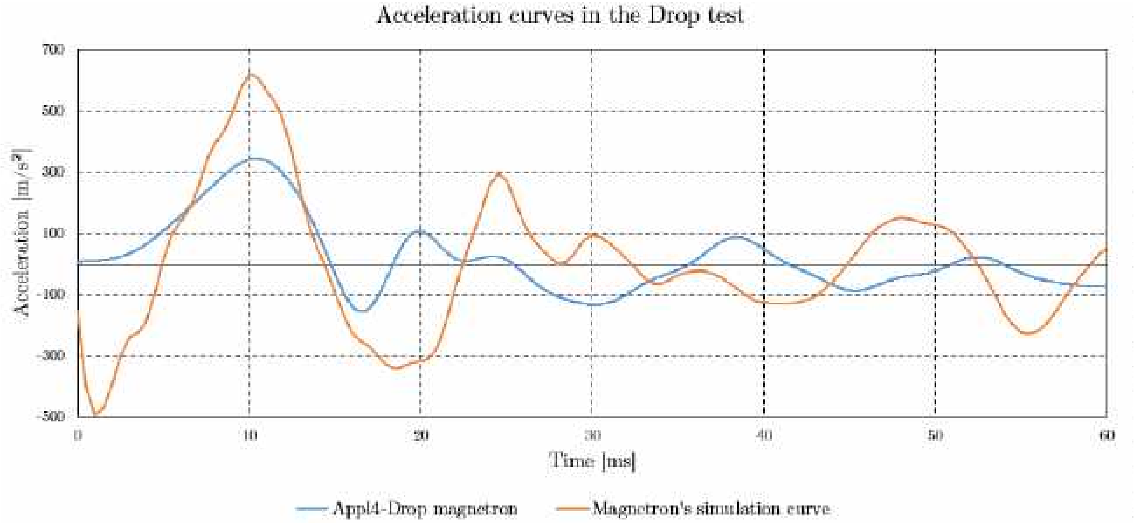

**Figure 4-9. Magnetron's acceleration curves comparison.**

It is important to observe that although the nodal point chosen to compare the accelerations was not positioned on the exact right location, it does not seem to make that much of a difference on the results obtained for this specific component. This implies that the physical Magnetron component displays what is called a rigid body motion. Also, the experimental accelerometer will rotate according to the movement of the components to which it is attached, which will result in the software's global vertical axis not always being fully aligned with the vertical axis of the accelerometer. It would be expected, then, that the curves would not entirely match, but as observed, an agreement between the numerical and experimental qualifications was obtained.

### 4.2.2. Hot Air Motor's Acceleration Curves

The experimental setup for the Hot Air Motor's accelerometer can be seen in Figure 4-10, where different views and the dimensions for correct positioning of the accelerometer can be visualized.

The Hot Air Motor presents the same problem observed with the Magnetron, as this component was also modelled as a nodal rigid body, using a mass element at its center of mass and the *CONSTRAINED_NODAL_RIGID_BODY control to induce its inertial contribution to the parts to which it is directly connected.

**Figure 4-10. Correct positioning of the accelerometer on the Hot Air Motor's physical component. Source: Electrolux**

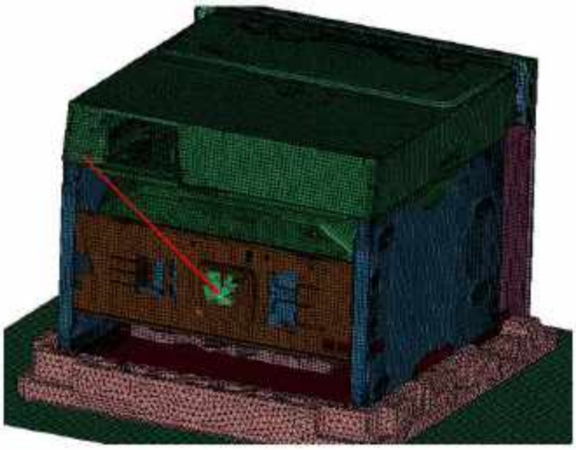

**Figure 4-11. Hot Air Motor's mass element representation and location.**

As this problem is posed, once again the nodal point chosen to assess the acceleration curve progress (see Figure 4-11) is the one representing the Hot Air Motor's center of mass since it is the closest node to the right location, and presents practically the same motion as the point where the accelerometer should be positioned.

Comparing again both the experimental and numerical curves on the same graph (using the same filter mentioned earlier), one may see in Figure 4-12 that both progressions display nearly the same movement and are substantially identical with even similar values revealed.

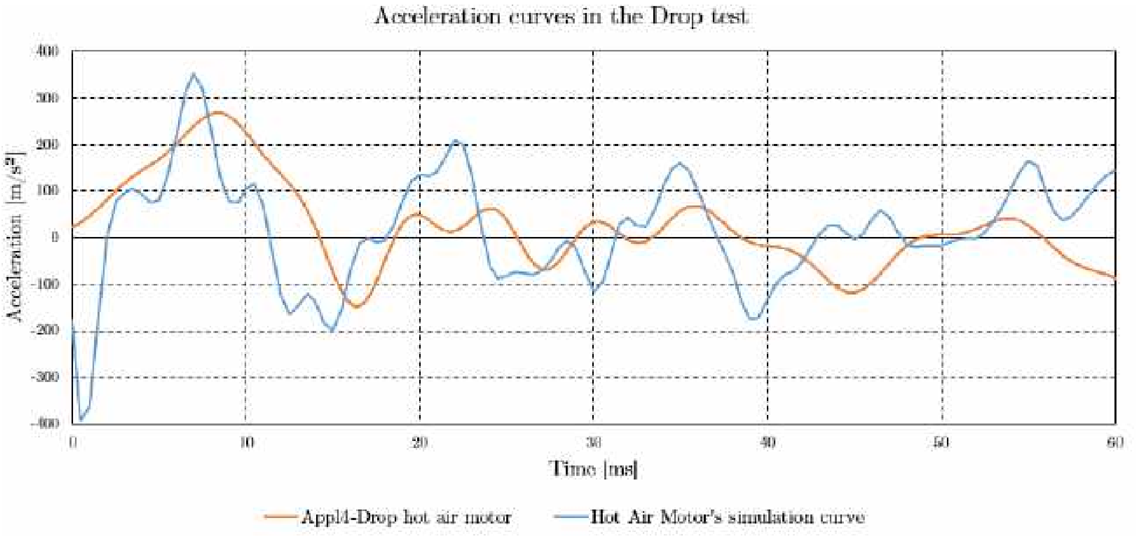

**Figure 4-12. Hot Air Motor's acceleration curves comparison.**

The simulation curve for the Hot Air Motor does not display an equally smoother progress as the respective experimental curve, even with the filter applied, but it is noticeable nevertheless that the progress is very similar in both situations and displays the same oscillations throughout almost the entire simulation, except at the final moments. As larger simulations were not conducted, it is not possible to see if the simulation curve would stabilize in the same manner as observed in the experimental route, but since both curves match during almost the entire time, it is accepted as a successful and virtuous approximation.

As mentioned before, small differences may appear due to possible rotations of the oven that lead to the axes' misalignment and different motions between the point being analyzed in the physical model and the Hot Air Motor's center of mass. The final thing that should be kept in mind, is that the simulation was performed with only elastic material models.

It is possible to finally assume and conclude that the numerical model is validated and presents a good kinematic correlation with the experimental drop test performed on the physical model. In this way, it is possible to ascertain that the state of stresses analyzed in the next section is in agreement with the physical state of stresses, and more easily the damages in the oven can be detected. In this next section, it will also be found if some structural elements reach plasticity regime stress values, and if this occurs, it poses one more influential issue on each of the simulation acceleration curves' progress.

## 4.3. Stress Analysis

The efforts present in several critical components of the oven that present high loads will be examined to understand where and why these fall into plastic regime during the course of the simulation. In order to perform this analysis, the Von Mises yield criterion was chosen in the assessment of the stress distribution along each component. In addition to the components in critical stress states, some of the components that help the understanding of the overall behavior of the oven are also highlighted, in order to understand how it evolves over time and if there are any fluctuations due to the weight distribution inside, as well.

### 4.3.1. Cavity Stress Analysis

Starting initially by observing the components of the Cavity Assemble, the first component in which high-stress levels were observed (above its yield strength) was in the Cavity itself, in its upper left-hand lateral zone, as it can be observed in Figure 4-13. The stress values range from 0 (blue) to 180 (red) MPa which is the yield strength value for the Cavity's material, as previously seen in Table 3-4 of the "Characteristics of the Employed Materials" section in the preceding chapter. For values above 180 MPa, the elements will display red color independently of their stress values.

This stress distribution was obtained from instant t=10ms in which the most critical period was observed in this component. There are two elements highlighted in Figure 4-13, which were randomly chosen from the most critical section observed in the Cavity, in order to prove that it was at the referenced time instant that the highest values of stress were observed. These elements, which are *Shell* elements S65979 and S65984, have the stress values to which they are subjected over the simulation time represented in the graph of Figure 4-14.

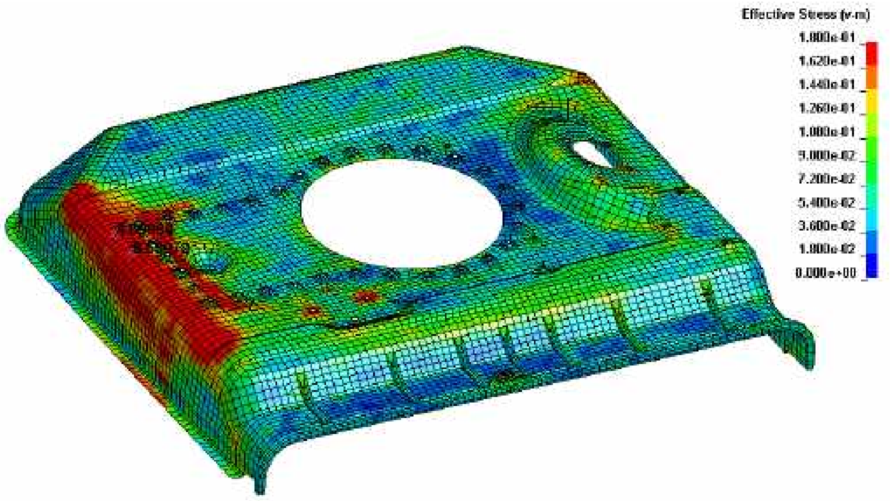

**Figure 4-13. Von-mises stress analysis of the Cavity (GPa) at t=10ms.**

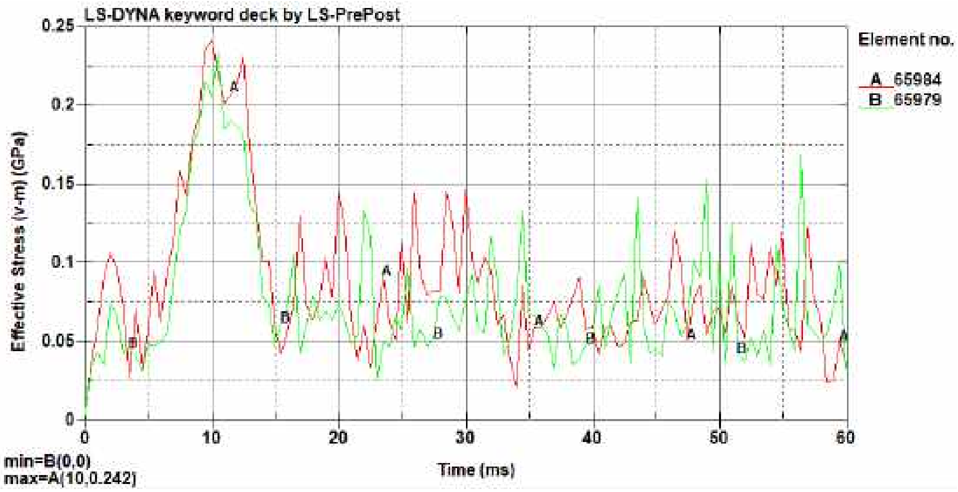

**Figure 4-14. Von-mises stress values for the elements 65984 and 65979.**

As can be seen, the highest stress values in both elements appear between t=9.5ms to t=10.5ms, but more specifically in t=10ms where maximum global stress of 242 MPa is observed. In the neighborhood of this instant, the yield stress value is not exceeded for the remaining simulation time.

The reason why this region has such a high-stress value is due to the fact that there is a mass element (representing the Magnetron) directly above this area, connected to the "Bracket Magnetron" component. Due to the inertia achieved by this mass element, a large distributed force is transferred directly from the Bracket to the "Cover, Waveguide", and from the latter to the Cavity to which it is attached. The inertia is at its maximum between t=9ms and t=10ms, as it is at this moment that the greatest compression in the bottom cushion, which is absorbing the impact of the structure, is presented. Since the oven no longer penetrates the cushion, a force contrary to the weight of the magnetron is performed in the Cavity, causing the stress to reach the maximum value at this point in time.

The confirmation for this statement can be secured by analyzing the displacements of the bottom cushioning's elements, represented in Figure 4-15. By selecting several elements on the periphery of the base of the cushion (where the biggest deformations will happen since this is the place where the furnace structure's supports are placed), the nodes' displacement through the simulation time may be assessed in the graph of Figure 4-16.

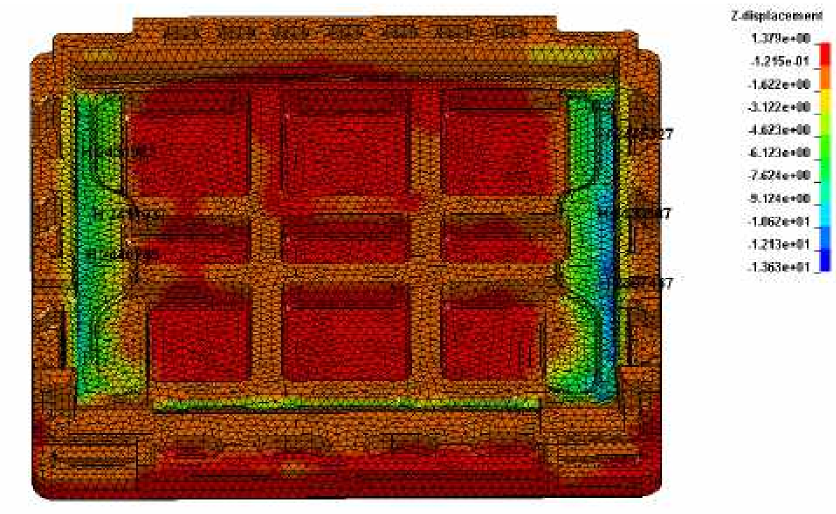

**Figure 4-15. Z-displacement (height) analysis for the Bottom Cushion (mm) at t=10ms.**

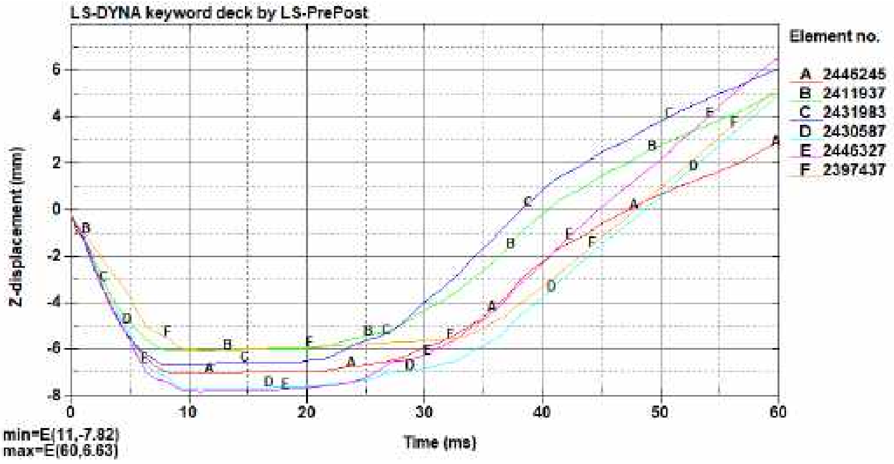

Figure 4-16. Bottom cushion elements' Z-displacement (height).

### 4.3.2. "Cover, Waveguide" Stress Analysis

As expected, the component "Cover, Waveguide" would also present high values in terms of stress on its bottom region, where the bracket is connected. In Figure 4-17 it is possible to be seen the distribution of stress along the component's surface, with values ranging from 0 (blue) to 283 (red) MPa, which is the yield stress value for this specific material. As the yield stress value is bigger than the one observed in the Cavity's material, the damage in terms of plastic deformation is, therefore, smaller (since the loading applied in both situations is of a similar nature).

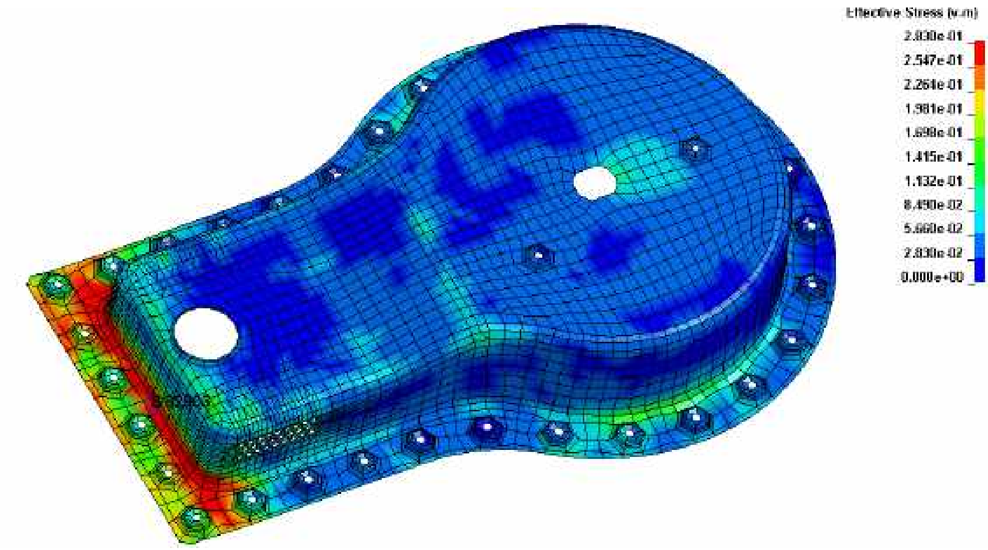

Figure 4-17. Von-mises stress analysis of the "Cover, Waveguide" (GPa) at t=10ms.

This stress distribution was also obtained from the instant t=10ms, and the element highlighted and chosen from the most critical section exhibit a stress variation over the simulation time as showed in the graph of Figure 4-18. The *Shell* element S82903 displays a peak stress value between t=10ms and t=10.5ms of 346 MPa. Before and after this point, the yield stress value is not exceeded for the remaining simulation time. This is not the highest overall stress value, but one of the highest from the critical area displayed before. The reason why this region has such a high-stress value at this moment in time was also already discussed on the Cavity stress analysis.

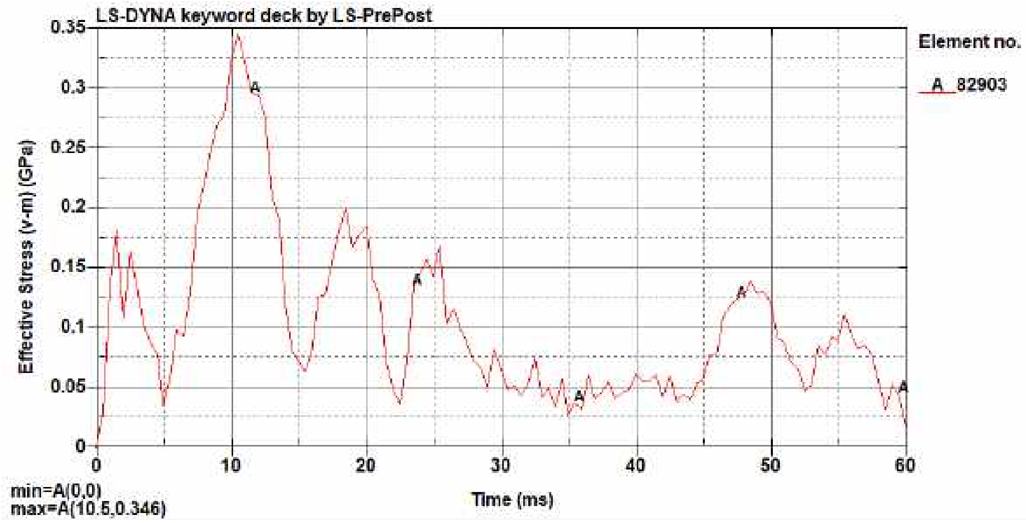

**Figure 4-18. Von-mises stress values for the element 82903.**

### 4.3.3. Bracket Magnetron Stress Analysis

For the Bracket component, the high stresses are predictable on the areas around the nodes to which the mass element is connected via *CONSTRAINED_NODAL_RIGID_BODY. In Figure 4-19 it is possible to be seen the distribution of stress along the component's surface, with values ranging from 0 (blue) to 170 (red) MPa, which is the yield stress value for the Bracket material.

This time, the stress distribution was obtained from the instant t=9ms, as it was in this moment the highest stress values were found in the elements around the nodal rigid body connection. The reason why there is this high-stress value a moment before than on the components connected to this one is owing to the fact that right before the moment of full compression on the cushion, tension is being created on the nodes connected to the nodal rigid body since it is being pulled by the Bracket Magnetron. As the maximum compression is reached at t=10ms, the Bracket stops its downward motion and tension stops due to the inertia gained by the nodal rigid body. At around t=11ms, this inertia is then felt on the same nodes and another stress peak is reached.

The *Shell* element S146997, which is one of the most loaded elements of the Bracket throughout the simulation, displays a peak stress value at t=9ms of 529 MPa, as shown in the graph of Figure 4-20. The stress values are most of the times very high and above the yield value during the whole simulation, but there can be seen several other peaks requiring particular attention as they represent the multiple rebound of the nodal rigid body on the Bracket's surface. This rebound created on the nodal rigid body happens due the oscillatory movement of the Bracket, as the Cavity (to which the Bracket is connected) displays high elastic deformations during the whole process. It is important to say that even though the peak at t=11ms (referred regarding to the inertia accumulated and felt after full displacement of the cushion) isn't as high as the one at t=9ms for this specific element analyzed, it is going to be as high or even higher if another element around either one the four critical areas were to be analyzed instead.

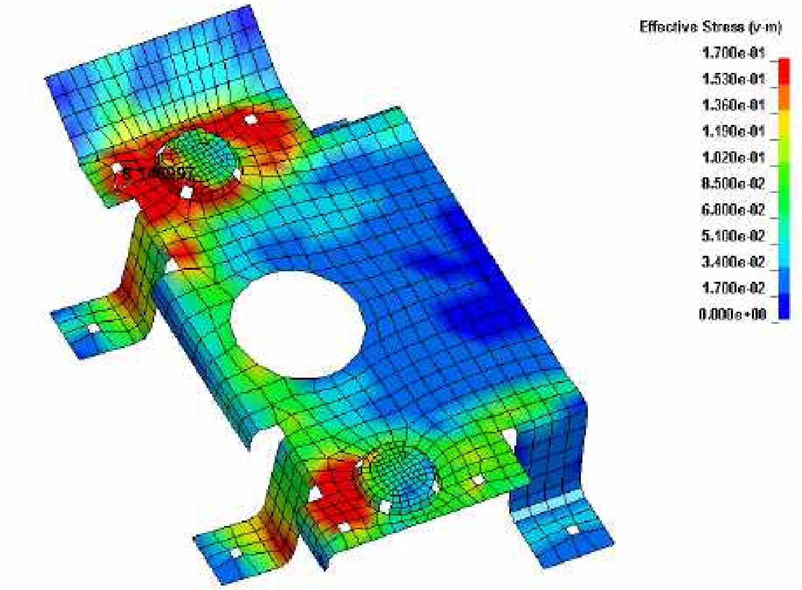

**Figure 4-19. Von-mises stress analysis of the Bracket Magnetron (GPa) at t=9ms.**

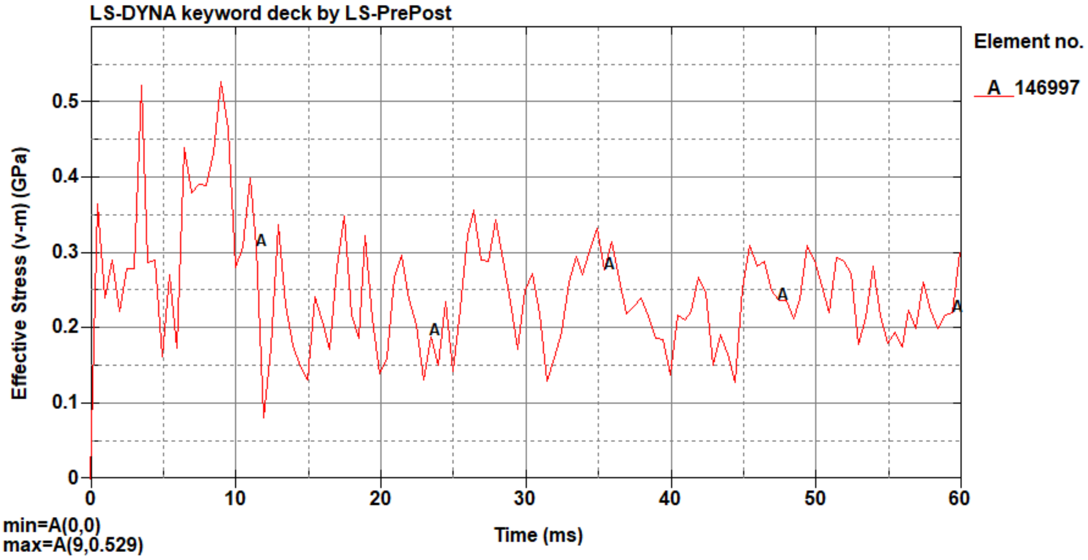

**Figure 4-20. Von-mises stress values for the Element 146997.**

Following the displacement along the z-axis (height) of the same element analyzed regarding the state of stress, it can be observed in the graph of Figure 4-21 the peaks mentioned above at t=10ms (when the cushion reaches the maximum deformation) and at t=20ms, t=25ms, t=45 ms, and t=57.5ms, which represent the wavering movement of the Bracket while its moving upwards due to the elastic deformations on the top of the Cavity.

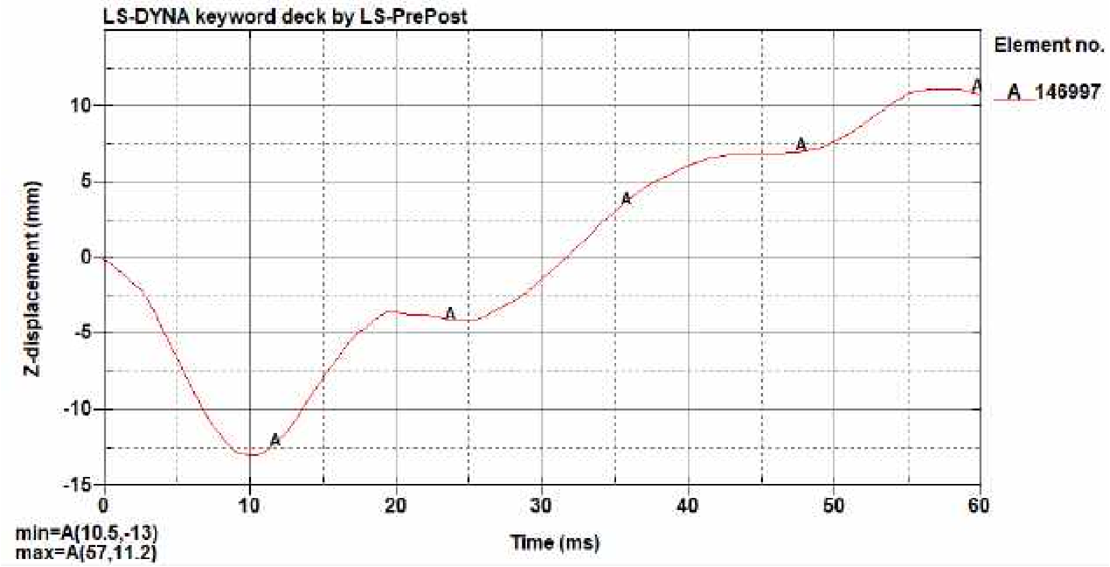

**Figure 4-21. Element number 146997 Z-displacement (height).**

### 4.3.4. Frame Front Stress Analysis

Another component displaying rather high stress values is the Frame Front, as this component hits the cushion with its bottom edge while the rest of the oven's structure keeps falling and penetrating the cushion frame due the weight involved. As shown in Figure 4-22, this situation creates a bending stress on the front lower edge and on both lower corners above the openings used for the integration of the hinges (seen in red).

The stress distribution represented in Figure 4-22 was retrieved from the instant t=10ms, as the greatest stress values emerge between instants t=9.5ms and t=10.5ms. Once more, this was predictable as the maximum cushion penetration happens around this moment in time. The *Shell* element S132650, randomly selected from the critical set of nodes on the front lower edge (and highlighted in Figure 4-22), displays a stress loading over time as shown in Figure 4-23, where it is possible to detect that even the peak stress value of 174 MPa is only slightly above the yield value (170 MPa for the Frame Front material).

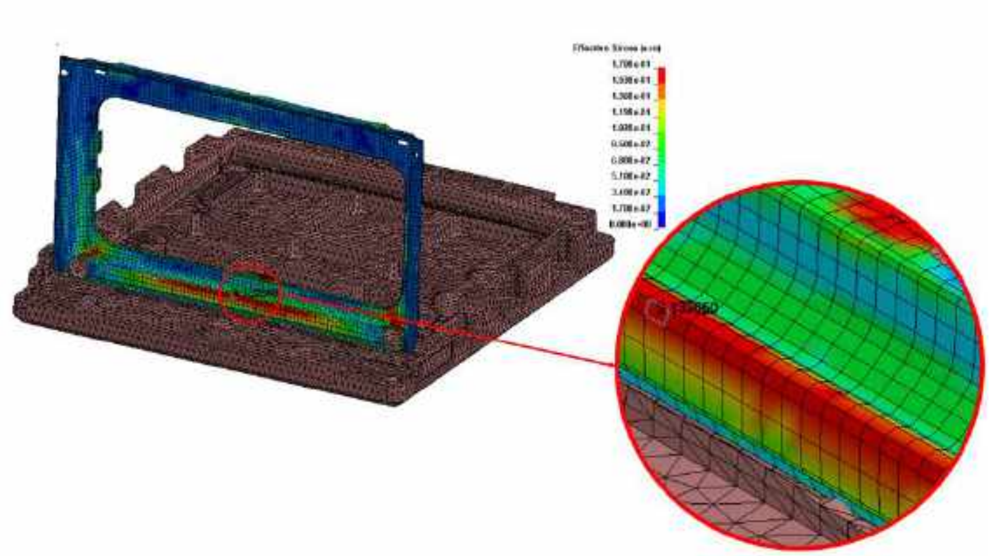

**Figure 4-22. Von-mises stress analysis of the Frame Front (GPa) at t=10ms.**

For the lower corners' region, the same cannot be said, as the peak stress on the highlighted *Shell* elements S133194 and S130900 in Figure 4-24 far exceeds the yield strength of the material. In the graph of Figure 4-25, it is possible to see that these elements fall into a plasticity regime between t=5ms and t=17ms due to being located on an area prone to high stress concentrations resulting from the geometry of the opening. For this reason, the plastic regime is reached long before the maximum cushion compression and lasts for a longer period of time after the oven's bounce on the cushion. It is also noticeable that the right corner enter a slightly higher stress state, which comes from the fact that the distribution of weight is unbalanced, and more weight is concentrated on the right-hand side of the oven. This will clearly induce more tension in this area, visibly susceptible to the appearance of stresses.

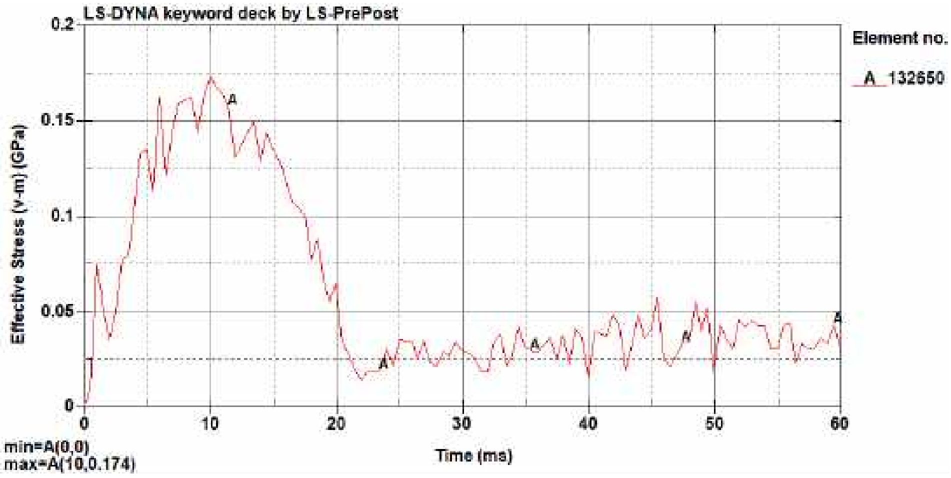

**Figure 4-23. Von-mises stress values for the element 132650.**

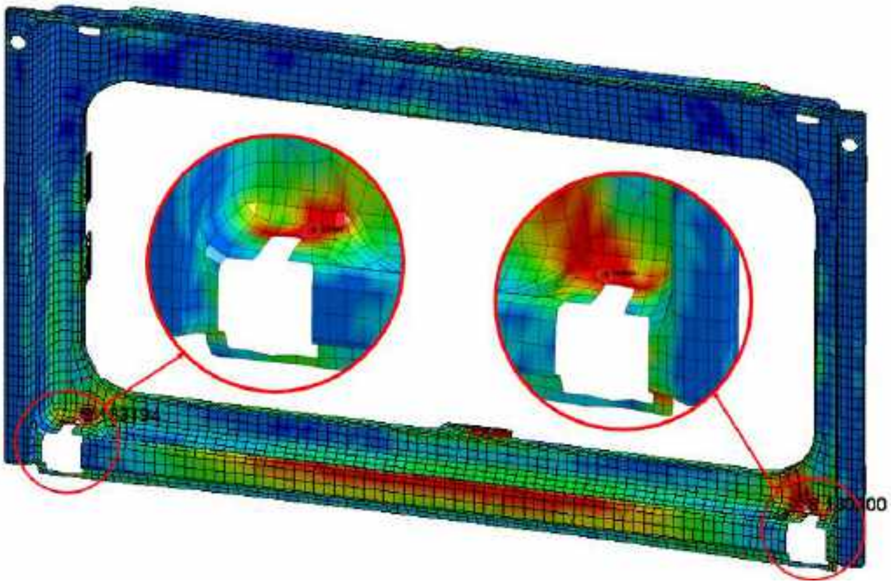

**Figure 4-24. Von-mises stress details on the lower corners' region at t=10ms.**

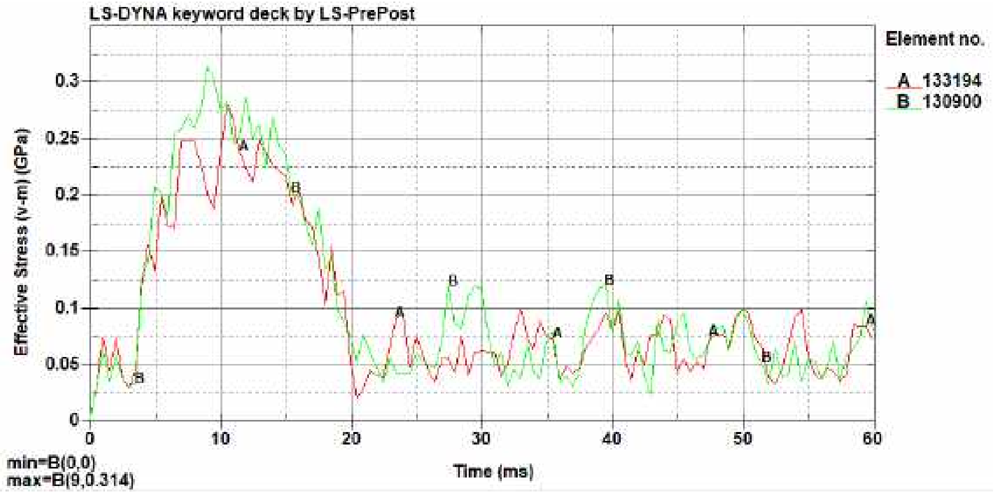

**Figure 4-25. Von-mises stress values for the elements 133194 and 130900.**

To corroborate this justification, the nodal displacement control along the z-axis (height) was employed in order to prove the stated unbalance. Looking at the displacement distribution along the Frame Front's surface at t=10ms in Figure 4-26, we can clearly verify the rotation of the oven to the right, confirming the weight unbalance and increase on this side that will make the stress value larger in contrast with the left opening.

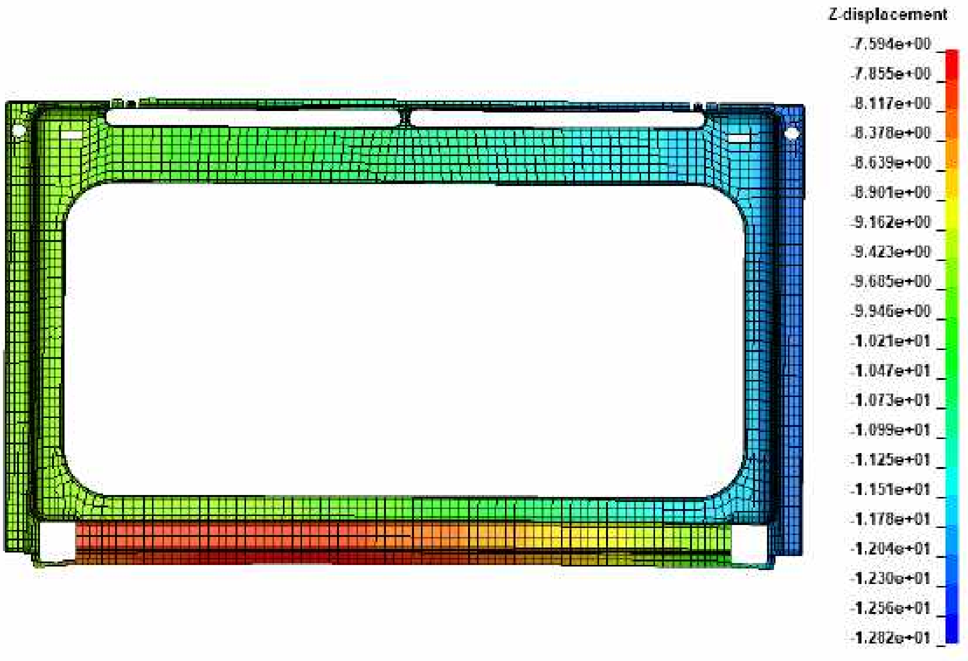

**Figure 4-26. Frame Front's Z-displacement (height) analysis (mm).**

Finally, to confirm the fact that when the bottom edge hits the cushion there is little penetration by the latter and a much bigger one by the rest of the oven (which leads to the appearance of bending stress), in Figure 4-28 the displacements of the elements highlighted in Figure 4-27 are shown, showing that at t=3ms the bottom elements (S132650 and S132797) stop descending as much and the top element (S133697) continues to go down with the rest of the structure. Around t=10ms is when it is possible to see the maximum displacement of the S133697 element.

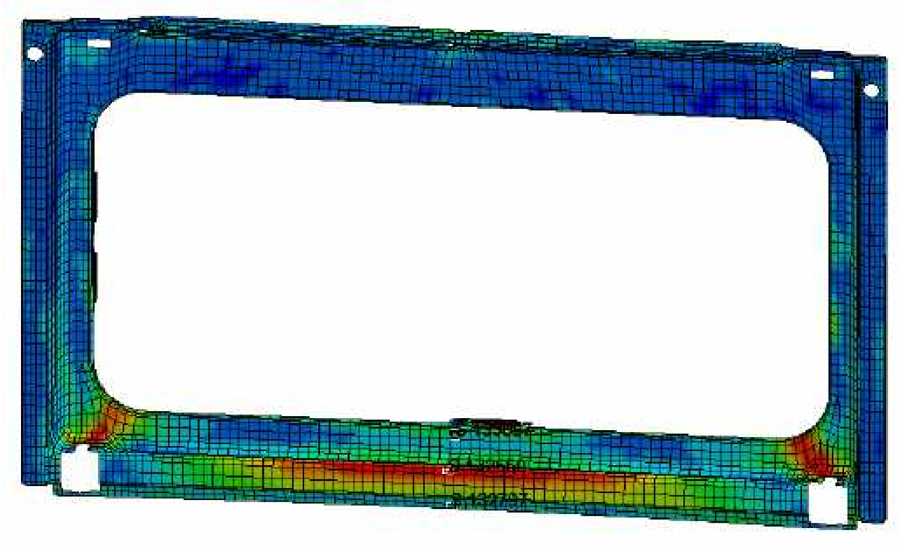

Figure 4-27. Elements highlighted on different sides of the Frame Front.

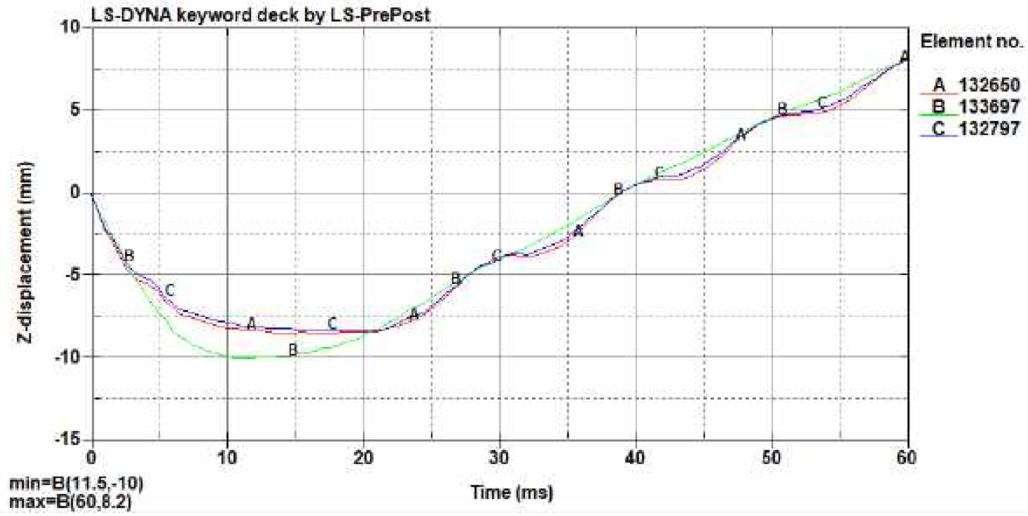

Figure 4-28. Frame Front elements' Z-displacement (height).

### 4.3.5. Bottom Element Protection Stress Analysis

The Bottom Element Protection component is connected to the Cavity by two front and two rear simple supports, as seen in Figure 4-29, which will likely experience high stress values at the moment of impact when the oven first starts to penetrate the foam. As this component has a relatively low yield strength value of 170 MPa, the plastic deformation will be very high at its structural supports.

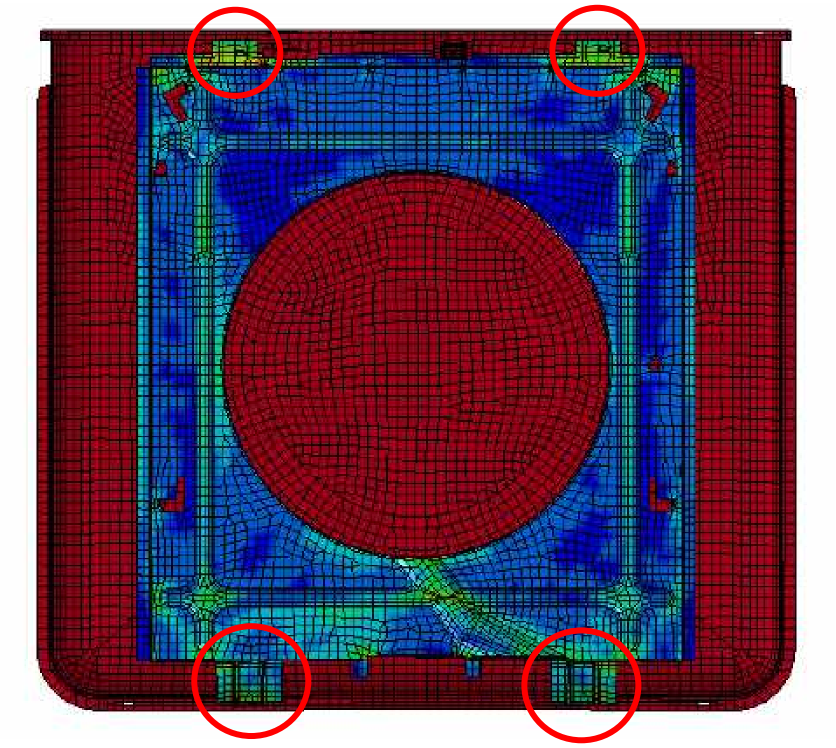

**Figure 4-29. Bottom Element Protection front and rear supports.**

As previously concluded in the Frame Front analysis, the overall weight of the oven is more concentrated on the right side which will make the penetration on the right side of the cushion a little bit higher. If this happens, the left side will reach maximum penetration beforehand the remainder of the structure and biggest stresses will be brought into the rear left-hand support of the Bottom Element Protection, as the oven is somewhat rotating.

The overall movement of this component starts by a first tilt to the right (see Figure 4-30 at t=5.5ms) and then a second tilt along the diagonal direction. Thus, when the oven is moving upwards after full penetration of the cushion, the stresses will be transferred directly to front right support and a slight bend is generated in the middle back half of the piece, as it can be seen through the displacement control of Figure 4-31 at the time instant t=12.5ms.

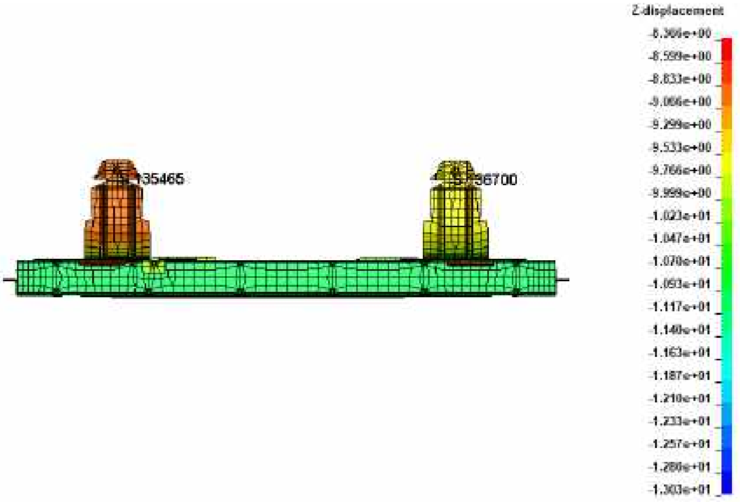

**Figure 4-30. Right tilt of the Bottom Element Protection assessed in the Z-displacement (height) analysis (mm) at t=5.5ms.**

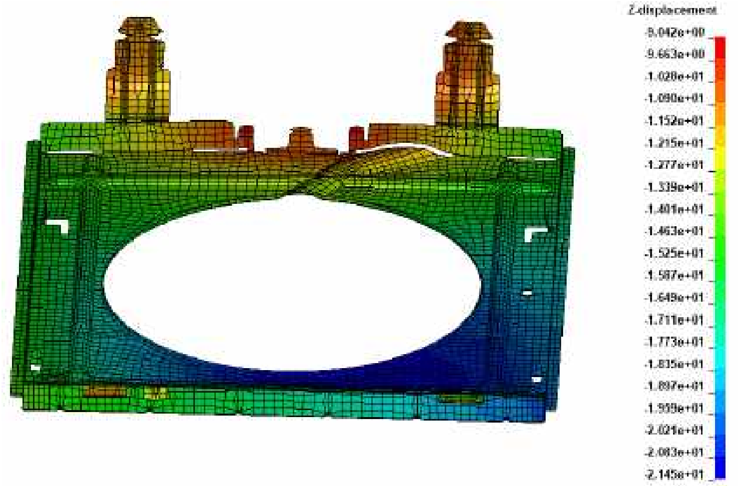

**Figure 4-31. Diagonal tilt of the Bottom Element Protection assessed in the Z-displacement (height) analysis (mm) at t=12.5ms.**

It is then easy to grasp that right after full penetration of the foam at t=10ms, the moment of the highest stress on the rear left support will appear. Through the graph of Figure 4-32, displaying the stress distribution of the *Shell* elements S135465 (left support) and S136700 (right support) highlighted in Figure 4-33, one may see that quite high loadings are experienced at the instant t=12.5ms by the element on the back left support as predicted. Just as the stress is distributed to the front right support, the component will bounce on this one and bend again on the middle back half but to the opposite direction, generating this time an extremely high shear stress loading on the rear right-support at the time t=25.5ms (see Figure 4-33). This is also visible in the graph of Figure 4-32, when the stress on the element S136700 located on the back right support starts to peak (and a similar situation happens at the time instant t=51ms).

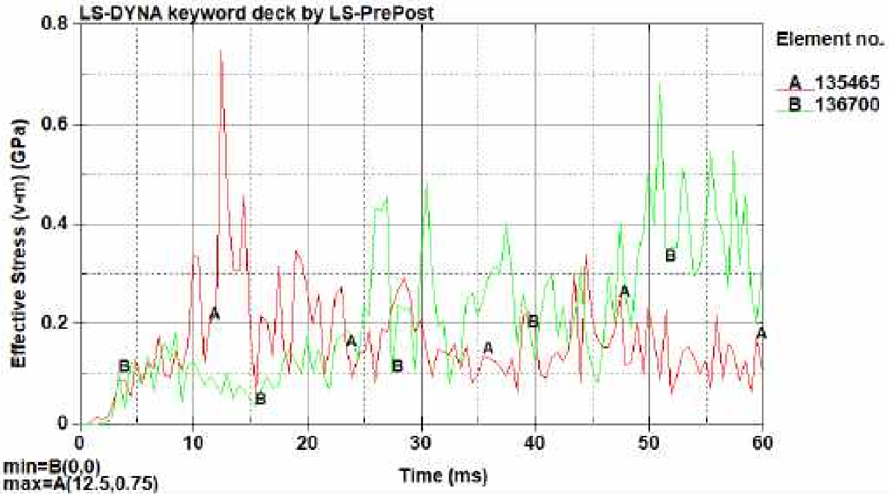

Figure 4-32. Von-mises stress values for the elements 135465 and 136700.

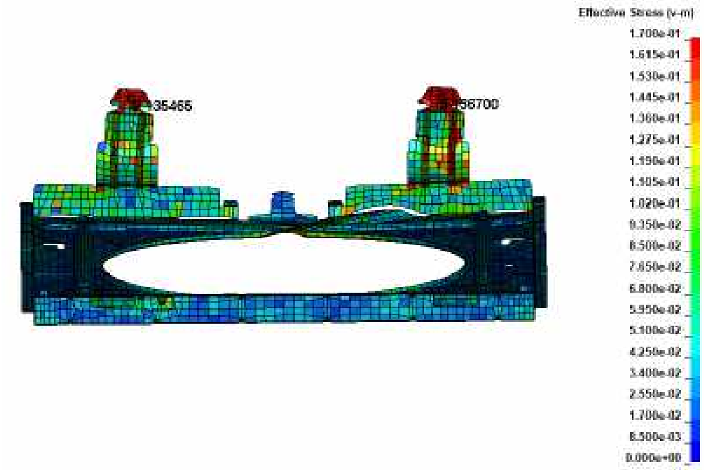

Figure 4-33. Von-mises stress analysis of the Bottom Element Protection (GPa) at t=25.5ms.

Just after the component tilts along its diagonal, the stresses on the front right support will increase in the same manner as the rear left-support, even though the magnitude of the stresses on these elements will be much lower than the ones on the first. The reason why this is verified is that the rear supports had already accommodate the biggest stress of the impact, which makes the front supports subjected to a slightly smaller loading. On top of this, the back supports have a certain geometry (on the hook that connects to the Cavity, see Figure 4-34 at t=13ms) that makes it rather prone to high stress concentration. After it bounces back, the stress is relieved and maintained below the yield value during most of the time.

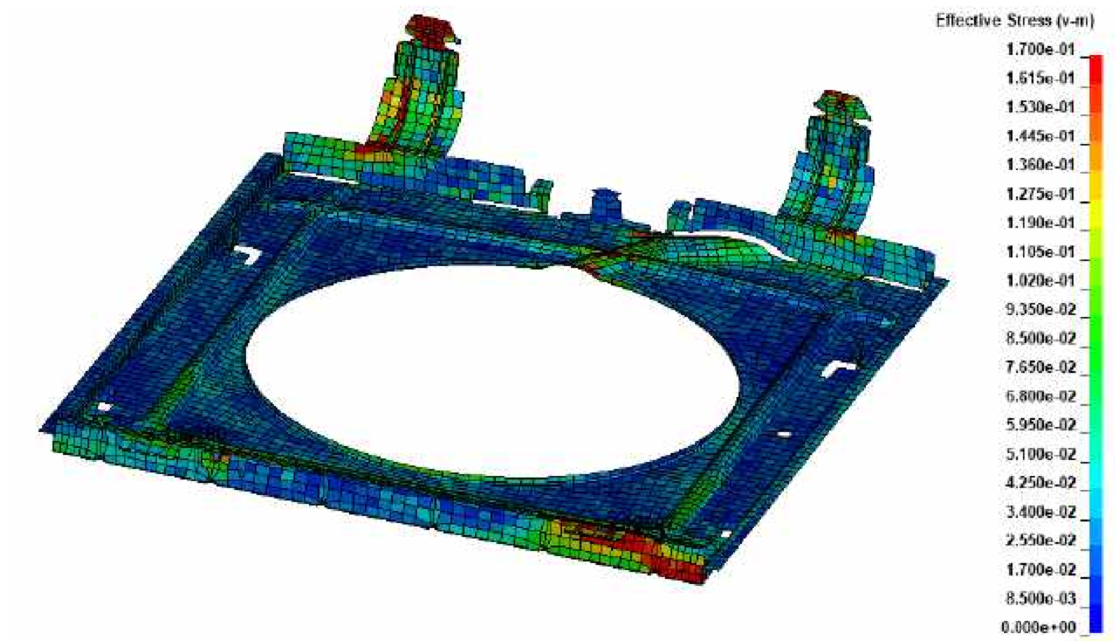

**Figure 4-34. Von-mises stress analysis with a detail on the diagonal tilt of the Bottom Element Protection (GPa) at t=13ms.**

As it is possible to validate by the graph of Figure 4-35, the randomly selected element on the critical area of the front left support (S134750) is subjected to a harder load than the one on the front right (S99897), and the highest global stress value is a lot smaller than on the rear supports (Figure 4-32) as already debated. The remaining of the Bottom Element Protection's structure, though, keeps the elastic regime during the whole simulation, unlike its supports.

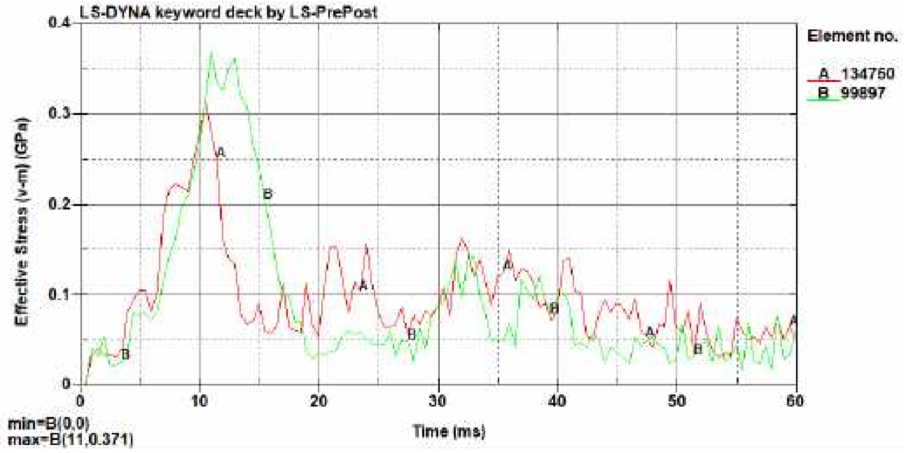

Figure 4-35. Von-mises stress values for the elements 134750 and 99897.

## 4.3.6. Housing Bottom Stress Analysis

The Housing Bottom component is the one element sustaining all the oven weight, at the structural supports area, during the impact instants. As the structural supports, like the Side panels and the Brackets and Supports set, are located close to the right and left edges of this component, these will be the zones where greatest stresses and deformations will be found at the moment of maximum penetration on the cushion. In Figure 4-36, one may observe the stress distribution on the Housing Bottom's surface, where it can be seen plastic deformation (above the yield value of 283 MPa for this material) on its sides.

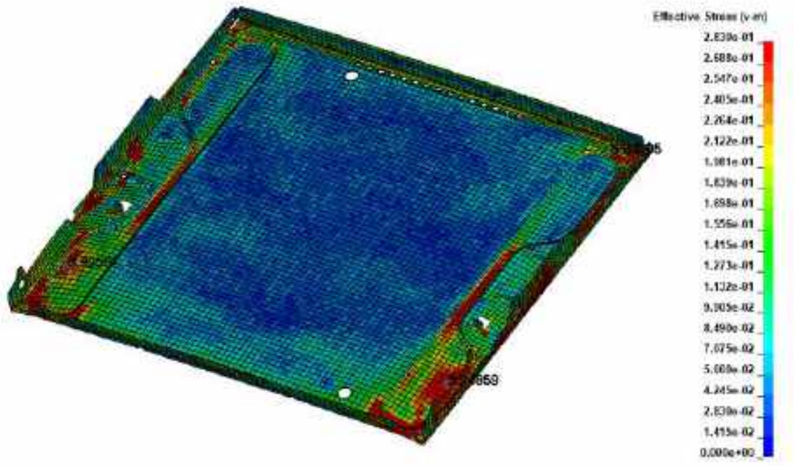

Figure 4-36. Von-mises stress analysis of the Housing Bottom (GPa) at t=10ms.

The stress distribution was taken from the instant t=10ms, which was proven to be the worst stress period to which the component was subjected, with an even bigger focus on the right side overall plastic deformation. The stress value is a little bigger and the plastic regime is more spread out on this side due to the weight of the oven being more concentrated on this half (as previously discussed).

The *Shell* element S94859 (highlighted in the front right half of Figure 4-36), which is one of the most loaded elements of the Housing Bottom throughout the simulation, displays a peak stress value at t=10ms of 502 MPa, as shown in the graph of Figure 4-37. The element S92587 (also highlighted on the front left half of Figure 4-36), as predictable, displays also a peak stress value at the same instant but with a relatively lower order of magnitude. The stress extent stands above yield right after the cushion compression begins around t=6ms and lasts until t=22ms, as the Housing Bottom starts to lose contact with the foam (due to loosening the contact between the structural supports and the latter component).

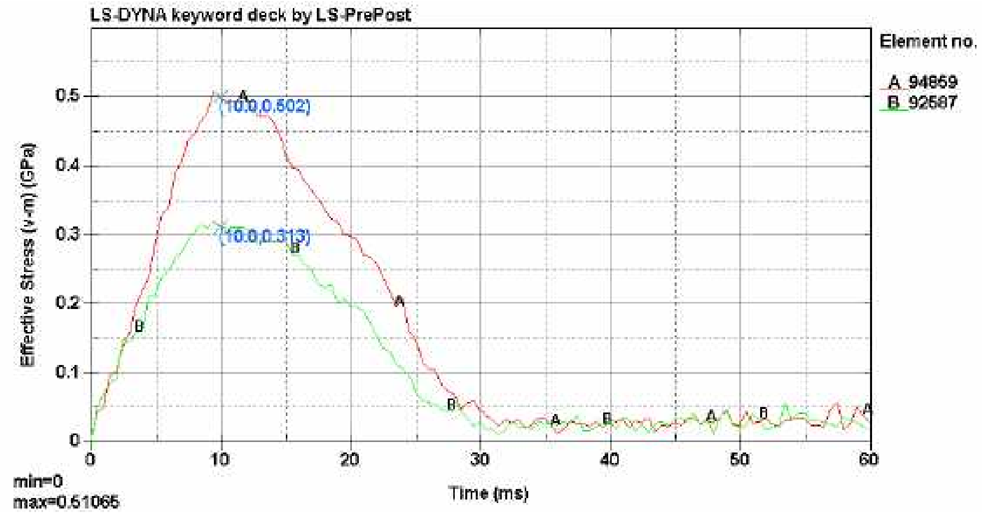

**Figure 4-37. Von-mises stress values for the elements 94859 and 92587.**

Comparing also the stress loading of the Shell element S94859, located on the critical area of the front right side, with the element S94205, located on the critical area of the rear right side, one can realize that the stress peaks don't happen at the same time, but one after the other (see Figure 4-38). The back half reaches the peak stress value around the instant t=5ms, whereas the front half peaks at t=10ms as previously discussed. This information leads to believe that the hindmost side of the oven penetrates additionally the foam initially, on the first contact between the oven and the cushion, and then a slight bounce is created to encourage an even bigger penetration on the front end, accompanied with a greater stress formation.

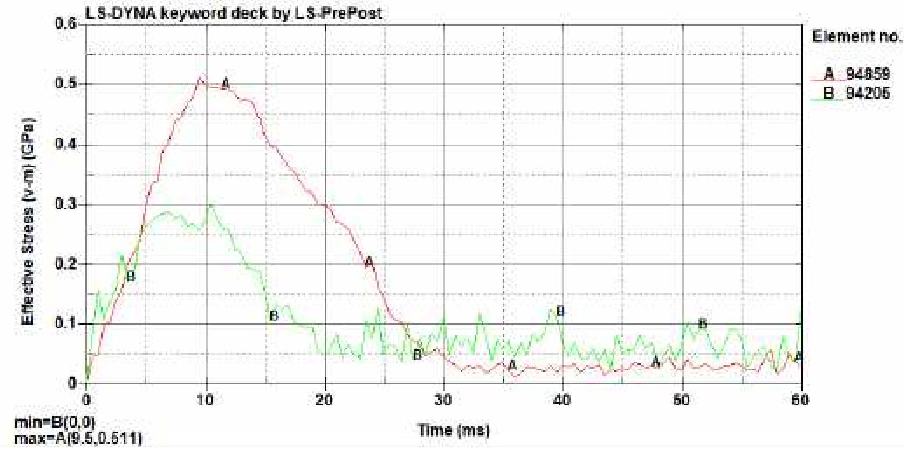

**Figure 4-38. Von-mises stress values for the elements 94859 and 94205.**

This is confirmed again by looking at the displacement distribution for this component at t=4ms (see Figure 4-39) when the rear side of the oven is below relatively to the front half, and observing the displacement distribution at t=20ms (see Figure 4-40) where it is clearly seen the front tilting due to the bounce that occurs.

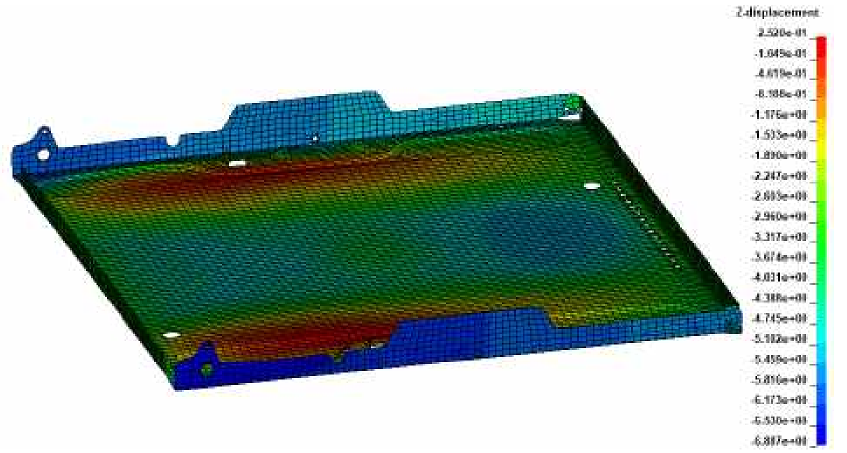

**Figure 4-39. Housing Bottom's Z-displacement (height) analysis (mm) at t=4ms.**

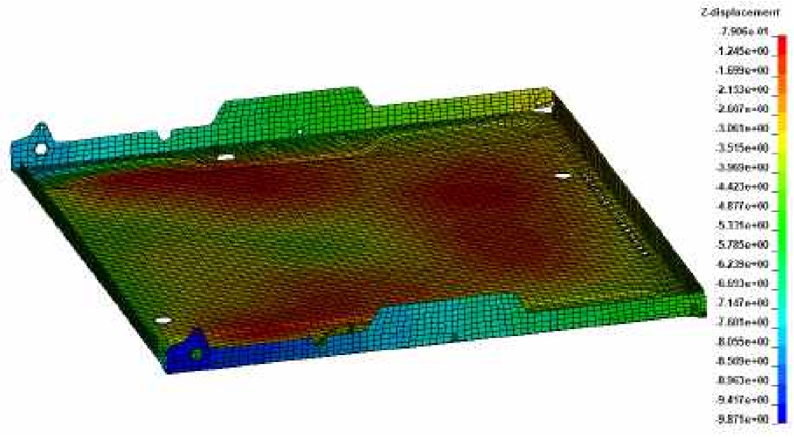

**Figure 4-40. Housing Bottom's Z-displacement (height) analysis (mm) at t=20ms.**

### 4.3.7. Carrier Stress Analysis

The Carrier, which shares the same material as the "Cover, Waveguide" and Housing Bottom, is one of the most crucial components in the entire oven as its primary goal is to carry all of the electronics appointed to make the oven operational. Due to the amount of weight it is carrying, rather high stresses at specific points in time are engendered and moderate displacements are transpired. As it is visible in Figure 4-41, the greatest loadings are observed in the middle back portion, on the rib frame visible in red, and on the edge of the transition grade to the transformer positioning zone similarly visible in red.

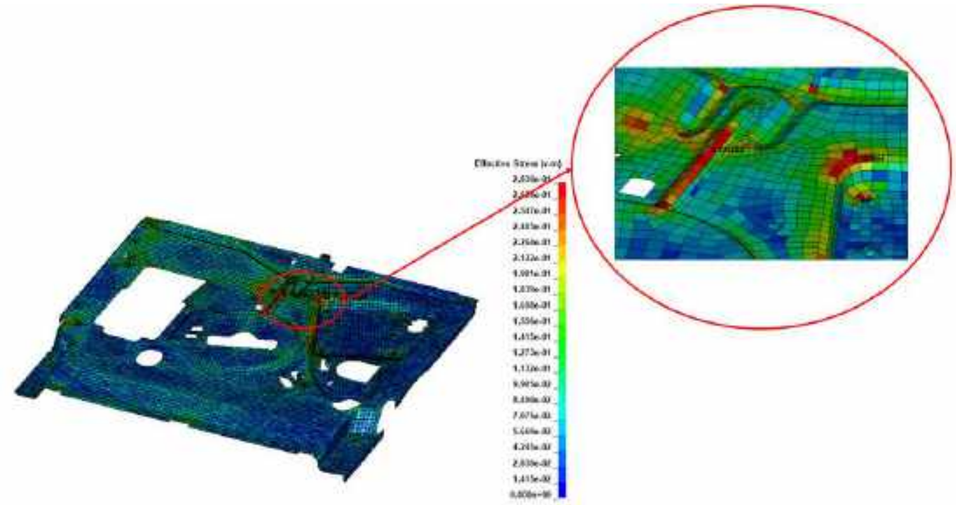

**Figure 4-41. Von-mises stress analysis of the Carrier (GPa) at t=14ms.**

This stress distribution was obtained from instant t=14ms in which the most critical period was observed in this component. The two elements highlighted in Figure 4-41, which are *Shell* elements S139233 and S137994, have the stress values to which they are subjected over the simulation time represented in the graph of Figure 4-42. The highest stress values appear in both elements at the instants t=14ms and around t=25ms to t=26.5ms, however, only the first peak reaches plastic deformation, remaining the entire structure in the elastic regime for the remaining simulation time.

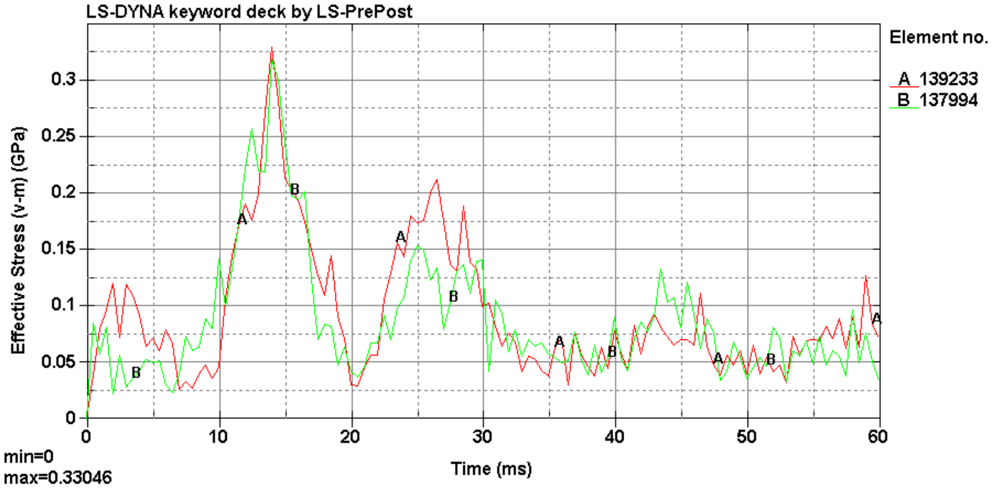

**Figure 4-42. Von-mises stress values for the elements 139233 and 137994.**

When the oven reaches its maximum displacement, the Side panels stop their descending motion and since the Carrier is resting on these parts, it starts to bend due to the inertia effect of the components being carried (special attention is required to the transformer and cooling fan's weight, with the last one represented by a mass element and connected to the Cooling Channel, as seen in Figure 4-43). In the graph of Figure 4-42 it is thus perceived that at t=10ms (maximum deflection of the cushion), the stress value on both previously mentioned nodes start to build until the peak value at t=14ms, reaching the maximum bend at this stage, limited by the Carrier's stiffness.

After this point, the piece starts to unbend as the oven structure is moving upwards and reaches maximum bend on the opposite direction, represented by the next stress peak observed in the graph of Figure 4-42 between the instants t=25ms and t=26.5ms. At this point, there is no opposing force (as the oven is still ascending) on the Carrier to make it deflect to a greater extent and, therefore, the stress value isn't as severe as the first case and does not surpass the yield strength value.

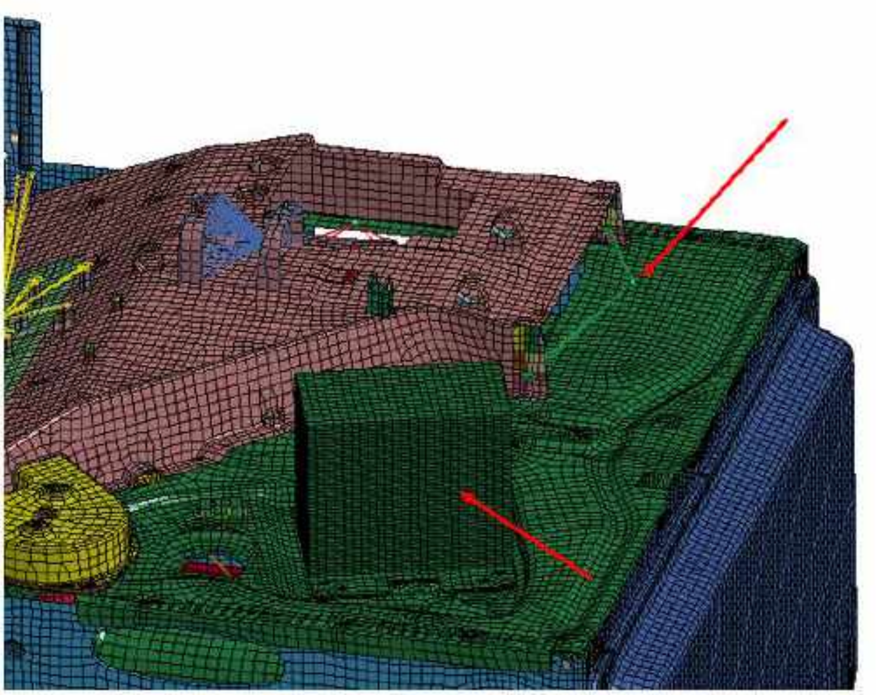

**Figure 4-43. Highlighting of the Transformer and Cooling Fan's representation.**

By observing the displacement distribution for this component, another contributor to the stress peak at t=14ms is found. In Figure 4-44, displaying the displacements at t=13.5ms, it is seen the Carrier hitting the "Cover, Waveguide" component. When this bump happens, the areas around the hitting zone (seen in blue) cave in a little bit more than they would've if there was no impact, and together with the Transformer and Cooling Fan's weight a major bending load is produced on the aforementioned rib frame and edge of the transition grade to the Transformer's positioning zone.

This situation also implies that the contact modelling between these components was well performed and impact forces were suitably distributed and applied on both parts. This is crucial when developing a finite element numerical model for crash analysis, as the penetration between parts will not reveal very significant information and will clutter the model's behavior.

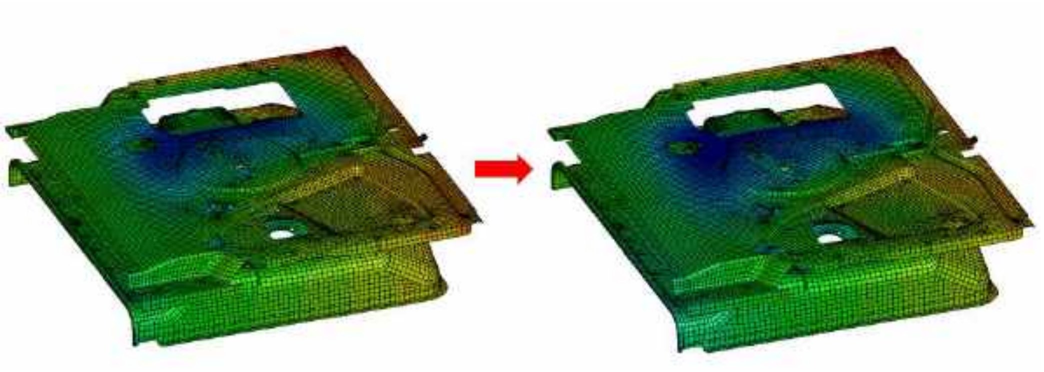

**Figure 4-44. Carrier's Z-displacement (height) analysis (mm) at t=13.5ms and t=14ms.**

### 4.3.8. Effect of Thermal Shrinking on the Foil

When analyzing the stresses on both the Supports and Brackets without pre-stressing on the Foil component, it is possible to find a slight peak stress above the yield value on both the left and right-hand side groups, but at different points in time. The first set where this is observed is on the left one, noting an increase of the stress level in the area of the Bracket contacting the Housing Bottom, and in the area of the Support which in turn is in contact with the former (as seen in Figure 4-45). Both components share the same material, which holds a yield strength value of 283 MPa.

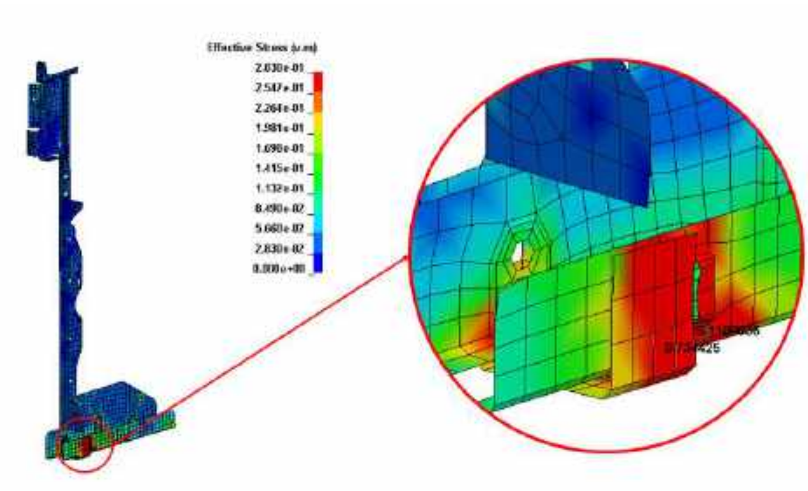

**Figure 4-45. Von-mises stress analysis of the Left Bracket and Support (GPa) at t=15.5ms.**

This stress distribution was obtained from instant t=15.5ms in which the most critical period was observed for this specific set (left one). The *Shell* elements highlighted in the critical area of both components (S734425 on the bracket and S1166036 on the support) have a stress variation over time as seen in Figure 4-46, where it is noticeable that other than at the peak of t=15.5ms where the global maximum stress of 416 MPa is found, no plasticity occurs on either component.

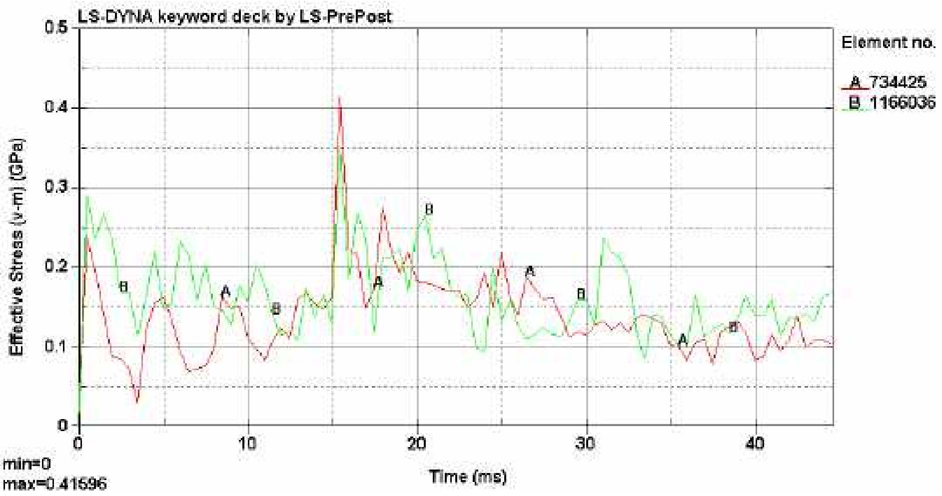

**Figure 4-46. Von-mises stress values for the elements 734425 and 1166036.**

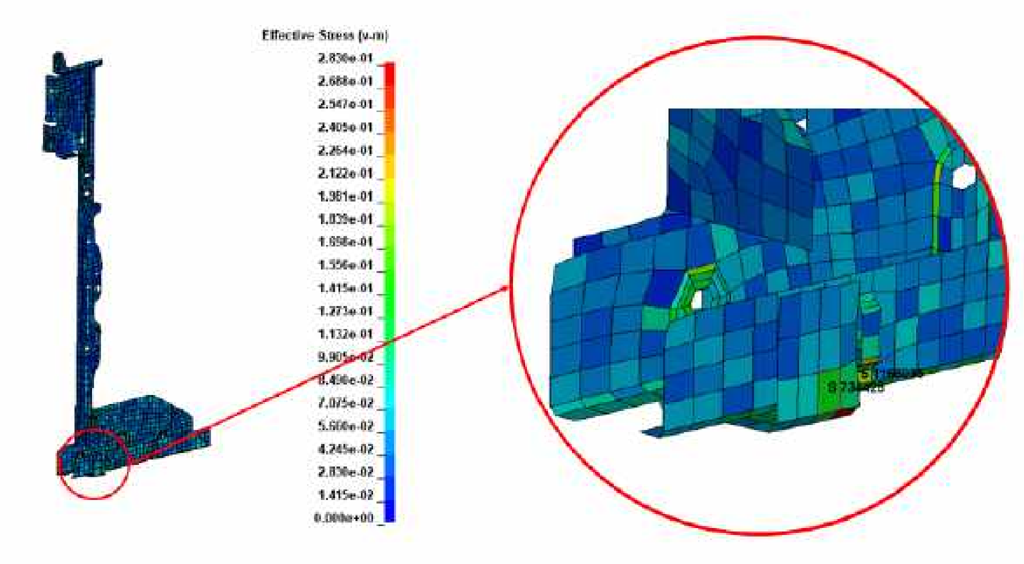

**Figure 4-47. Von-mises stress analysis of the Left Bracket and Support with the Foil's pre-stressing (GPa) at t=15.5ms.**

When the pre-stressed simulation is analyzed at the same instant of t=15.5ms, the previously critical area of the left set of Bracket and Support no longer looks as it did in Figure 4-45, but have an appearance right now as displayed in Figure 4-47.

The *Shell* elements highlighted on the formerly critical area of both components (which are the same as the ones highlighted in the first simulation) have now a stress variation over time as seen in Figure 4-48, where it is possible to conclude that the stress peak found in the unstressed simulation at t=15.5ms is no longer existent and the overall stress values remain always below yield and even decrease over time. There is only a subtle peak for the S1166036 element that falls just a little over the yield value, but being only due to the moment of impact and the place where this element is located (just below a small groove in the Support), which is somewhat susceptible to stress concentrations (see Figure 4-49).

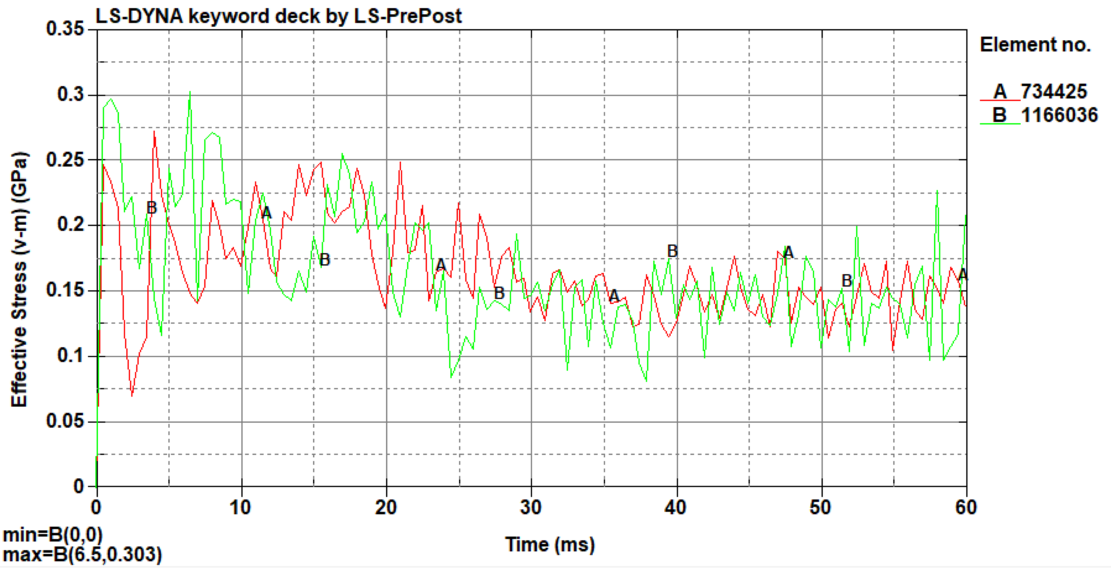

**Figure 4-48. Von-mises stress values for the elements 734425 and 1166036 in the Pre-Stressing simulation.**

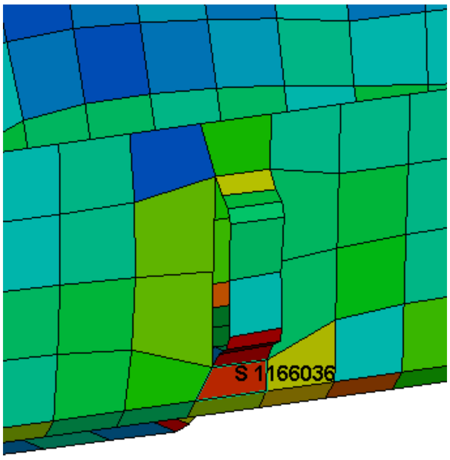

**Figure 4-49. Location of the 1166036 element on the left Support at t=10ms.**

The stress distribution along the right-hand set of components, in the unstressed simulation, is verified to be at its worst case at the instant t=21.5ms, on the exact same location as the first set mentioned (seen in Figure 4-50).

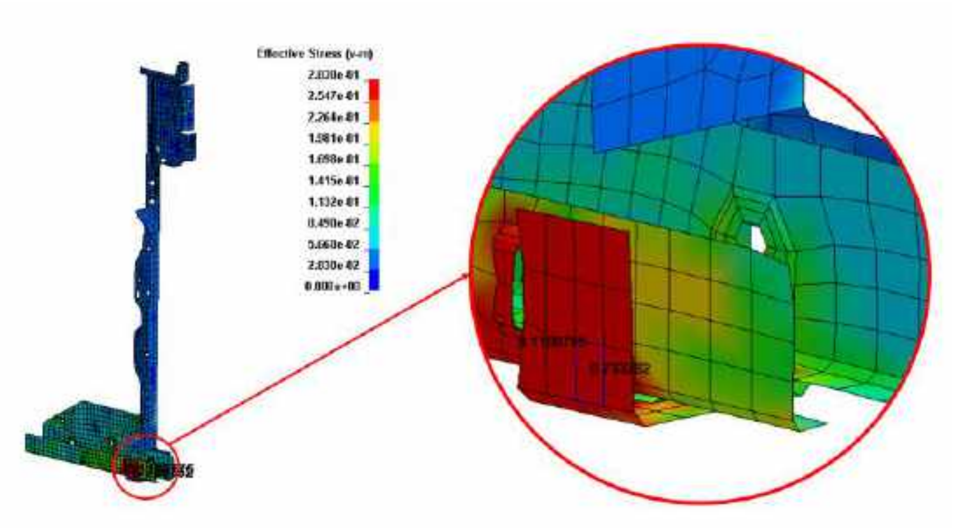

**Figure 4-50. Von-mises stress analysis of the Right Bracket and Support (GPa) at t=21.5ms.**

The stress variation, seen in the graph of Figure 4-51, for the S733362 and S1166776 elements confirms that between the moments t=21.5ms and t=22.5ms it is verified a peak stress value of 586 MPa (depending on which specific elements are being analyzed, the peak stress would be either at t=21.5ms or t=22.5ms). Again, except at the highest overall peak of stress, the tension state is always below the yield strength.

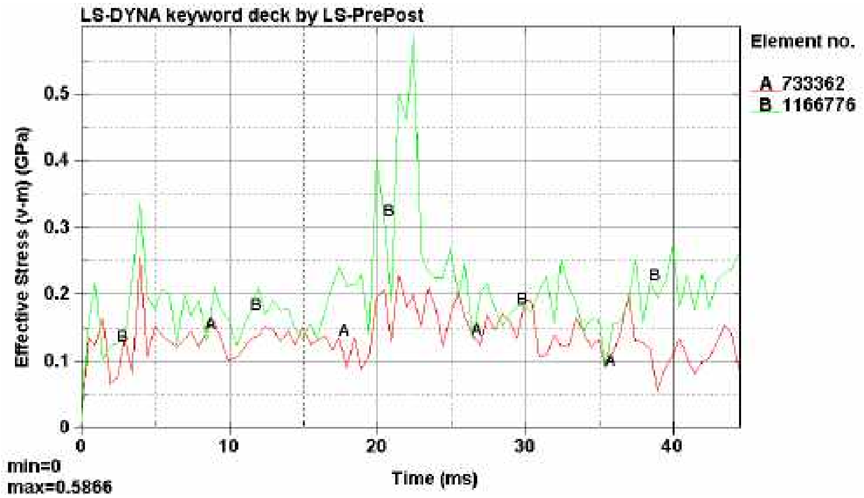

**Figure 4-51. Von-mises stress values for the elements 733362 and 1166776.**

Analyzing now the pre-stressed simulation at the same time instant of t=21.5ms, the critical area found on the right set of Bracket and Support is no longer critical, and looks now as in Figure 4-52.

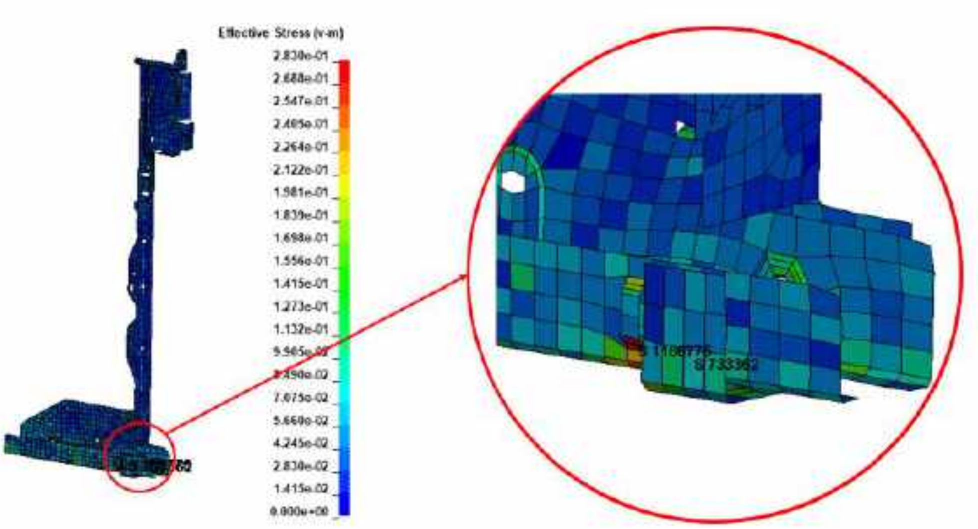

**Figure 4-52. Von-mises stress analysis of the Right Bracket and Support with the Foil's pre-stressing (GPa) at t=21.5ms.**

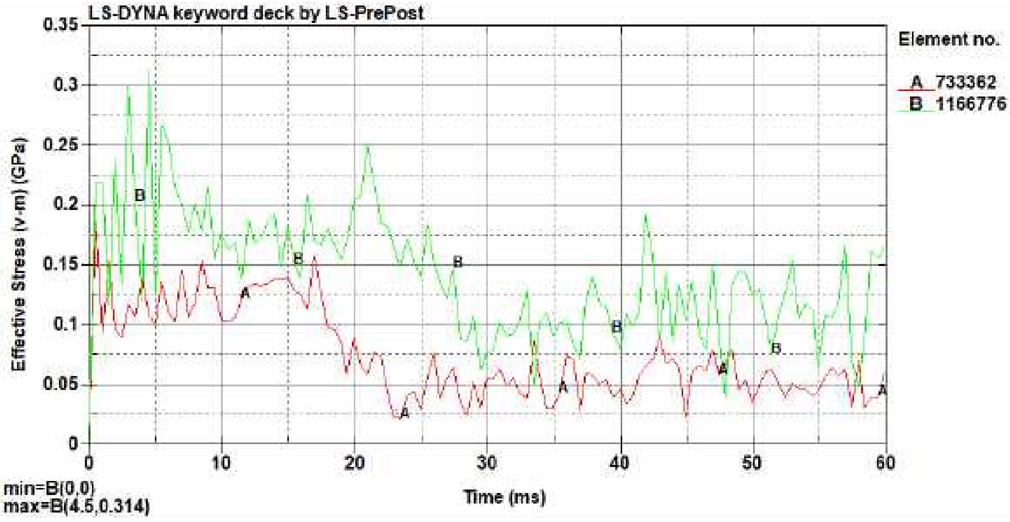

**Figure 4-53. Von-mises stress values for the elements 733362 and 1166776 in the Pre-Stressing simulation.**

It is possible to conclude once again by analyzing the graph of Figure 4-53, that the *Shell* elements which were once critically loaded in the unstressed simulation, are no longer critical and do not reach plasticity during the entire simulation time. Just as the left set, this one remains always below yield stress and the stress values also decrease over time, although it also exhibits a subtle stress peak for the element S1166776 that falls a little over the yield value for the exact same reason as the S1166036 element on the left set.

Although these are considered critical components due to the prevailing folds in their structures (especially in the lower portion of the Bracket where the Support is resting) and low thicknesses allied, the thermal shrinking on the Foil demonstrated an important role in reducing loadings at various locations in the oven's structure. Certainly, when the Bracket is most compressed at t=10ms it still displays some damaging loadings on the first fold, but nothing similar to the unstressed condition, where the stresses on that areas were highly amplified.

The *Shell* element S733328 seen in Figure 4-54 and located on the fold seen in the side part of the Bracket (which is connected to the Side panels) is in a compression state during the downward motion of the oven, and as it would be expected, displays a maximum stress loading at around the instant t=10ms (seen in Figure 4-55). After full compression, the Bracket is progressively deloaded as the oven is bouncing, until the stress value falls below yield and remains quite low for the remaining time.

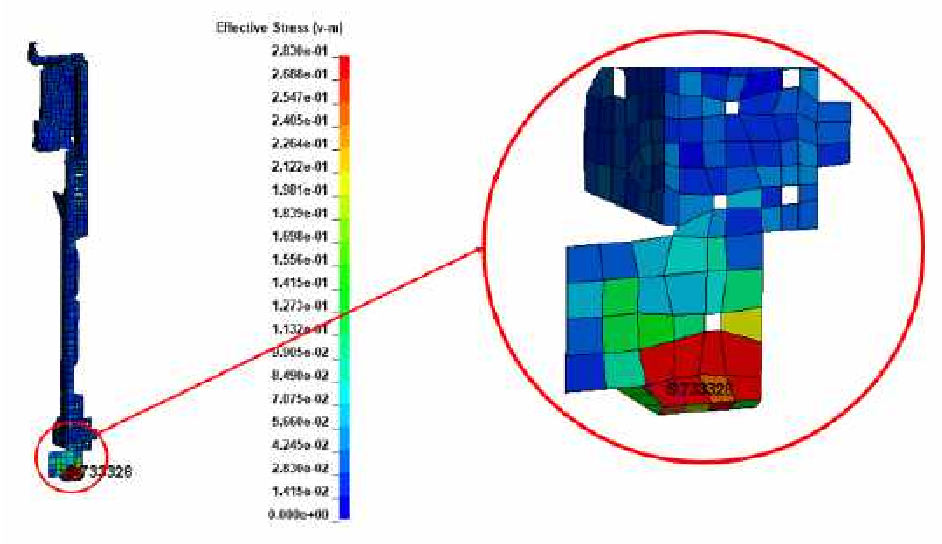

**Figure 4-54. Location of the 733328 element on the Left Bracket at t=10ms.**

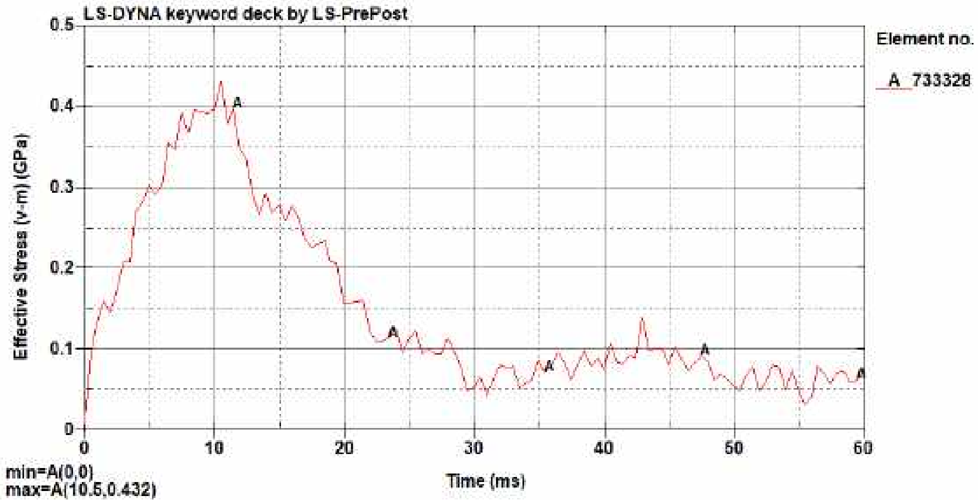

**Figure 4-55. Von-mises stress values for the elements 733328.**

Finally, it is important to remark that even though this stress alterations were found on these components, not every single one produced these kind of results. This being said, most of constituent components of the numerical model showed little to no alterations on their stress state, as for example the ones analyzed on this present section. Also, these effects may not fully correspond to the real case, due to the assumptions that were considered in the thermal shrinking effect modelling.

### 4.3.9. Final Considerations

To finish off this chapter, some final considerations must be addressed regarding the loading stresses on structural components. The first observation refers to the screw modelling using the *spider connection* technique, as the practice of this type of modelling creates a fairly high stress concentration on the elements composed by the nodes where the rigid beams are connected. Hence, when the stress distribution is analyzed on components containing *spider meshes*, the results may become drastically exaggerated.

Looking at the stress distribution along the Top Panel's surface for example (see Figure 4-56), it is easily visible the high stress concentration on the elements around the connection between this component and the Bracket. Although traction and shear stresses will be brought to these elements as any of the components try to pull out from each other, the stress value is always amplified to a greater magnitude than what would be expected in the physical model.

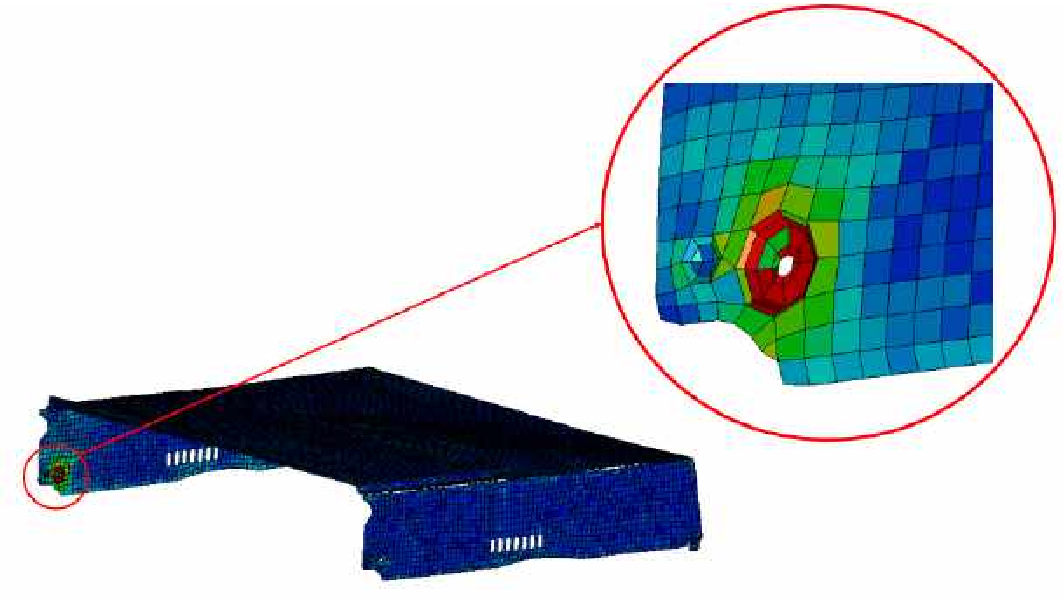

**Figure 4-56. Von-mises stress analysis of the Top Panel (GPa).**

The second observation requiring special attention has to do with the structural parts contained in the Choke group, that as already seen in the “Energy Balance” section, present an improperly defined contact (number 174) containing negative contact energy. Due to this contact malfunction, an unrealistic load happens to the Choke components, making them go straight into the plastic domain from t=0ms to t=0.5ms (as seen in Figure 4-57).

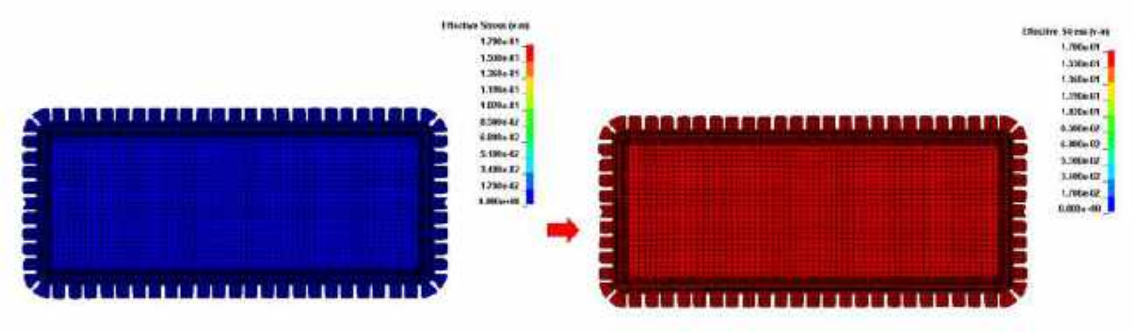

**Figure 4-57. Von-mises stress analysis of the Choke at t=0ms and t=0.5ms.**

Although the loading is observed to be exceeding the expected value for this component and that results are found to be unrealistic during the whole simulation time, the deformations don’t seem to have any practical meaning and are not executing any exaggerated forces on other components spreading this adulterated behavior. Due to the positioning and structural assembly of this component inside the door, it is not expected the presence of high stresses in the execution of the drop test, and for this reason the behavior of this group of components is not also of great value for analysis. It is reaffirmed that this particularity will not constitute a major problem when it comes to the validity of the results obtained by the numerical model.

The third and final relevant consideration to taken in account is that from the stress analysis presented above, it is finally known that the oven components require a material conversion to elasto-plastic material with linear hardening, to represent in a totally realistic way the overall behavior of the oven. This will lead not only to obtaining more approximate acceleration curves, since the residual deformations are being considered, but also to the possibility of analyzing these same plastic strains. The information to accomplish this, is all detailed on the “Characteristics of the Employed Materials” section of the third chapter.

# 5

# Chapter 5 - Conclusion and Future Works

The development of this dissertation was based on the construction of a finite element numerical model, using the *software LS-PrePost*, of an oven model with the purpose of numerically replicating a drop test, used in the design phase for the approval of its structural integrity for safe transportation.

The process used in the construction of this numerical model is based on a demanding iterative process, requiring special attention throughout, in order to be realized in an expedite and scrupulous manner without compromising each posterior and following phase of the project. While building the numerical model, numerous proceedings and techniques found and used in the literature were employed, to ensure a well-functioning model and maintain the correct procedure from the beginning to the final phase, and avoiding too many changes that would require a great number of repetitive simulation runs. The research and methodology used to produce the final numerical model exposed in this dissertation, may and must be used as an orientation for future developments of numerical models used in the design phase of electrical appliances, offering this way a more convenient, faster, and more efficient modelling method.

After the successful simulations of the drop test, the critical components which were sustaining moderate to high loads were analyzed, and the motion of the oven was found to be in a good correlation with the one found on the experimental test performed by Electrolux on the physical model. The model was also successfully validated both in terms of energy and motion dynamics, as the acceleration curves in both the numerical and physical experimentation were very similar and presented an equally similar kinematic response qualitatively. Although there are small differences, these are only due to the difficulty of precisely replicating the experimental test due to uncontrollable physical constraints, since each experimental test is always different from the former even when controlled under specific conditions.

Even though there was a countless amount of time invested on correcting the final behavior of the full numerical model, the extensive simulation times to perform this analysis contributed to the impossibility to have a completely accurate finite element model. However, the problems encountered were found not have any implication on the overall model performance and very satisfactory results were obtained on how the oven was being loaded during the simulation time, to assess which parts were critical to withstand the structural integrity. Bearing this in mind, a future investigation on the optimization of this numerical model in terms of reduction of the simulation time, would have a great impact on upcoming ventures revolving around the analysis of other designs.

To conclude, it would be quite interesting succeeding this dissertation the completion of the methodology for the structural optimization of electrical home appliances, by performing any type of design optimization algorithm using the developed numerical model.

# References

Altair Engineering. (2018). *Hypermesh*. Retrieved from https://altairhyperworks.com/product/HyperMesh

ASTM International. (2014). ASTM D1596-14, Standard Test Method for Dynamic Shock Cushioning Characteristics of Packaging Material. *West Conshohocken, PA*, (www.astm.org).

ASTM International. (2015a). ASTM D4168-95(2015), Standard Test Methods for Transmitted Shock Characteristics of Foam-in-Place Cushioning Materials. *West Conshohocken, PA*, (www.astm.org).

ASTM International. (2015b). ASTM D880-92(2015), Standard Test Method for Impact Testing for Shipping Containers and Systems. *West Conshohocken, PA*, (www.astm.org).

ASTM International. (2015c). ASTM D999-08(2015), Standard Test Methods for Vibration Testing of Shipping Containers. *West Conshohocken, PA*, (www.astm.org).

ASTM International. (2016). ASTM D4169-16, Standard Practice for Performance Testing of Shipping Containers and Systems. *West Conshohocken, PA*, (www.astm.org).

ASTM International. (2017a). ASTM D4728-17, Standard Test Method for Random Vibration Testing of Shipping Containers. *West Conshohocken, PA*, (www.astm.org).

ASTM International. (2017b). ASTM D5276-98(2017), Standard Test Method for Drop Test of Loaded Containers by Free Fall. *West Conshohocken, PA*, (www.astm.org).

Bala, S. (2006). *Overview of Mass-Scaling in LS-DYNA*. Retrieved from https://www.d3view.com/2006/10/overview-of-mass-scaling/

Bala, S., & Day, J. (2013). General Guidelines for Crash Analysis in LS-DYNA. Retrieved from http://ftp.lstc.com/anonymous/outgoing/jday/faq/guidelines.pdf

Belingardi, G., Montanini, R., & Avalle, M. (2001). Characterization of polymeric structural foams under compressive impact loading by means of energy-absorption diagram. *International Journal of Impact Engineering*, *25*(5), 455–472.

Bielenberg, R. W., & Reid, J. D. (2004). Modeling Crushable Foam for the SAFER Racetrack Barrier. *8th International LS-DYNA Users Conference*, 1–10.

Blanco, D. H., Ortalda, A., & Clementi, F. (2015). Impact simulations on home appliances to optimize packaging protection : a case study on a refrigerator. *10th European LS-DYNA Conference 2015*, (score 1).

Burgess, G. (1990). Consolidation of cushion curves. *Packaging Technology and Science*, *3*(4), 189–194. https://doi.org/10.1002/pts.2770030403

Chen, Z. (Kobe U. (2014). *Study on Improvement of Evaluation Methodology of Cushioning Packaging*. Kobe University.

Cronin, D. S., & Ouellet, S. (2016). Low density polyethylene, expanded polystyrene and expanded polypropylene: Strain rate and size effects on mechanical properties. *Polymer Testing*, *53*, 40–50. https://doi.org/10.1016/j.polymertesting.2016.04.018

Cronin, Duane S, Bui, K., Kaufmann, C., Mcintosh, G., Berstad, T., & Cronin, D. (2003). *Implementation and Validation of the Johnson-Holmquist Ceramic Material Model in LS-Dyna*. 47–60.

Croop, B., & Lobo, H. (2009). Selecting material models for the simulation of foams in LS-DYNA. *7 Th LS-DYNA European Conference*. Retrieved from http://www.dynamore.de/de/download/papers/konferenz09/papers-depr/D-II-04.pdf

Department of Defense. (1997). *PACKAGE CUSHIONING DESIGN - MIL-HDBK-304C*.

EHP/EUROPE. (2004). *PACKAGING TEST EHP LAUNDRY*. 29.

Goyal, S, Upasani, S., & Patel, D. M. (1998). *Improving Impact Tolerance of Portable Electronic Products : Case Study of Cellular Phones*. 43–52.

Goyal, Suresh, & Buratynski, E. K. (2000). *Methods for Realistic Drop-Testing The International Journal of Microcircuits and Electronic Packaging*. *23*(c), 45–52.

Hallquist, J. O. (2006). *LS-DYNA Theory Manual*. Retrieved from www.lstc.com

Hwan, C.-L., Lin, M.-J., Lo, C.-C., & Chen, W.-L. (2011). Drop tests and impact simulation for cell phones. *Journal of the Chinese Institute of Engineers*, 337–346.

International Organization for Standardization. (1985). ISO 2248:1985, Packaging -- Complete, filled transport packages -- Vertical impact test by dropping. *Geneve, Switzerland*, (www. iso.org).

International Organization for Standardization. (2000a). ISO 2244:2000, Packaging -- Complete, filled transport packages and unit loads -- Horizontal impact tests. *Geneve, Switzerland*, (www.iso.org).

International Organization for Standardization. (2000b). ISO 2247:2000, Packaging -- Complete, filled transport packages and unit loads -- Vibration tests at fixed low frequency. *Geneve, Switzerland*, (www.iso.org).

Jain, P., Oswal, R., & Khisty, A. (2018). *Study of Drop Test Parameters Using Design of Experiments*. 1–14.

Johnson, G. R., & Holmquist, T. J. (1994). *An improved computational constitutive model for brittle materials*. *981*, 981–984. https://doi.org/10.1063/1.46199

JPD. (2003). Negative volume in soft materials. Retrieved from https://www.dynasupport.com/howtos/material/negative-volume-in-soft-materials

Lim, C.-T., Teo, Y. M., & Shim, V. P. W. (2002). *Modal and impact analysis of modern* *portable electronic products* (pp. 478–485). pp. 478–485. IEEE Transactions on components and packaging technologies 25.3.

Livermore Software Technology Corporation (LSTC). (2018a). Contact in LS-DYNA. Retrieved from http://ftp.lstc.com/anonymous/outgoing/support/FAQ_docs/contact.pdf

Livermore Software Technology Corporation (LSTC). (2018b). *LS-DYNA® Keyword User's Manual R11 Volume I*. Retrieved from www.lstc.com

Livermore Software Technology Corporation (LSTC). (2018c). *LS-DYNA® Keyword User's Manual R11 Volume II*. Retrieved from www.lstc.com

Livermore Software Technology Corporation (LSTC). (2019a). Hourglass (HG) Modes. Retrieved from http://ftp.lstc.com/anonymous/outgoing/jday/hourglass.pdf

Livermore Software Technology Corporation (LSTC). (2019b). *LS-PrePost*. Retrieved from ftp://ftp.lstc.com/outgoing/lsprepost/

LS-DYNA Support. (2001a). Contact stiffness calculation. Retrieved from https://www.dynasupport.com/tutorial/contact-modeling-in-ls-dyna/contact-stiffness-calculation

LS-DYNA Support. (2001b). Contact types. Retrieved from https://www.dynasupport.com/tutorial/contact-modeling-in-ls-dyna/contact-types

LS-DYNA Support. (2001c). How contact works. Retrieved from https://www.dynasupport.com/tutorial/contact-modeling-in-ls-dyna/how-contact-works

LS-DYNA Support. (2002a). Energy data. Retrieved from https://www.dynasupport.com/tutorial/ls-dyna-users-guide/energy-data

LS-DYNA Support. (2002b). Hourglass. Retrieved from https://www.dynasupport.com/howtos/element/hourglass

LS-DYNA Support. (2002c). Total Energy. Retrieved from https://www.dynasupport.com/howtos/general/total-energy

Military standard. (2000). MIL-STD-810F. Military standard: test method standard for environmental engineering consideration and laboratory tests. *US Department of Defense*.

Military standard. (2004). MIL-STD-883F. Military standard: test methods and procedures for microelectronics. *Washington, DC: US Office of Naval Publications*.

Mills, N. J., & Masso-Moreu, Y. (2005). Finite Element Analysis (FEA) applied to polyethylene foam cushions in package drop tests. *Packaging Technology and Science*, *18*(1), 29–38. https://doi.org/10.1002/pts.676

Mulkoglu, O., Guler, M. A., & Demirbag, H. (2015). Drop Test Simulation and Verification of a Dishwasher Mechanical Structure. *10th European LS-DYNA Conference 2015*.

Neumayer, D., Chatiri, M., & Höermann, M. (2006). Drop Test Simulation of a Cooker

Including Foam Packaging and Pre-stressed Plastic Foil Wrapping. *9th International LS-DYNA Users Conference*, (4), 33–40.

Nitta, K., & Yamana, M. (2012). Poisson’s Ratio and Mechanical Nonlinearity Under Tensile Deformation in Crystalline Polymers. *Rheology*. https://doi.org/10.5772/34881

Ozturk, U. E., & Anlas, G. (2011). Finite element analysis of expanded polystyrene foam under multiple compressive loading and unloading. *Materials and Design*, *32*(2), 773–780. https://doi.org/10.1016/j.matdes.2010.07.025

Park, Y. K., & Kim, J. G. (2004). *Experimental Verification of Drop/Impact Simulation for a Cellular Phone*. https://doi.org/10.1177/0014485104046086

Rao, S. S. (2011). Mechanical Vibrations. In *Recherche* (Vol. 67).

Reithofer, P., Fertschej, A., Hirschmann, B., Jilka, B., & Rollant, M. (2018). *Material Models for Thermoplastics in LS-DYNA ® from Deformation to Failure*. 1–19.

Schueneman, H. H. (1986). A Comparison of Three Different Cushion Test Methods. *SPHE Symposium on Current Trends in Protective Packaging of Computers and Electronic Components, West Consh*(PA: ASTM International), 58–64.

Schueneman, H. H. (1993). *CUSHION MATERIAL EVALUATION*. 24.

Schueneman, H. H. (2017). *Cushion Engineering, Design and Testing*. 44.

Shah, Q. H., & Abid, H. (2012). "LS-PrePost & LS-DYNAtips,” in LS DYNA for Beginners: an Insight Into Ls-Prepost and Ls-Dyna. *Lambert, Saarbrücken, Germany*, p.116.

Shah, Q. H., & Topa, A. (2014). Modeling large deformation and failure of expanded polystyrene crushable foam using LS-DYNA. *Modeling and Simulation in Engineering*, *2014*. https://doi.org/10.1155/2014/292647

Sonnenschein, U. (2008). Modelling of bolts under dynamic loads. *LS-DYNA Anwenderforum*, 12.

# Annexes

This drawing contains confidential information and is the property of Electrolux, without whose permission it may not be copied, shown or handed to a third party or otherwise used and it is to be returned promptly upon request to the design owner, who is responsible for the drawing.

Components reflected by this drawing must not contain substances or coatings of any of the substances banned according to Dir.2002/95/EC,RoHS, or substances on the REACH candidate list published on http://echa.europa.eu/. They have to conform in all respects with Electrolux 'Restricted Materials List' as published on www.electrolux.com. Upon request documentation demonstrating compliance with these requirements shall be immediately provided by the supplier to Electrolux

Dimensions, data and characteristics, which are subjected to Statistic Process Control (SPC) are marked with ⬭

## 356310810 -11 -12

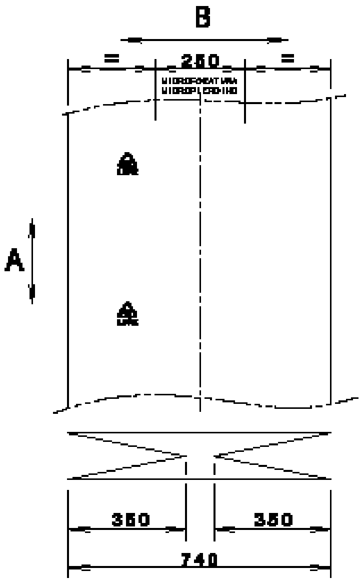

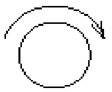

## 356310810

| Physical / Mechanical Features | | Value | Measurement Units | Toll. | Norm |
|---|---|---|---|---|---|
| Polymer | | LDPE | | | |
| Density | | 0.9[illegible] | g/cm3 | +-0.002 | ASTM D 1505 |
| Bandwidth | | 740 | mm | +- 5mm | |
| Folds | | 350 | mm | +- 5mm | |
| Thickness | | 80 | micron | +-8% | |
| Central MICROPIERCING | | 250 | mm | | |
| Tensile Strength | MD*<br>TD* | 25<br>21 | N/mm2<br>N/mm2 | +- 10% | ASTM D 882 |
| Breaking elongation | MD*<br>TD* | 400<br>600 | %<br>% | +- 10% | ASTM D 882 |
| Thermoshrinking at 120°C x 10'' | MD*<br>TD* | 60<br>42 | %<br>% | +- 10% | UNI 8513-2 |

## 356310811 -12

| Physical / Mechanical Features | | Value | Measurement Units | Toll. | Norm |
|---|---|---|---|---|---|
| Polymer | | LDPE | | | |
| Density | | 0.924 | g/cm3 | +-0.002 | ASTM D 1505 |
| Bandwidth | | 740 | mm | +- 5mm | |
| Folds | | 350 | mm | +- 5mm | |
| Thickness | | 70 (for ex.11)<br>80 (for ex.12) | micron | +-8% | |
| Central MICROPIERCING | | 250 | mm | | |
| Tensile Strength | MD*<br>TD* | 24<br>26 | N/mm2<br>N/mm2 | +- 10% | ASTM D 882 |
| Breaking elongation | MD*<br>TD* | 500<br>550 | %<br>% | +- 10% | ASTM D 882 |
| Thermoshrinking at 160°C x 10'' | MD*<br>TD* | 54<br>45 | %<br>% | +- 10% | UNI 8513-2 |

*MD - direction longitudinal

*TD - direction transverse

### CARATTERISTICHE TECNICHE

COEFFICIENTE DI RITRAZIONE

A = 55% (TRASVERSALE)
B = 45% (LONGITUDINALE)

LA BOBINA DEVE ESSERE PRIVA DI SCIVOLANTE

### TECHNICAL FEATURES

MOULD SHRINKAGE COEFFICIENT

A = 55% (TRANSVERSAL)
B = 45% (LONGITUDINAL)

WITHOUT ANTI-SKIDDING

LA BOBINA DEVE ESSERE MICROFORATA PASSANTE NELLA ZONA CENTRALE INDICATA A DISEGNO CON LA QUOTA 250mm, IN MODO TALE CHE RISULTINO ESSERE FORATI ANCHE I LATI RIPIEGATI UNA VOLTA APERTO IL SACCO. LA DISTANZA DEI FORI NON DEVE ESSERE SUPERIORE A 15mm.
LA SUPERFICIE DELLE BOBINE NON ANCORA CARICATE SUGLI INCAPPUCCIATORI DEVE PRESENTARSI LISCIA ED UNIFORME CON EVENTUALI ONDULATURE O SCHIACCIAMENTI AI LATI DELLA ZONA CENTRALE PREFORATA NON SUPERIORI A ±0.5mm.

THE COIL TO BE MICROPIERCED THROUGTH IN THE CENTRAL AND THE SIDE AREA. THE HOLES DISTANCE MUST NOT TO EXCEED 15 mm "STANDARD" HOLES. THE WIDTH OF THE PIERCING MUST BE AS PER ABOVE PICTURE INDICATED BY CENTRAL DIMENSION 250mm.
THE COILS, NOT JET LOADED, MUST BE SMOOTH AND UNIFORM. EVENTUALLY WAVES OR FLATTENING ON THE SIDE OF CENTRAL AREA MUST NOT BE MORE THAN ±0.5mm.

| POS. | MODIFICATIONS | SIGNATURE | REQUEST | DATE |
|---|---|---|---|---|
| 013 | Add variant -12 with thickness of 80µm remove printed symbols (ECN PLS_6606) | PodemN | ECN-022286 | 2014-02-12 |
| L | RESTORE NC.10 | MARUDA | PL88139 | 2012-06-06 |
| K | ADD NC.11 THICKNESS 70 MY, DELETE NC.08-10 (PLS_2437) | MARUDA | PL86007 | 2012-04-04 |
| J | ADD NO.10 SUBST/DEL NO.09 FOR (PLS_868) | MARUDA | PL82271 | 2009-10-09 |
| I | ADD NO.09 FOR PLS QUBE PROJECT (PLS_828) | MARUDA | PL82168 | 2009-09-11 |
| H | PRINT TO PART UPDATE (ECN ZO_ED[illegible])<br>AGG.DISEGNO AL PEZZO PER DIMENSIONE QUOTE SIMBOLI (ECN ZO_ED[illegible]) | CHIAPPARINI | ZO_16436 | 2008-12-03 |
| G | [illegible] | UTILI | ZO_10567 | 2007-12-03 |
| F | Agg. cod.3563108.07 che sost/ann cod.06 | Cortesi B. | ECN_308 | 2006-05-25 |
| E | Aggiornato disegno | Cortesi B. | Supply | 2006-04-12 |
| D | Modificato simb. [illegible] da barrato a MAX 350 Kg (cod.06 R/A 05) | Cortesi B. | Rhino | 2006-01-12 |
| C | Modificata dimensione posiz. simboli da 200 a 250 mm | Cortesi B. | - | 2005-06-16 |
| B | Modificato orientamento simboli imballo | Cortesi B. | - | 2005-05-23 |

| VARIANT NUMBER | REVISION | REPLACED NUMBER | POS. | MODEL | DESIGN USERS | CHANGES FROM THE BASE NUMBER |
|---|---|---|---|---|---|---|
| 356310812 | A | - | 013 | - | PLS | Micropierced polyethylene thickness 80 micron |
| 356310811 | L | - | K | - | PLS | Micropierced polyethylene thickness 70 micron |
| 356310810 | L | 356310809 | L | - | PLS | Micropierced polyethylene thickness 80 micron |

GENERAL TOLERANCES
ISO 2768-mK

A3 [DF07]

MATERIAL
see on variant table

MODEL -

DESIGN USERS -

SCALE -

REPLACES -

EUROPEAN METHOD

TREATMENT -

WEIGHT - Kg.

DERIVED FROM -

SUPPLY SPECIFICATIONS
TS5000 e QS5005

DESIGN OWNER ZO

DRW Cortesi B.

DATE 2005-03-21

CHK -

APPR -

2D ONLY X

CONCEPT 3D -

EXACT 3D -

TITLE Thermoshrinking spool
Sacco per forno

Electrolux

NUMBER 3563108

REV 013

SHEET 1/1